Understanding Himalayan Denudation at the Catchment and Orogen Scale

Dissertation von

Stephanie M. Olen

Kumulative Dissertation zur Erlangung der Würde des akademischen Grades
Doktor Rerum Naturalium (Dr. rer. Nat)

in der Wissenschaftdisziplin

Geologie

Eingereicht an der Mathematisch-Naturwissenschaftichen Fakultät der
Universität Potsdam

Potsdam, Oktober 2015

Published online at the
Institutional Repository of the University of Potsdam:
URN urn:nbn:de:kobv:517-opus4-91423
http://nbn-resolving.de/urn:nbn:de:kobv:517-opus4-91423

This work has not been submitted to any other institution of higher education, and that it was prepared independently and exclusively with the specified funds, the graduate school GRK1364 “Shaping Earth's Surface in a Variable Environment**:** Interactions between tectonics, climate and biosphere in the African-Asian monsoonal region” of the German Science Foundation (DFG, Deutsche Forschungsgemeinschaft; Project GRK 1364/2) and by the HIMPAC research project (Himalayas: Modern and Past Climates), funded by DFG (STR 373/27-1 and 28-1).

Abstract

Understanding the rates and processes of denudation is key to unraveling the dynamic processes that shape active orogens. This includes decoding the roles of tectonic and climate-driven processes in the long-term evolution of high-mountain landscapes in regions with pronounced tectonic activity and steep climatic and surface-process gradients. Well-constrained denudation rates can be used to address a wide range of geologic problems. In steady-state landscapes, denudation rates are argued to be proportional to tectonic or isostatic uplift rates and provide valuable insight into the tectonic regimes underlying surface denudation. The use of denudation rates based on terrestrial cosmogenic nuclide (TCN) such as ^{10}Beryllium has become a widely-used method to quantify catchment-mean denudation rates. Because such measurements are averaged over timescales of 10^2 to 10^5 years, they are not as susceptible to stochastic changes as shorter-term denudation rate estimates (e.g., from suspended sediment measurements) and are therefore considered more reliable for a comparison to long-term processes that operate on geologic timescales. However, the impact of various climatic, biotic, and surface processes on ^{10}Be concentrations and the resultant denudation rates remains unclear and is subject to ongoing discussion. In this thesis, I explore the interaction of climate, the biosphere, topography, and geology in forcing and modulating denudation rates on catchment to orogen scales.

There are many processes in highly dynamic active orogens that may effect ^{10}Be concentrations in modern river sands and therefore impact ^{10}Be-derived denudation rates. The calculation of denudation rates from ^{10}Be concentrations, however, requires a suite of simplifying assumptions that may not be valid or applicable in many orogens. I investigate how these processes affect ^{10}Be concentrations in the Arun Valley of Eastern Nepal using 34 new ^{10}Be measurements from the main stem Arun River and its tributaries. The Arun Valley is characterized by steep gradients in climate and topography, with elevations ranging from <100 m asl in the foreland basin to >8,000 asl in the high sectors to the north. This is coupled with a five-fold increase in mean

annual rainfall across strike of the orogen. Denudation rates from tributary samples increase toward the core of the orogen, from <0.2 to >5 mm/yr from the Lesser to Higher Himalaya. Very high denudation rates (>2 mm/yr), however, are likely the result of ^{10}Be TCN dilution by surface and climatic processes, such as large landsliding and glaciation, and thus may not be representative of long-term denudation rates. Mainstem Arun denudation rates increase downstream from ~0.2 mm/yr at the border with Tibet to 0.91 mm/yr at its outlet into the Sapt Kosi. However, the downstream ^{10}Be concentrations may not be representative of the entire upstream catchment. Instead, I document evidence for downstream fining of grains from the Tibetan Plateau, resulting in an order-of-magnitude apparent decrease in the measured ^{10}Be concentration.

In the Arun Valley and across the Himalaya, topography, climate, and vegetation are strongly interrelated. The observed increase in denudation rates at the transition from the Lesser to Higher Himalaya corresponds to abrupt increases in elevation, hillslope gradient, and mean annual rainfall. Thus, across strike (N-S), it is difficult to decipher the potential impacts of climate and vegetation cover on denudation rates. To further evaluate these relationships I instead took advantage of an along-strike west-to-east increase of mean annual rainfall and vegetation density in the Himalaya. An analysis of 136 published ^{10}Be denudation rates from along strike of the revealed that median denudation rates do not vary considerably along strike of the Himalaya, ~1500 km E-W. However, the range of denudation rates generally decreases from west to east, with more variable denudation rates in the northwestern regions of the orogen than in the eastern regions. This denudation rate variability decreases as vegetation density increases (R=-0.90), and increases proportionately to the annual seasonality of vegetation (R=0.99). Moreover, rainfall and vegetation modulate the relationship between topographic steepness and denudation rates such that in the wet, densely vegetated regions of the Himalaya, topography responds more linearly to changes in denudation rates than in dry, sparsely vegetated regions, where the response of topographic steepness to denudation rates is highly nonlinear.

Understanding the relationships between denudation rates, topography, and climate is also critical for interpreting sedimentary archives. However, there is a lack of understanding of how terrestrial organic matter is transported out of orogens and into sedimentary archives. Plant wax lipid biomarkers derived from terrestrial and marine sedimentary records are commonly used as paleo-hydrologic proxy to help elucidate these problems. I address the issue of how to interpret the biomarker record by using the plant wax isotopic composition of modern suspended and riverbank organic matter to identify and quantify organic matter source regions in the Arun Valley. Topographic and geomorphic analysis, provided by the ^{10}Be catchment-mean denudation rates, reveals that a combination of topographic steepness (as a proxy for denudation) and vegetation density is required to capture organic matter sourcing in the Arun River.

My studies highlight the importance of a rigorous and careful interpretation of denudation rates in tectonically active orogens that are furthermore characterized by strong climatic and biotic gradients. Unambiguous information about these issues is critical for correctly decoding and interpreting the possible tectonic and climatic forces that drive erosion and denudation, and the manifestation of the erosion products in sedimentary archives.

Kurzfassung

Der Schlüssel zum Verständnis der Prozessdynamik tektonisch aktiver Orogene mit ausgeprägten Relief- und klimatisch gesteuerten Denudationsprozessen ist eine genaue Kenntnis der Abtragungsraten und –prozesse, denn diese Informationen erlauben es, eventuelle Ungleichgewichte zwischen tektonisch und klimatisch kontrollierten Faktoren bei der Landschaftsgenese zu betrachten. Sind Landschaften im Gleichgewicht, so sind die Denudationsraten proportional zu den tektonischen und isostatischen Hebungsraten und geben somit wichtige Hinweise über die tektonischen Eigenschaften der Region. Eine weit verbreitete und etablierte Methode zur Bestimmung mittlerer Denudationsraten eines bestimmten Einzugsgebietes ist die Anwendung von Expositionsaltern mittels Beryllium-10, ein terrestrisches kosmogenes Nuklid (^{10}Be TCN). ^{10}Be TCN-Messungen an Sedimenten eines Flusseinzugsgebiets stellen durchschnittliche Abtragungsraten über einen Zeitraum von 10^2 – 10^5 Jahren zur Verfügung und sind daher weniger empfindlich gegenüber stochastischen Änderungen wie Erosionsraten, die über einen kurzen Zeitraum ermittelt werden (z.B. Suspensionsfracht). Sie sind daher zuverlässig einsetzbar, um langfristig operierende Prozesse miteinander zu vergleichen. Allerdings ist bei vielen Sudien unklar, welchen Einfluss verschiedene klimatische, biologische oder geomorphologische Prozesse auf die ^{10}Be Konzentration ausüben und somit auch auf die Abtragungsraten und resultierenden Interpreationen. Vor diesem Hintergrund setze ich mich mit dem Zwischenspiel von Klima, Biosphäre, Topographie und Geologie auseinander bei Erosionsprozessen im Hochgebirge und und untersuche den Einfluss, den diese Faktoren auf Abtragungsraten ausüben, sowohl auf regionalem wie auch auf orogenem Maßstab.

Um Erosionsraten in Hochgebirgsregionen mittels ^{10}Be-Konzentrationen zu berechnen, benötigen wir einige vereinfachende Annahmen, die möglicherweise in anderen Regionen keine allgemeine Gültigkeit haben. Ich untersuche daher den Einfluss verschiedener Prozesse auf die ^{10}Be-Konzentration mit Hilfe 34 neuer ^{10}Be-Konzentrationen des Arun Flusses und

seinen Zuflüssen im Osten von Nepal. Charakteristisch für das Arun Tal sind die steilen Gradienten im Klima mit einem fünffachen Anstieg des mittleren jährlichen Regenfalls über das Orogen sowie in der Topographie, mit Höhen von weniger als 100 m NN im Vorlandbecken bis über 8000 m NN im Gebirge. Die ermittelten Abtragungsraten der Proben der Zuflüsse nehmen gegen das Zentrum des Gebirges von weniger <0.2mm/a auf >5 mm/a zu. Sehr hohe Denudationsraten (> 2mm/yr) können durch grosse Massenbewegungen und Vergletscherungen zu höheren Werten hin verfälscht werden. Sie sind daher nicht repräsentativ für Abtragungsraten auf langen Zeitskalen. Im Arun nehmen die Erosionsraten des Hauptflusses flussabwärts von 0.2 mm/yr im Bereich der Grenze zu Tibet auf 0.91 mm/a am Ausfluss in Sapt Kosi zu. Es ist möglich, dass diese ^{10}Be-Konzentrationen nicht das vollständige Einzugsgebiet der höheren Regionen repräsentieren. Dies wird durch die Betrachtung unterschiedlicher Korngrößenfraktionen verdeutlicht. Ich lege in diesem Zusammenhang dar, wie sich die Korngrösse vom tibetischen Plateau flussabwärts verfeinert und dazu führt, dass die ^{10}BeKonzentrationen im Bereich einer Grössenordnung abnehmen und somit bei synopttischen Betrachtungen mit Vorsicht zu interpretieren sind.

Im Arun Tal und sowie über den ganzen Himalaja hinweg sind Topographie, Klima und Vegetation aufgrund orografischer Effekte sehr stark miteinander gekoppelt. Das Ansteigen der Denudationsraten im Übergang vom Lesser zum Higher Himalaya stimmt mit der abrupten Höhenänderung, der Hangneigung und der Menge der mittleren jährlichen Regenfallmenge überein. Es ist generell schwierig, die möglichen Einflüsse von Klima und der Vegetationsdichte auf die Abtragungsraten über das Orogen hinweg (N-S) zu entziffern. Stattdessen, nutze ich die parallel zum Himalaja verlaufende unahme des mittleren jährlichen Regenfalles und der Vegetationsdichte in einem W-O-gerichteten orogenparallelen Streifen.

Eine Analyse 136 publizierter ^{10}Be TCN Abtragungsraten entlang des Gebirges zeigt dass die im Streichen liegenden mittleren Denudationsraten (ca. 1500 km Ost-West) nicht signifikant variieren. Generell sinken die Denudationsraten in ostwärtiger Richtung, wobei in den nordwestlichen

Regionen des Himalajas variablere Abtragungsraten vorherrschen als in den östlichen Regionen. Diese Vielfalt in den Denudationsraten sinkt allerdings mit steigender Vegetationsdichte (R=-0.90) und steigt proportional zur (jährlichen) Saisonalität der Vegetation (R=0.99). Vielmehr noch wird das Verhältnis zwischen der Steilheit des Terrains und den Abtragungsraten durch Niederschlagsmenge und -verteilung sowie Vegetation beeinflusst - z. B. in feuchten Gebieten mit starker Vegetation reagiert die Topographie eher linear auf Wechsel in den Abtragungsraten, verglichen mit trockenen, kaum bewachsenen Regionen, wo die Reaktion der topographischen Steilheit auf die Denudationsraten nicht-linear ist.

Das Verständnis der Beziehungen zwischen Erosion, Topographie und Klima ist auch entscheidend für die korrekte Interpretation von Sedimentarchiven. Unser Wissen über die Repräsentativität organischen Materials in Ablagerungsräumen.(z.B. Flussdeltas) ist nach wie vor sehr limitiert. Blattwachse höherer Landpflanzen, extrahiert aus terrestrischen und marinen Sedimenten, sind ein häufig verwendeter paläohydrologischer Proxy, der die hydrologischen Bedingungen in den ehemaligen Einzugsgebieten definieren kann. Im Rahmen dieser Arbeit nutzen meine Ko-Autoren und ich die Isotopenzusammensetzung von Pflanzenwachsen aus Suspensionsmaterial als Indikatoren der Provenienz und zur Quantifizierung des organischen Materials. Die Analyse von Vegetationsdichte und Regenverteilung in Kombination mit Abtragungsraten des Einzugsgebietes, welche durch die mittleren 10Be-Erosionsraten im Arun-Tal gestützt werden, zeigen, dass das Vorhandensein dichter Vegetation ein zwar notwendiges, aber nicht hinreichendes Kriterium für hohen Austrag organischer Materie ist. Vielmehr kann gezeigt werden, dass nur eine Kombination aus dichter Vegetationsdecke und Erosion zu hohem Austrag organischer Materie führt. Für die Interpretation entspechender Sedimentbecken-Archive bedeutet das, dass entsprechende Ablagerungen im Wesentlichen jene Bereiche des Einzugsgebietes repräsentieren, welche durch die Kombination von hoher Pflanzendichte und starker Erosion charakterisiert sind.

Meine Studien belegen, wie wichtig es ist, die verschiedenen Erosionsparameter und Ratenänderungen zu erkennen und in ihren Auswirkungen auf die Umwelt zu verstehen, wenn Abtragungsraten unter heutigen und vergangenen Klimabedingungen sowie unter tektonisch getriebenen Voraussetzungen korrekt bewertet werden sollen. Dies trifft vor allem dann zu, wenn. im Kontext des globalen Wandels Sedimentarchive Auskunft über unterschiedliche Einflussfaktoren auf Erosion und Sedimentation geben sollen.

Publications and author contributions

This thesis is comprised of three independent studies published or in review in high impact peer review journals. Chapters 3 through 5 correspond to the individual studies.

Chapter 3

Understanding erosion rates in the Himalayan orogen: A case study from the Arun Valley

Stephanie M. Olen, Bodo Bookhagen, Bernd Hoffmann, Dirk Sachse, D.P. Adhikari, Manfred R. Strecker

Stephanie M. Olen, Bodo Bookhagen, and Manfred R. Strecker contributed to the design of the study. Stephanie M. Olen, Bodo Bookhagen, Bernd Hoffmann, Dirk Sachse, and D.P. Adhikari contributed to organizing and conducting field work, strategy and sample collection. Stephanie M. Olen and Bodo Bookhagen contributed to the analysis of ^{10}Be TCN samples in the laboratory and calculation of denudation rates. Stephanie M. Olen wrote the manuscript, with contributions from all co-authors.

Chapter 4

Role of climate and vegetation in modulating denudation rates in the Himalaya

Stephanie M. Olen, Bodo Bookhagen, Manfred Strecker

Stephanie M. Olen and Bodo Bookhagen contributed to the design of the study. Stephanie M. Olen compiled the ^{10}Be TCN dataset, recalculated denudation rates using standardized methods, and ran all correlation analysis. All co-authors discussed the interpretation of the results. Stephanie M. Olen wrote the manuscript, with contributions from Bodo Bookhagen and Manfred R. Strecker.

Chapter 5

Ecologic, climatic and geomorphic drivers of terrestrial organic matter transport in the trans-Himalayan Arun River catchment, E Nepal

Bernd Hoffmann, Sarah J. Feakins, Bodo Bookhagen, Stephanie M. Olen, Danda P. Adhikari, Janardan Mainali, Dirk Sachse

Stephanie M. Olen, Bernd Hoffmann, Bodo Bookhagen, Danda P. Adhikari, and Dirk Sachse contributed to the design, strategy, and organization of field work. Stephanie M. Olen, Bernd Hoffmann, Bodo Bookhagen, Dirk Sachse, and Janardan Mainali conducted field work and collected samples. Bernd Hoffmann, Sara J. Feakins, and Dirk Sachse contributed to the sample laboratory analysis. Bernd Hoffmann, Stephanie M. Olen, Bodo Bookhagen, and Dirk Sachse contributed to the terrestrial organic matter weighting scheme. Stephanie M. Olen provided the topographic analysis for the erosion weighting model. Bernd Hoffmann wrote the manuscript with contributions from all co-authors.

Table of Contents

List of Figures

List of Tables

Acknowledgements

First and foremost, I would like to express my deep gratitude to Bodo Bookhagen. Thank you for supporting me and my research from start to finish, from Nepal, to Santa Barbara, to Potsdam. For giving me direction, and letting me follow my own. This work would have been much poorer without your insight, guidance, and encouragement.

Thank you to Manfred Strecker for supporting me throughout my time at Potsdam and ensuring that my research was always my only worry. I would like to thank everyone involved in the Graduate School GRK 1364, "Shaping Earth's Surface in a Variable Environment: Interactions between tectonics, climate and biosphere in the African-Asian monsoonal region" and in particular Henry Wichura. My time in Potsdam wouldn't have been the same without everyone involved in the Graduate School, and our time in Kenya and India will be some of my best memories of my PhD. I'd like to particularly thank Rasmus Thiede and Dirk Scherler for giving their time to these expeditions.

I am grateful to everyone who enabled and supported my two field seasons in Nepal. In particular Danda P. Adhikari, for helping us organize in Nepal from Tribhuvan University, and Bhim Chand of Earth's Paradise Trekking, for organizing and supporting our second field season.

I owe a particular debt of gratitude to Bernd Hoffmann, who was the best companion in the field I could have hoped for, and shared in all the adventures and frustrations in the Arun Valley. Thanks, Bernd, for helping me carry kilos of wet sand every day through the mountains, for putting up with me through thick and thin, and for sharing the highs, lows, laughter (happy and helpless), exhaustion, inspiration, Tüborg, and dal bhat of two truly memorable field seasons. To this end I am also grateful to Sophia Wagner, Janardan Mainali, Raphael Scheffler, Manoj, Birendra Bam, and all of our local Nepali support. Special thanks to Bambu Skully.

My time at Potsdam would not have been the same without an amazing set of officemates that provided helpful scientific discussion and invaluable friendship: Patricia Eugster, Veronica Torres Acosta, Fabiana Castino, Fred

Amour, Anke Deekan, and Johannes Kalbe. I owe special thanks to Patricia, who provided the German translation of the abstract for this thesis.

There are many people at Potsdam who contributed to my scientific development. I would like to give particular thanks to Ed Sobel, whose constant presence at seminars and reading groups and general availability for help and questions of all sorts has been, I believe, invaluable to all the Ph.D. students in our group, myself certainly included. There are several post docs and Ph.D. students who were a great presence in the group, providing discussion and insights: Paolo Ballato, Angela Langraf, Sara Savi, Euan Macaulay, Alejandro Bande, Simon Riedl, Görkem Sviri, Steffani Toefelde, Saptarshi Dey, Alexander Rohrmann, and Heiko Pingel to name a few.

I would be remiss not to acknowledge my past advisors and mentors who paved my way to this point. Special thanks to Todd Ehlers and Arlo Weil for first teaching me the rigors of scientific research and writing, and for encouraging me and pushing me forward throughout my scientific development. Thanks also to Donald Barber for giving me my first real experience with field work and all its perks and pitfalls. Without these three and many others at Bryn Mawr College and the University of Michigan, I never would have made it as far as I have.

Last but certainly not least, I'd like to thank my family. Louise, for her constant encouragement, occasional scientific discussions, and constructive criticism of manuscript titles. My parents for supporting my intellectual endeavors from the beginning, even when they took me across the ocean to Germany. Especially my dad, for encouraging a love of learning from a young age. And, of course, I can't wait to explore the great outdoors with Julian and Greer.

Chapter 1: Introduction

1.1 Motivation

The landscapes of mountain belts result from the interplay between tectonic forces that shorten and uplift crustal material, and the denudation processes that remove it. Surface denudation is the combination weathering and erosion of sediment (e.g., *Bissell*, 1921). As such, it is the process responsible for removal of mass from Earth's surface and delivery of sediment into downstream transport systems. Material denuded from the interior of mountain belts is forms fluvial terraces, intermontane basins, and foreland alluvial plains critical for agriculture, and is ultimately delivered to continental shelf regions and submarine fans that provide important geologic archives (e.g., *Brozovic and Burbank*, 2000; *Clift et al.*, 2001).

The Himalaya, the world's largest Cenozoic collisional mountain belt, is associated with one of the largest sediment-flux systems known (*Milliman and Syvitski*, 1992), testified by the scale of the Indus and Ganges-Brahamaputra submarine fans (*Curray and Moore*, 1971; *Milliman et al.*, 1984; *France-Lanord et al.*, 1993; *Einsele et al.*, 1996) with sediment transported as far as the Sumatran subduction zone, where large accretionary wedges are formed (*Moore et al.*, 1982). By removing material from the surface and delivering it to fluvial systems, denudation directly impacts the sediment yield of rivers, which can have a critical impact on hydropower projects (e.g. *Singh et al.*, 2003 *Wulf et al.*, 2012). This is a particular concern in high-mountain settings, such as the planned 900 megawatt Arun III hydroelectric project in eastern Nepal. On a global and geologic scale, aerially extensive chemical denudation associated with Cenozoic uplift the Himalaya has been proposed as a potential link to global cooling trends via carbon-dioxide drawdown during silicate weathering (*Raymo et al.*, 1988; *Molnar and England*, 1990; *Raymo and Ruddiman*, 1992). In active orogens, denudation rates and the different processes responsible for wearing down mountain ranges are impacted directly by the combination of tectonics, regional climate, and the biosphere. Understanding how denudation rates are influenced by these processes and their forcing factors is critical to understanding how processes in mountain

belts may operate, how to correctly interpret sedimentary archives, and how to assess natural hazards.

Earth's tectonic forces generate crustal material to be eroded via rock uplift on long timescales, but are also able to trigger massive erosion events, e.g., through seismically-triggered abrupt uplift, and subsequent landsliding and river incision (e.g., *Yanites et al.*, 2010a; *Parker et al.*, 2011). In steady-state landscapes, denudation rates are believed to be proportionate to tectonic or isostatic uplift rates (e.g., *Lavé and Avouac*, 2001; *Willett and Brandon*, 2002; *Kirby and Whipple*, 2012). Topographic relief is proportionate to denudation rates and can therefore be used to estimate order-of-magnitude uplift rates (*Ahnert*, 1970). Thus, quantifying denudation rates and understanding the relationship between denudation rates and topographic steepness can provide valuable insight into the underlying tectonic regimes of active orogens. This is especially useful when factors such as dense vegetation cover make detailed geologic mapping of tectonic structures difficult, such as along the densely vegetated southern flanks of the Himalaya. Several studies have argued that in tectonically highly active orogens, such as the Himalaya or Andes, high rates of tectonic uplift dominate the denudation rate signal and that climatic factors play only a secondary role in setting denudation rates (e.g., *Riebe et al.*, 2001; *Burbank et al.*, 2003; *Riebe et al.*, 2004; *Safran et al.*, 2005; *Adlakha et al.*, 2013).

However, the rates and patterns of denudation have also been documented to be sensitive to and driven by changes in climate (e.g., *Willett*, 1999; *Reiners et al.*, 2003; *Moon et al.*, 2011; *Ferrier et al.*, 2013a *Ferrier et al.*, 2013b; *McPhillips et al.*, 2013). Processes related to precipitation (e.g., *Morgan*, 1978), glaciation (e.g., *Egholm et al.*, 2009), and periglacial activity (e.g., *Hales and Roering*, 2007) constitute some of the tools of erosion that removes material from orogens. Modeling studies have suggested that regional climatic changes can result in basin aggradation and incision (*Tucker and Slingerland*, 1997). In the NW Himalaya, for example, large-scale aggradation has been linked to intensified monsoon precipitation on millennial timescales, triggering mass-wasting events in high-elevation sectors caused sediment-choked fluvial systems farther downstream (*Bookhagen et al.*, 2005a). A subsequent decrease in precipitation was inferred to result in fluvial incision as rivers transported less sediment and were able to incise into fluvial terraces (*Bookhagen et al.*, 2006). On seasonal timescales, high fluxes

of suspended sediment have been found to correspond to large storm events (e.g., *Wolman and Miller*, 1960; *Coppus and Imeson*, 2002; *Wulf et al.*, 2012). On timescales involving several 10^5 to 10^6 years, increased exhumation rates derived from low-temperature thermochronology have been linked to enhanced denudation during glacial periods (e.g., *Ehlers et al.*, 2006). In this context, erosion and sedimentation rates have thus been used to infer the onset and cessation of climatic change (e.g., *Herman et al.*, 2013).

Through modeling studies, it has been inferred that protracted differences in moisture regimes impacting mountain ranges may ultimately lead to topographic asymmetry (e.g., *Bonnet*, 2009). The effect of localized high precipitation at orographic barriers and the resulting localized high denudation rates has been hypothesized to drive greater exhumation and uplift via isostatic compensation and the mechanics of the orogenic Coulomb wedge (e.g., *Dahlen et al.*, 1984; *Dahlen*, 1990; *Willett*, 1999). Along the southern flanks of the Himalayan orogen, the apparent focus of high precipitation and denudation has long been thought to result from tectonic-climatic coupling (e.g., *Beaumont et al.*, 2001 *Hodges et al.*, 2004 *Thiede et al.*, 2004). On a regional scale, in the Arun Valley of eastern Nepal, focused incision of the Arun River has been suggested to drive the uplift of a large river anticline (*Oberlander*, 1985; *Montgomery and Stolar*, 2006). Similar river anticlines are observed in the adjoining Sun Kosi and Tamor Valleys (*Schelling*, 1992). However, Himalayan studies of denudation rates based on timescales of $>10^5$ years have revealed a decoupling of rainfall and denudation across strike (e.g., *Burbank et al.*, 2003; *Adlakha et al.*, 2013). Fluvial incision rates were first quantified in the Himalaya and linked to tectonic uplift by the seminal study of Lavé and Avouac (*Lavé and Avouac*, 2001), arguing that incision and uplift rates are linked to a flat-ramp-flat geometry of the Main Himalayan Thrust. Denudation rate estimates over centennial to millennial timescales have confirmed this and have been associated with tectonic uplift rates and the underlying structure of the major faults systems (e.g., *Godard et al.*, 2014; *Scherler et al.*, 2014; *Le Roux-Mallouf et al.*, 2015; *Morell et al.*, 2015). However, despite several studies that have argued for a primarily tectonic control on denudation rates, Hirschmiller et al. (2014) documented that the morphology and width of the Himalayan foreland fold-and-thrust belt is controlled primarily by climate-driven erosion along-strike (E-W) of the orogen. Thus a careful quantification and understanding of the relationship

between denudation rates and tectonic and climatic processes across and along strike is critical to understanding the dynamics of the Himalayan orogeny.

1.2 Denudation rates from Berryllium-10 Terrestrial Cosmogenic Nuclides

In recent decades, the quantification of catchment-mean denudation rates through the measurement of *in situ*-produced Berrylium-10 terrestrial cosmogenic nuclides (^{10}Be TCN) has become a standard tool of geomorphologists (*Brown et al.*, 1995; *Bierman and Steig*, 1996; *Granger et al.*, 1996). In the quartz-bearing lithologies, ^{10}Be accumulates in the uppermost layers of Earth's surface via exposure to cosmogenic rays (*Nishiizumi et al.*, 1984; *Lal and Arnold*, 1985). The production rate of ^{10}Be in surface rocks depends primarily on the latitude, altitude, and degree of shielding of a particular location (*Lal*, 1991; *J Dunne et al.*, 1999; *Dunai*, 2000; *Desilets and Zreda*, 2001; *Dunai*, 2001; *Masarik et al.*, 2001). Measurement of ^{10}Be TCNs is a standard method of exposure dating, due to the increase of ^{10}Be within quartz grains of an exposed rock surface through time (*Lal and Arnold*, 1985; *Klein et al.*, 1986). The same principle can be applied to a sample of fluvial sand to calculate catchment-mean denudation rates. Sand grains in a fluvial system must necessarily come from upstream hillslopes and channels. Thus, in slowly denuding landscapes, quartz grains eroded from rocks in the catchment will have a long time to accumulate ^{10}Be before being delivered to the fluvial system. In rapidly denuding landscapes, quartz grains will have little time to accumulate ^{10}Be prior to fluvial transport. Hence there is an inverse relationship between the upstream denudation rate of the catchment and the measured ^{10}Be concentration in fluvial sand (for a review see *von Blanckenburg*, 2005, and references therein). The advantages of the method are that (1) fluvial sand samples theoretically represent the entire catchment, allowing for estimation of catchment-mean denudation rates; and (2) denudation rates derived from the measurement of ^{10}Be TCNs are integrated over 10^2-10^5 years, and thus integrate the stochastic processes that might bias or be missed by short-term estimations of denudation rates, such as suspended sediment-load measurements (*Kirchner et al.*, 2001).

However, surface and climatic processes such as landsliding (*Niemi et al.*, 2005; *Yanites et al.*, 2009) and glacial processes (*Godard et al.*, 2012; *Glotzbach et al.*, 2013) can impact ^{10}Be concentrations by delivering fresh material to the

catchment so that basin-wide denudation rates do not represent accurate temporal averages. A study by Niemi et al. (2005) modeling ^{10}Be TCN concentrations in catchments dominated by shallow landslides concluded that in sufficiently large catchments, fluvial TCN concentrations are an appropriate method to quantify long-term denudation rates and are likely to provide more accurate estimates than from bedrock samples. The authors suggest that to accurately reconstruct denudation rates from ^{10}Be TCN, it is required that the catchment fulfill a minimum area, such that:

$$Area\ (km^2) = \frac{100\ km^3/Myr}{E\ km/Myr}$$

where *Area* is the required minimum catchment area to provide reliable denudation rate estimates, and *E* is the catchment-average denudation rate. In a subsequent study, Yanites et al. (2009) modeled the effect of deep-seated landsliding on TCN concentrations. In catchments that experienced deep-seeded landslides, only catchments greater than ~100 km^2 produced reliable denudation rates from ^{10}Be TCN concentrations. Furthermore, Yanites et al. (2009) highlight the importance that the sediment be well-mixed to "blur" the effect of large or deep landslides. An implicit assumption of the sampling of fluvial sand samples, however, is that the analyzed grain sizes are representative of all denudation processes occurring in the catchment. Recent studies analyzing multiple grain sizes have cast doubt on this assumption (*McPhillips et al.*, 2014; *Puchol et al.*, 2014; *Carretier et al.*, 2015). Analysis of larger grain and cobble sizes from rivers in the Central Andes (*McPhillips et al.*, 2014; *Carretier et al.*, 2015) and Nepalese Himalaya (*Puchol et al.*, 2014) suggest that the grain sizes typically analyzed (generally 250-500 μm) may not capture denudation signals from landsliding. Both studies present evidence that larger grain sizes and individually-measured cobbles, presumed to be derived from mass-wasting, have systematically lower ^{10}Be concentrations. The continuing refinement of the method suggests we may not yet understand all the dynamic processes that impact ^{10}Be TCN concentrations in fluvial sand samples.

1.3 Vegetation as an agent of landscape change and recorder of climate change

Climatic influences on landscape evolution are typically cast in terms of precipitation-related, glacial, or periglacial processes. The impact of vegetation, directly controlled by climate, on denudation processes, however, has long been recognized (e.g., *Wilson*, 1973; *Wolman and Gerson*, 1978; *Bull*, 1991). The role of vegetation in creating steep soil-mantled landscapes in humid tropical regions was observed by Krynine (1936). Büdel (1982) suggested that regional climatic conditions, including vegetation and soil cover, result in morphogenetic zones corresponding to latitudinal climate transitions. In their classic study, Langbein and Schumm (1958) attribute the relationship between precipitation and sediment yield to changes in vegetation cover. They present a model wherein sediment yield is low in arid environments, where not enough precipitation occurs to affect sediment transport, then rapidly rises as a function of precipitation until there is enough precipitation to support a stable vegetation cover. Following this point, sediment yield rapidly decreases again. This observed stabilizing effect of vegetation can be attributed to several factors, including: the interception of raindrops before they strike the surface (e.g., *Noble and Morgan*, 1983); root cohesion, which creates a mechanical resistance to sliding (e.g., *Waldron*, 1977); and greater infiltration rates, which decreases erosion by overland flow (e.g., *Horton*, 1945; *Wainwright et al.*, 2000). Modeling studies simulating the effect of vegetation on landscapes have found that vegetation inhibits erosion on hillslopes, leading to oversteepened topography. The general inhibition of erosion in vegetated regions leads to a transition from run-off dominated erosion in sparsely or non-vegetated landscapes to landslide-dominated erosion in densely vegetated landscapes (*Collins et al.*, 2004; *Istanbulluoglu et al.*, 2004; *Istanbulluoglu and Bras*, 2005). Despite this, to date there have been few large-scale studies of the interactions between vegetation, topography, and erosion (exceptions include *Carretier et al.*, 2013; *Jeffery et al.*, 2014; *Torres Acosta et al.*, 2015).

Vegetation does not only play an important role as an agent of landscape change, but the remnants of vegetation or pollen may be useful recorders of climate change. The preservation of plant lipid biomarkers and their stable isotope compositions have become an increasingly important tool for understanding past changes in climate and the hydrologic cycle (e.g., *Freeman and Colarusso*, 2001).

Stable hydrogen and oxygen isotopes are preserved in organic compounds, particularly leaf waxes, and transported through fluvial systems before they are deposited and preserved in sedimentary archives. Changes in hydrogen, deuterium, and oxygen-18 (∂D an ∂^{18}O) from such archives can be employed to interpret paleoclimate and paleohydrology histories (e.g., *Sachse et al.*, 2012 and references therein). However, to properly interpret these records, it is necessary to have an accurate understanding of how stable isotopes from precipitation are recorded in leaf wax of present-day plants, and the source area of terrestrial organic matter found in sedimentary archives.

1.4 Objectives

The objective of this dissertation is to build upon our understanding of how climate, surface processes, and denudation relate in an active, highly dynamic orogen such as the Himalaya. To this end, the dissertation addresses three primary research questions:

1. How do dynamic tectonic, climatic, and surface processes impact ^{10}Be concentrations and denudation rates at the regional scale in the Arun Valley?
2. What processes modulate denudation rates along strike of the Himalaya at the orogen scale?
3. How can a clear understanding of the spatial patterns of denudation rates aid the interpretation of sedimentary and biomarker archives?

Chapter 2 provides a tectonic and climatic overview of the Himalaya. Chapters 3 through 5 address these questions as independent studies published in or submitted to peer-reviewed journals. Chapter 3,"Understanding erosion rates in the Himalaya: A case study from the Arun Valley" by Stephanie Olen, Bodo Bookhagen, Bernd Hoffmann, Dirk Sachse, Danda P. Adhikari, and Manfred R. Strecker, addresses Research Objective 1 and has been published in *The Journal of Geophysical Research: Earth Surface*, 120, doi:10.1002/2014JF003410. Research Objective 2 is addressed in Chapter 4, "Role of climate and vegetation in modulating denudation rates in the Himalaya" by Stephanie Olen, Bodo

Bookhagen, and Manfred R. Strecker, which is currently in review in the journal *Earth and Planetary Science Letters*. Chapter 5 addresses Research Objective 3 and is titled "Ecologic, climatic and geomorphic drivers of terrestrial organic matter transport in the trans-Himalayan Arun River catchment, E Nepal" by Bernd Hoffmann, Sarah J. Feakins, Bodo Bookhagen, Stephanie Olen, Danda P. Adhikari, Janardan Mainali, Dirk Sachse, and is in review in the journal *Earth and Planetary Science Letters*.

Chapter 2: The Himalaya

2.1 Tectonic and geologic overview

The Himalaya and the adjacent Tibetan Plateau have formed for the last ~50 Ma as the result of the ongoing collision between India and Eurasia (*Dewey and Bird*, 1970). The Himalayan mountains represent the orogenic wedge between the Tibetan Plateau and the Indian subcontinent, underlain by a basal décollement known as the Main Himalayan Thrust, MHT (*Schelling and Arita*, 1991). The major thrust systems of the orogen are generally thought to root in the Main Himalayan Thrust (*Zhao et al.*, 1993). From the foreland to the hinterland (youngest to oldest), the major fault systems at the surface are: the Main Frontal Thrust, MFT (*Gansser*, 1964; 1983 *Fuchs and Linner*, 1995; *Lavé and Avouac*, 2001), the current surficial expression of the Main Himalayan Thrust; the Main Boundary Thrust, MBT (e.g., *DiPietro and Pogue*, 2004); and the Main Central Thrust, MCT (*Heim and Gansser*; *Le Fort*, 1975 *Searle et al.*, 2003). North of the Main Central Thrust, the Himalaya is separated from the Tethyan Sediments by a normal fault system, the Southern Tibetan Detachment, STD (sometimes referred to as the Southern Tibetan faults or STF) (*Burchfiel et al.*, 1992).

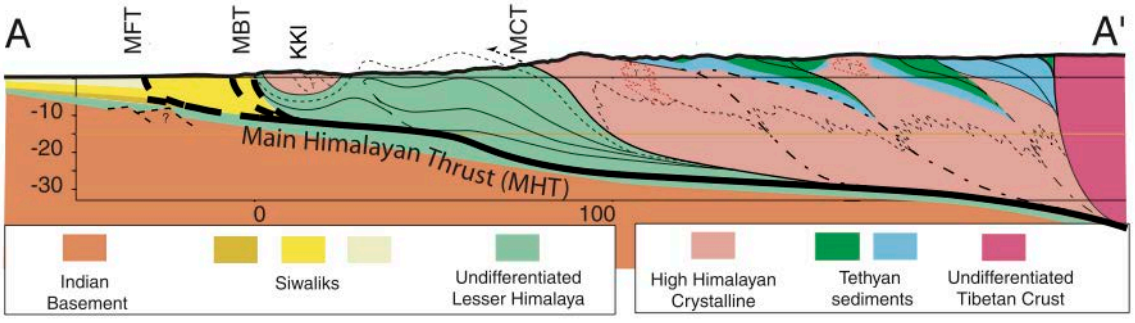

Figure 2.1 Major faults and geology of the Himalaya

Simplified cross-section across Central Nepal from Gangetic Plain (A) to Tibet (A') showing major thrust fault systems: Main Frontal Thrust (MFT), Main Boundary Thrust (MBT), Main Central Thrust (MCT), all soling at depth to the Main Himalayan Thrust (MHT). Major fault systems separate principal geologic units, from foreland to hinterland, the sediments and sedimentary rocks of the Siwaliks (yellow); the Lesser Himalaya Series (light green); the Higher Himalaya (light orange); and the Tethyan Sediments (green, blue). From *Bollinger et al.*, 2004.

The principal structures of the Himalaya described above separate the major geologic units of the orogen. From the undeformed foreland sedimentary basins on the Indian plate, north of the MFT are the Siwaliks, a foreland fold-and-

thrust belt comprised primarily of Miocene to Pleistocene sedimentary rocks (*Burbank et al.*, 1996a; *DeCelles et al.*, 1998). The MBT separates the Siwaliks from the Lesser Himalayan Zone, a region of low- to high-grade metasedimentary rocks (*Gansser*, 1964; *Stöcklin*, 1980; *Valdiya*, 1980; *Schelling*, 1992). High-grade crystalline units are also referred to as the Lesser Himalayan Crystalline Series (e.g., *Schelling*, 1992). Farther into the hinterland, the MCT separates the Lesser Himalayan Zone from the Greater or Higher Himalayan Crystalline units, high-grade metasedimentary, meta-igneous, and igneous rocks (*Le Fort*, 1975; *Yin*, 2006). North of the STD is the Tethyan Himalaya Sequence, comprised primarily of Proterozoic to Eocene sedimentary rocks (*Garzanti*, 1993; 1999).

2.2 Topography of the Himalaya along strike

Across much of the Himalaya, topography is generally divided by three physiographic transitions corresponding to regions of differing uplift, erosion, relief, and elevation. Hodges et al. (2001) describe these transitions as follows: The "physiographic transition 1" (PT_1) marks the transition from little uplift and erosion on the high-elevation, low-relief Tibetan Plateau from high uplift and erosion in the high-relief Higher Himalaya; the "physiographic transition 2" (PT_2) marks the transition into areas characterized by moderate uplift and erosion and moderate relief and elevation in the Lesser Himalaya; "physiographic transition 3" (PT_3) marks the transition into low uplift and erosion and minimal elevation in the foreland. In this manuscript, I refer to the Siwaliks as the region between the PT_3 and MBT; the Lesser Himalaya from the MBT to PT_2; and the Higher Himalaya from the PT_2 to the STD/PT_1.

The PT_2 has been of particular interest to researchers due to the fact that it does not correspond to the location of the MCT or another known structure along strike (e.g., *Hodges et al.*, 2001; *Wobus et al.*, 2005; *Harvey et al.*, 2015). The transition between the Lesser and Higher Himalaya is most prominent from the Garhwal Himalaya through Nepal and Sikkim and creates a "two-step" topography throughout these regions. It is notably absent in regions father west in the Himalaya and from Bhutan and regions in the east. The varying topographic expressions along strike are generally believed to be the result of recent to modern tectonic activity across the orogen, with the high elevation and relief of the Higher

Himalaya linked to relatively higher uplift rates than in the Lesser Himalaya (e.g., *Hodges et al.*, 2001). This differential uplift has been linked to the southward extrusion of the Tibetan

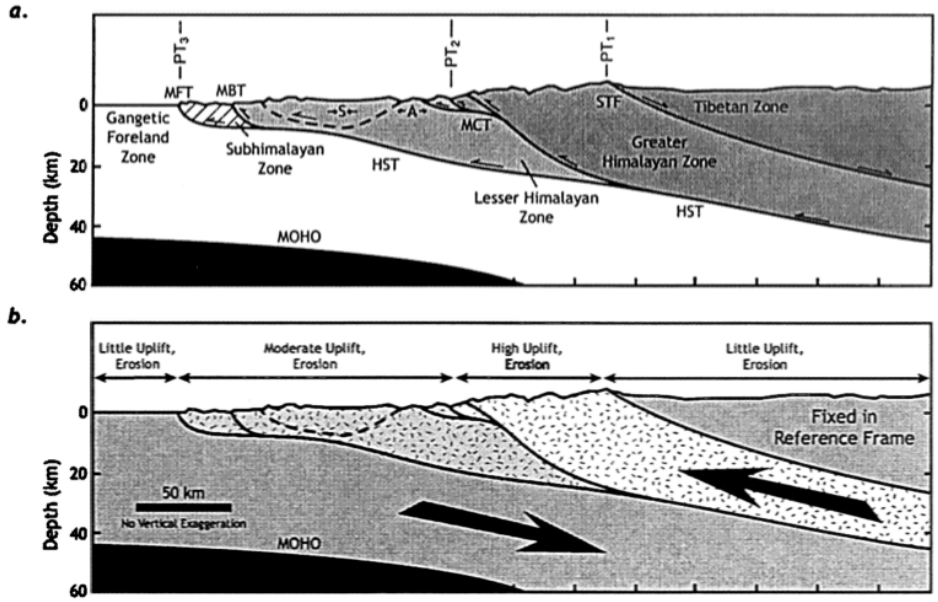

Figure 2.2 Topographic divisions of the Himalaya.

Major Himalayan physiographic regions of Central Nepal. From *Hodges et al., 2001*.

crust through a low viscosity channel (e.g., *Beaumont et al.*, 2001; *Hodges et al.*, 2001), out-of-sequence thrusting or reactivation of the MCT (e.g., *Hodges et al.*, 2004; *Wobus et al.*, 2005), and exhumation over a mid-crustal ramp (*Cattin and Avouac*, 2000; *Avouac*, 2003; *Bollinger et al.*, 2004; *Schulte-Pelkum et al.*, 2005; *Robert et al.*, 2009; *Harvey et al.*, 2015; *Morell et al.*, 2015).

The densely vegetated slopes of the southern flanks of the Higher and Lesser Himalaya make detailed geologic mapping across this important topographic feature difficult. Studies of low-temperature thermochronology (*Robert et al.*, 2009) and ^{10}Be TCN (*Wobus et al.*, 2005; *Godard et al.*, 2014; *Scherler et al.*, 2014; *Morell et al.*, 2015) have confirmed that exhumation and denudation rates, respectively, are greater in the Higher Himalaya compared to the Lesser Himalaya.

2.3 Climate of the Himalaya

The climate of much of the Himalaya is dominated by the Indian Summer Monsoon (ISM). Every summer, the ISM delivers large amounts of highly

seasonal rainfall, with much of the Himalaya receiving over 80% of annual rainfall during the summer months from May through October and local rainfall rates in excess of 5 m/yr (*Bookhagen and Burbank*, 2006; 2010) The ISM was originally proposed to be the result of differential heating between the Tibetan Plateau and the Indian Ocean (e.g., *Flohn et al.*, 1968 *Webster*, 1987). The current widely accepted hypothesis is that the ISM is a result of the northward migration of the Intertropical Convergence Zone (ITCZ) (e.g., *Charney*, 1969; *Gadgil*, 1988), which separates the wind circulation of the northern and southern hemispheres (*Charney*, 1969). A low-pressure cell caused by the heating of Central Asia causes the ITCZ to be deflected northward, while a high-pressure cell over the Indian and Pacific Oceans forces the transport of moisture

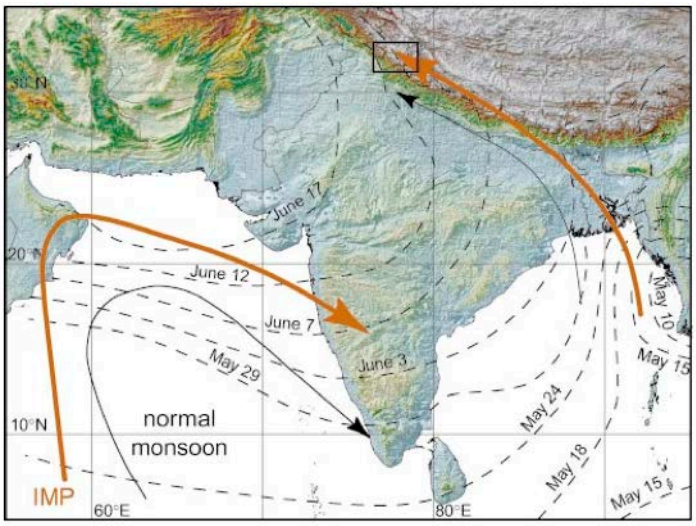

Figure 2.3 Indian Summer Monsoon wind circulation trajectories.

Black arrows represent moisture transport routes during normal monsoon years; orange arrows represent intensified monsoon phases. Dashed lines signify the dates of rainfall onset across the region. From *Bookhagen et al., 2005a* and references therein.

northwestward into the Himalaya. An alternative theory suggests that the Himalaya act as a barrier from Arctic cold air systems, insulating warm, moist air masses over the Indian subcontinent, allowing the ITCZ to migrate northward over the Himalaya (*Boos and Kuang*, 2010; *Molnar et al.*, 2010). During abnormally strong monsoon years, the ITCZ is deflected farther north, resulting in moisture penetrating deeper into the orogen (e.g., *Bookhagen et al.*, 2005a). The primary moisture source for the ISM, therefore, is the Bay of Bengal. ISM moisture then travels westward along the orographic barrier of the southern flanks of the Himalaya. This results in both an along-strike east-to-west and across-strike south-to-north decreasing rainfall gradient (*Bookhagen and Burbank*, 2006; 2010).

Differing topography along strike results in either a single or double peak in rainfall across strike of the orogen. Bookhagen and Burbank (2010) identify a single, strong rainfall peak in regions with "one-step" topography such as NW India and Bhutan, and two, lower rainfall peaks in "two-step" topography across Nepal and much of Sikkim.

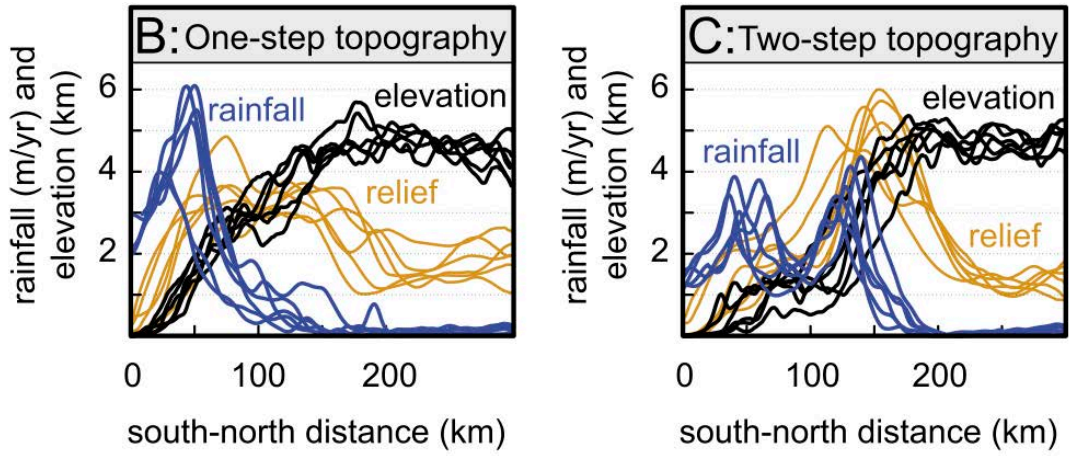

Figure 2.4 Relationship between rainfall and topography.

Across-strike profiles of elevation (black), relief (orange), and rainfall (blue). One-step topography (left) from NW India and Bhutan show one prominent rainfall peak at orographic barrier, corresponding with peak relief. Two-step topography from Central Himalaya exhibits less prominent two-peak rainfall pattern corresponding to the Lesser and Higher Himalayan orographic barriers. From *Bookhagen and Burbank, 2010*.

The dominance of monsoon rainfall extends to the region of approximately the Garhwal Himalaya or the Sutlej Valley in the northwestern Himalaya. West of these regions, the climate transitions into a regime with greater influence from the Winter Westerly system (e.g., *Barros et al.*, 2006; *Wang*, 2006; *Bookhagen and Burbank*, 2010; *Cannon et al.*, 2015). Corresponding to the greater influence of the Winter Westerlies is a higher contribution of snow and glacial melt to the annual river discharge in those areas (*Bookhagen and Burbank*, 2010).

Chapter 3: Understanding erosion rates in the Himalayan orogen : A case study from the Arun Valley

Abstract

Understanding the rates and pattern of erosion is a key aspect of deciphering the impacts of climate and tectonics on landscape evolution. Denudation rates derived from terrestrial cosmogenic nuclides (TCN) are commonly used to quantify erosion and bridge tectonic (Myr) and climatic (up to several kyr) timescales. However, how the processes of erosion in active orogens are ultimately reflected in ^{10}Be TCN samples remains a topic of discussion. We investigate this problem in the Arun Valley of eastern Nepal with 34 new ^{10}Be-derived catchment-mean denudation rates. The Arun Valley is characterized by steep north-south gradients in topography and climate. Locally, denudation rates increase northward, from <0.2 mm yr^{-1} to ~1.5 mm yr^{-1} in tributary samples, while mainstem samples appear to increase downstream from ~0.2 mm yr^{-1} at the border with Tibet to 0.91 mm yr^{-1} in the foreland. Denudation rates most strongly correlate with normalized channel steepness (R^2=0.67), which has been commonly interpreted to indicate tectonic activity. Significant downstream decrease of ^{10}Be concentration in the mainstem Arun suggests that upstream sediment grains are fining to the point that they are operationally excluded from the processed sample. This results in ^{10}Be concentrations and denudation rates that do not uniformly represent the upstream catchment area. We observe strong impacts on ^{10}Be concentrations from local, non-fluvial geomorphic processes, such as glaciation and landsliding coinciding with areas of peak rainfall rates, pointing toward climatic modulation of predominantly tectonically-driven denudation rates.

3.1 Introduction

Denudation, the removal of mass from the landscape, is the combined result of tectonic forces that expose rock at the surface and climatic forces that provide the erosive agents to remove it. An effort to understand the relationship

between the rates of denudation and the tectonic and/or climatic forces that drive denudation has been a main undertaking in Earth science in recent decades. Many theoretical and field studies have suggested a close link between climate and denudation rates in a variety of geodynamic settings (e.g., *Reiners et al.*, 2003; *Hales and Roering*, 2005; *Roe et al.*, 2008; *Moon et al.*, 2011; *Bookhagen and Strecker*, 2012a; *Ferrier et al.*, 2013a, 2013b; *Herman et al.*, 2013), ultimately resulting in characteristic landscapes in accord with climatic zonation (e.g., *Büdel*, 1982). In contrast, another group of studies has argued against a strong climatic influence on denudation rates in many orogens and emphasizes a more decisive role of tectonic processes in landscape evolution (e.g., *Riebe et al.*, 2001; 2004; *Burbank et al.*, 2003; *Safran et al.*, 2005; *Willenbring and von Blanckenburg*, 2010; *Godard et al.*, 2014; *Scherler et al.*, 2014). However, the timescales of these studies differ significantly, from tens (e.g., suspended sediment flux) to millions (e.g., thermochronometry) of years.

Over the last quarter century, the assessment of erosion processes using terrestrial cosmogenic nuclides (TCN) has been increasingly refined as a widely used method in geomorphology due to its ability to quantify catchment-mean denudation rates on 10^2 – 10^5 year timescales, thus bridging the gap between instrumentally-recorded erosion rates and rates obtained from thermochronology and the stratigraphic records of geologic archives (*Bierman and Steig*, 1996; *Brown et al.*, 1995; *Granger et al.*, 1996, *von Blanckenburg*, 2005; *Granger et al.*, 2013).. Several studies have used ^{10}Be concentrations in detrital sand samples to investigate how climate and/or tectonics influence denudation rates in mountain belts around the world (e.g., *Safran et al.*, 2005; *Bookhagen and Strecker*, 2012a; *Godard et al.*, 2014; *Scherler et al.*, 2014). However, the assumptions necessary to calculate catchment-mean denudation rates from a detrital river sand sample are frequently violated in climatically very dynamic, active tectonic environments, and the extent to which ^{10}Be concentrations reflect actual denudation rates is still under debate (e.g., *Lupker et al.*, 2012; *McPhillips et al.*, 2014; *Puchol et al.*, 2014).

Because it has been proposed as a location where tectonic-climate coupling might occur (e.g., *Molnar and England*, 1990; *Hodges et al.*, 2004; *Thiede et al.*, 2005a, 2005b; *Huntington et al.*, 2006; *Hirschmiller et al.*, 2014), the Himalaya represents an area where understanding denudation rates is of great scientific importance. The highest mountain range in the world, the Himalaya is rapidly and

actively uplifting and eroding (e.g., *Molnar and Tapponnier*, 1975; *Avouac*, 2003), and is characterized by an extreme and highly seasonal climate. The Indian Summer Monsoon (ISM) delivers large amounts of rainfall to the Himalaya, focused along the southern orographic front due to high topographic barriers (*Bookhagen and Burbank*, 2006; *Bookhagen and Burbank*, 2010). Monsoonal rainfall drives large discharge events and sediment fluxes toward the Indo-Gangetic foreland (*Wulf et al.*, 2010; 2012) and eventually into submarine fans and beyond (*Milliman and Syvitski*, 1992; *Clift et al.*, 2001; *Curray et al.*, 2002). Authors of recent studies of ^{10}Be TCN from the Himalaya have argued, however, that climate does not play a decisive role in driving denudation rates, which are instead controlled principally by tectonic deformation and uplift (e.g., *Godard et al.*, 2014; *Scherler et al.*, 2014).

The impact of climate on sediment flux and topography through variability of the ISM may have been stronger in the past (e.g., *Goodbred and Kuehl*, 2000; *Bookhagen et al.*, 2005a). Evidence exists for a stronger ISM in the early Holocene and a relatively weak ISM during the LGM and the present-day (e.g., *Prins and Postma*, 2000; *Thamban et al.*, 2002; *Fleitmann et al.*, 2003; *Bray and Stokes*, 2004; *Zhisheng et al.*, 2011). The early Holocene intensified monsoon was associated with a two-fold increase in sediment discharge to the Ganges-Brahmaputra fan (*Goodbred and Kuehl*, 2000), frequent large landslides in the orogen interior, and overall increased sediment flux in the NW Himalaya (*Bookhagen et al.*, 2005a). Such studies document the sensitivity of the Himalayan system to changes in regional climate and the surface-process regime.

In this study, we present 34 new ^{10}Be TCN catchment-mean denudation rates from the Arun Valley in eastern Nepal to understand how climatic and tectonic processes affect ^{10}Be TCN concentrations and the resulting denudation rate calculations. The north-south flowing Arun is the fourth largest trans-Himalayan river and traverses the orogen through a deeply incised, narrow gorge (Figure 3.1). The Arun Valley is characterized by steep topographic and climatic gradients perpendicular to the strike of the Himalaya. These distinct gradients allow for a robust analysis of different climatic and topographic factors that may influence ^{10}Be concentration in river sand samples and possibly control regional denudation rates.

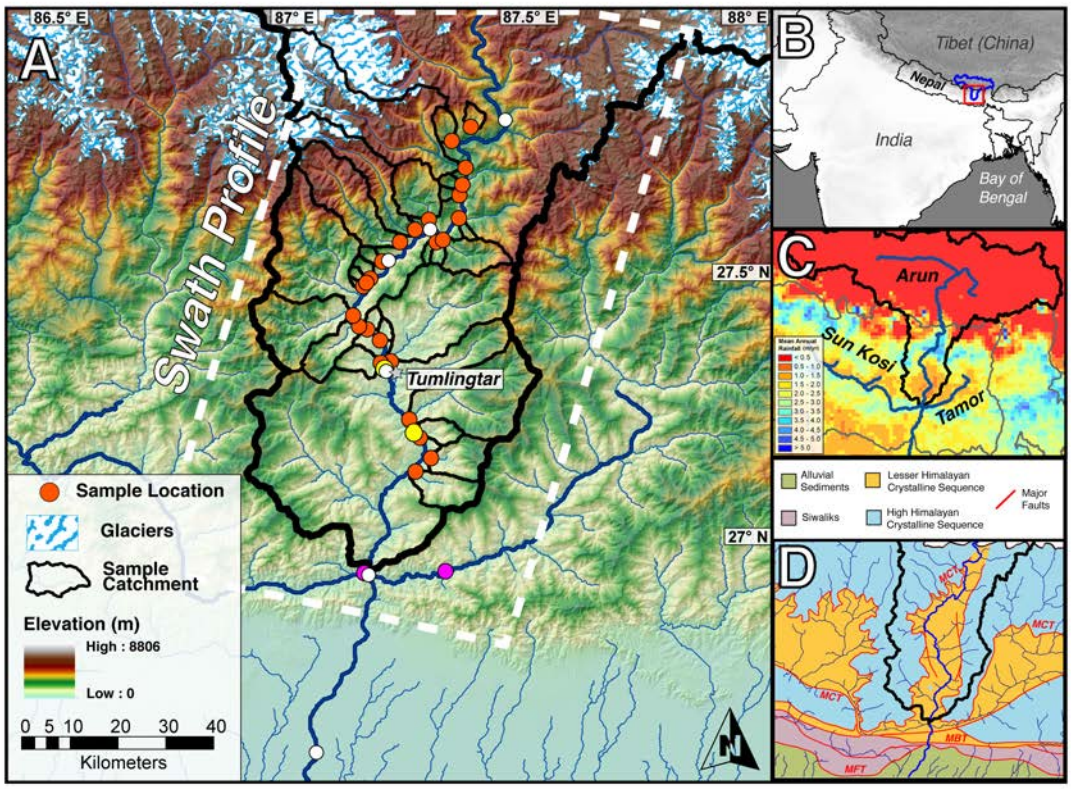

Figure 3.1 Overview of the Arun Valley study area.

Overview of study area in the Arun Valley, eastern Nepal. (A) Map of study area showing elevation from SRTM 90-m DEM, river network (dark blue), and glaciers from GLIMS glacier database (light blue/white) (GLIMS, 2005; http://www.glims.org/). Sample locations of ^{10}Be TCN sample sites for tributaries (red) are shown with associated watersheds outlined (black); along with mainstem (white), Sun Kosi and Tamor rivers (pink), and fluvial fill terrace (yellow) sample locations (cf. Table 3.1). Downstream of the confluence of the Arun, Sun Kosi, and Tamor rivers, the river is called the Sapt Kosi. The mainstem Arun watershed is shown by a thick black outline. The swath area used for Figure 3.3 is shown in dashed white lines. (B) The Arun Valley in the regional context; including area from (A) (red) and the entire Arun watershed, including area in Tibet (blue). (C) Mean annual rainfall (mm yr^{-1}) from calibrated TRMM 2B31 (*Bookhagen and Burbank*, 2010) showing double bands of high rainfall at the orographic fronts of the LH and HH and Sapt Kosi river network, including Arun, Sun Kosi, and Tamor (dark blue), and Arun watershed (black). Political boundaries are shown in gray for reference. (D) Geologic map of the study area after Grujic et al. (2011) showing major Himalayan lithologies and faults of eastern Nepal. MFT denotes Main Frontal Thrust, MBT Main Boundary Thrust, and MCT Main Central Thrust. Outline of the Arun watershed is shown in black.

3.2 Background

3.2.1 Climatic setting

Every year the ISM system delivers heavy, seasonal rainfall to the Himalaya as the Intertropical Convergence Zone (ITCZ) migrates northward during the boreal summer (*Charney*, 1969; *Gadgil*, 2003). The orographic barrier of the Himalaya focuses monsoonal rainfall along its southern flank, where mean annual rainfall locally exceeds 5 m yr^{-1} (Figure 3.1c) (*Bookhagen and Burbank*, 2010). The Arun Valley is located relatively close to the Bay of Bengal (Figure 3.1b,c) and thus the main ISM moisture source. Weather stations maintained by the

Nepal Department of Hydrology and Meteorology in the Arun record approximately 60% of annual rainfall during the peak ISM months (June through September); 80-90% of annual rainfall occurs from May through October (cf. *Bookhagen and Burbank*, 2010). Because of the deeply incised, N-S oriented gorge, moisture is funneled through the Arun Valley northward into Tibet, resulting in greater rainfall in the upper sectors of the valley than on the surrounding higher-elevation areas (Figure 3.1c). Winter precipitation is primarily focused in the high-altitude regions (*Bookhagen and Burbank*, 2010; *Wulf et al.*, 2010) and snowfall is common in these areas (*Carpenter and Zomer*, 1996). Reliable snowfall data from gauging stations, however, is not available in the Arun region as weather stations are principally located at low elevations not affected by snowfall. Bookhagen and Burbank (2010) calculated the snowmelt contribution of major Himalayan rivers across the Himalayan orogen and found that approximately 25% of total discharge in the Arun is related to snowmelt, as opposed to over 50% in the Western Himalaya.

3.2.2 Geologic and tectonic setting

Originating in Tibet, the Arun flows southward through the Himalayan orogen before joining the Sapt Kosi and the Ganges rivers in the foreland. The course of the river exposes a natural cross section through the mountain belt: From the sedimentary Tethyan series in Tibet (TS), through the Greater or High Himalayan Crystalline (HHC), the Lesser Himalayan Crystalline (LHC), the Siwaliks, and finally to the alluvial plains of the Gangetic foreland (*Schelling*, 1992; *Grujic et al.*, 2011). An aerially extensive tectonic window, identified by Meier and Hiltner (1993) as the Arun Tectonic Window, exposes LHC rocks below the Main Central Thrust (MCT) along the course of the Arun (Figure 3.1d). The northern extent of this window and the location of the MCT are poorly constrained (e.g., *Schelling*, 1992). The Arun Tectonic Window corresponds to a large anticline (*Wager*, 1937), which Montgomery and Stolar (2006) suggested to result from focused bedrock incision of the Arun.

The lithology in the study area is dominated by crystalline metamorphic rocks, principally from the HHC and LHC. The LHC units in the Arun Valley, as mapped by Schelling (1992), are metasediments (e.g., metaquartzite, slate, phyllite,

metagraywacke) and augengneiss. HHC units are comprised of migmatites, paragneiss, and granites. No extensive carbonate or volcanic deposits are exposed and all mapped lithologic groups are predominantly quartz-bearing. Because the Arun Tectonic Window follows the Arun Valley northward, we do not observe discrete variations in lithology perpendicular to strike within our study area (Figure 3.1d, Figure 3.2).

3.2.3 Geomorphic setting

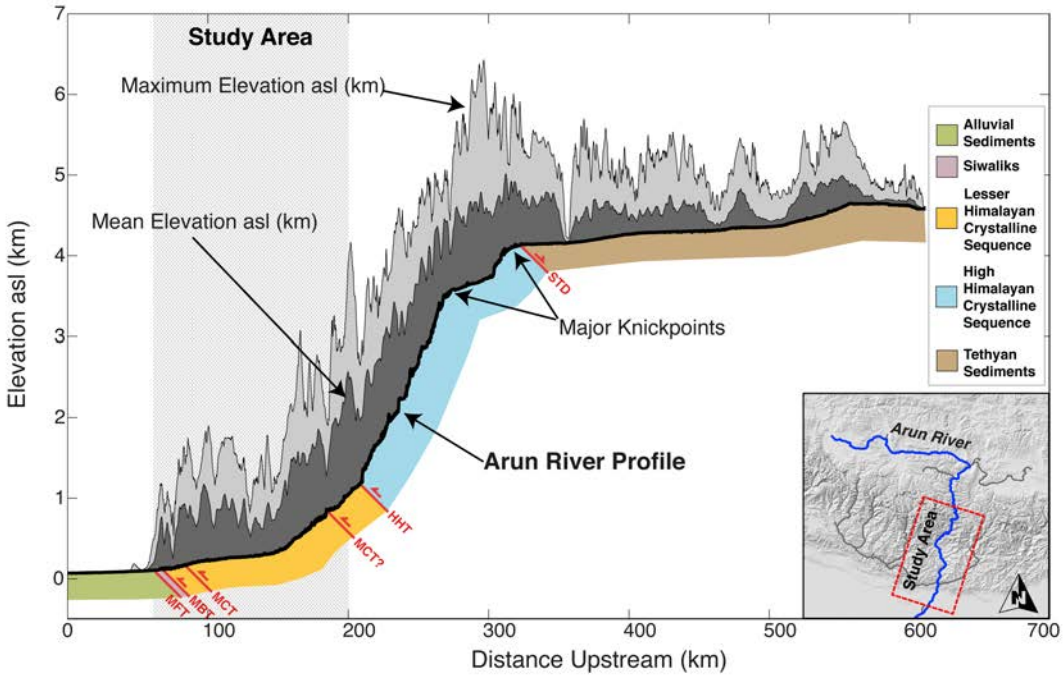

Figure 3.2 Longitudinal profile of Arun River

From the Ganges plain in the south to its source in southern Tibet. The river profile (black) is shown with mean elevation (dark gray) and maximum elevation (light gray) from a 1.5 km swath centered along the course of the river. The two large knickzones are easily visible in the river profile, as well as the transition from a steep graded profile (θ=0.45) to shallow profile (θ=0.79) downstream and upstream of the knickzones, respectively. Surface lithology along the Arun River after Grujic et al. (2011); major fault locations after Schelling (1992) and Grujic et al. (2011). The study area is shown in hatched gray. Inset shows map view of the region, with the Arun trunk stream highlighted in blue.

As it drains the Himalaya, the Arun displays a steep, graded channel profile in a narrow valley (Figure 3.2). Two large slope-break knickzones north of the Arun gorge, approximately corresponding to the location of the Southern Tibetan Detachment (STD), separate the Himalayan Arun from the Tibetan section of the river, known locally as the Pum Qu. Similar knickzones of tectonic origin are observed in many trans-Himalayan rivers along strike (e.g., *Seeber and Gornitz*,

1983). Above these knickzones the river has a shallow profile for the remainder of its upstream course and a broad, flat valley. Several fluvial fill terraces in the lower and middle reaches of the Arun have been mapped by Lavé and Avouac (2001), but few are preserved in the upper reaches of the valley. We observed several strath terraces and hanging valleys, particularly in the upper sections of our study area approaching the Tibetan border.

The topography of the Arun Valley is comprised of three principal topographic sectors (Figure 3.3a): the Lesser Himalaya (LH), with an average elevation of ~2 km asl and a mean hillslope angle of ~20˚; the Higher Himalaya (HH), where mean elevation rises above 4 km asl and peaks are in excess of 8 km asl, with a mean hillslope angle of ~30˚; and a topographic transition zone between the Lesser and Higher Himalaya, first identified in other areas along strike of the mountain belt as the Physiographic Transition Zone (PT_2) (*Hodges et al.*, 2001), marking a sharp break in topography.

In the Higher Himalaya, the Arun Valley hosts several glaciers (GLIMS, 2005; http://www.glims.org/). Larger valley glaciers are predominantly in western tributaries of the Arun. To the east, several small cirque glaciers exist in the Ama Drime and Higher Himalaya, but no large valley glaciers currently occupy these watersheds. In the Nepalese section of the Arun Valley, cirque and valley glaciers exist in the upper reaches of the northernmost tributaries flowing into the Arun, but are less prominent than on the northern flanks of the Higher Himalaya, where extensive glaciation extends down from the northern slopes of the Sagarmatha/Mt. Everest and Makalu regions. Valley morphology suggests that past glaciation was more extensive in medium to large high-altitude tributaries, but there is no evidence of glaciers reaching the mainstem Arun.

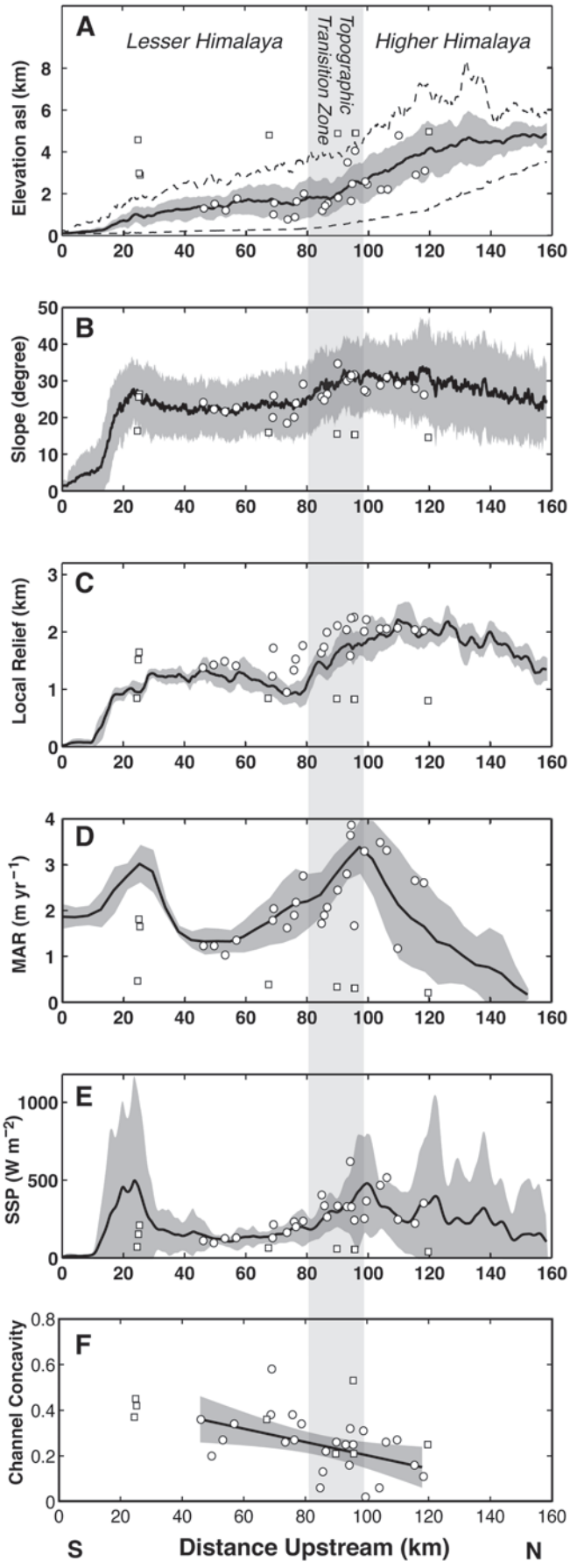

Figure 3.3 Arun swath profiles.

Swath profiles (from swath area in Figure 3.1) of: (A) elevation, with Lesser Himalaya, topographic transition zone (shaded gray), and Higher Himalaya denoted; (B) slope; (C) 3-km radius relief; (D) mean annual rainfall (*Bookhagen and Burbank*, 2010) ; (E) TRMM-weighted specific stream power (SSP); and (F) channel concavity from χ-analysis for each sampled tributary and mainstem location. Values are averaged across a 75-km wide swath area, chosen to include all major tributaries to the Arun River in our study area. Mean swath values are shown in black with $\pm 1\sigma$ in shaded gray. Catchment-mean values from all sampled tributaries (circles) and mainstem locations (squares) are shown along swath. Concavity values (F) are shown with linear regression of tributary concavity values and upstream distance; shaded gray region represents the 95% confidence bounds. The topographic transition zone is shown in all panels by the light gray bar.

3.3 Methods

3.3.1 Climatic Data and Analysis

Rainfall in the Arun Valley was characterized using remotely sensed data from the Tropical Rainfall Measurement Mission (TRMM). We used the calibrated 12-year average mean annual rainfall product TRMM 2B31

(*Bookhagen and Burbank*, 2010) with a nominal spatial resolution of 5 × 5 km. Additionally, we used the National Snow & Ice Data Center (NSIDC) Global Land Ice Measurements from Space (GLIMS) database to define the location of present-day glaciers within our study area (GLIMS, 2005; http://www.glims.org/). Due to insufficient data, we do not account for snowfall or glacial melt in any of our climate-based analysis. Because of this, we acknowledge that metrics that depend on stream discharge, such as specific stream power (below), may be underestimated in high altitude catchments affected by snowfall.

We calculated specific stream power (SSP), a measure of potential stream energy per unit area based on the stream power model (e.g., *Whipple and Tucker*, 1999; *Lague*, 2014), following Bookhagen and Strecker (*Bookhagen and Strecker*, 2012a). SSP (ω, W m^{-2}) incorporates climatic and topographic factors, such that:

$$\omega = \frac{\gamma \times Q \times S}{w} \tag{3.1}$$

where γ is the specific weight of water (9819 N m^{-3}), Q is discharge (m^3 s^{-1}), S is the local bed slope (m m^{-1}), and w is the width of the channel (m). To account for the large spatial variations in rainfall in the Arun Valley, and therefore presumably runoff, we determined discharge based on both upstream area and TRMM-derived rainfall. We calculated SSP for every 90-m pixel in the DEM and have used an 11-pixel (~1 km) moving average channel-slope filter to remove outliers. SSP values were explicitly calculated from channel slopes. Channel width was defined using a simple scaling model, such that channel width was assumed to increase proportionately to discharge, following a power-law relationship with an exponent of 0.4 (*Knighton*, 1999; *Whipple*, 2004; *Craddock et al.*, 2007).

3.3.2 Topographic and geologic data and analysis

Topographic analysis was performed on the 90-m resolution Shuttle Radar Topography Mission (SRTM) digital elevation model (DEM) v4.1 provided by CGIAR-CSI (*Jarvis et al.*, 2008, http://srtm.csi.cgiar.org/). The stream network and upstream area was determined after first filling sinks and carving sills in the 90-m DEM (*Schwanghart et al.*, 2013). We calculated several metrics to characterize topography in the Arun Valley using a combination of standard GIS

techniques and TopoToolbox v2 (*Schwanghart and Scherler*, 2013). Hillslope angle (degrees) and gradient (m m^{-1}) were calculated for each 90-m pixel based on its eight surrounding neighbors. Local relief was calculated for each pixel based on 1-km and 3-km radius averaging windows. Lithology was classified using the map by Schelling (1992). As sampled catchments lie entirely within the LHC and HHC units (ARU-12-11 contains 3% in Tethyan sediments), we quantified catchment lithology by percent area in the High Himalayan Crystalline units (%HHC). We did not perform a more detailed analysis between units within the HHC or LHC.

3.3.2.1 Channel Concavity and Steepness

Channel concavity is an integral part of the stream power model for bedrock rivers (e.g., *Whipple and Tucker*, 1999; *Whipple,* 2004; *Wobus et al.*, 2006) that describes channel evolution through time and varies for different rivers based on a variety of natural conditions (e.g., lithology). We calculated channel concavity for the mainstem Arun and each sampled tributary by: (1) standard slope-area regression (e.g., *Flint*, 1974; *Wobus et al.*, 2006), and (2) least-squares regression of the χ-transformed stream network (*Perron and Royden*, 2013; *Royden and Perron*, 2013). Because orographic rainfall, as observed in the Arun Valley, has the potential to affect channel concavity in steady-state river profiles (e.g., *Roe et al.*, 2002), we additionally performed the slope-area and χ-analysis using a TRMM rainfall-weighted flow accumulation grid.. The TRMM-weighted flow accumulation grid is calculated using the routines of TopoToolbox v. 2 (*Schwanghart and Scherler*, 2013) and results in upstream areas that are weighted to be proportionately "larger" in regions with higher rainfall rates, and proportionately "smaller" in regions with lower rainfall rates. In both cases, we separately calculated the channel concavity for the entire stream network and for the trunk stream in each catchment.

Normalized channel steepness (k_{sn}) (e.g., *Wobus et al.*, 2006) was calculated for the Arun fluvial network in our study area for every 90-m pixel in the channel network. Local channel gradient was calculated for each pixel, then divided by upstream area to calculate channel steepness (k_s); we then normalize channel steepness using: (1) the standard reference concavity of θ=0.45 (e.g., *Wobus et al.*, 2006); and (2) the mean concavity value derived from the χ-analysis

of all tributaries (θ=0.23 ± 0.14). We additionally calculated k_{sn} using a TRMM-weighted flow accumulation grid to account for the potential impact of spatially-inhomogeneous rainfall, assuming that regions experiencing higher rainfall may have higher denudation rates within the basin. TRMM-weighted k_{sn} was normalized using: (1) θ=0.45 and (2) θ=0.20 ± 0.14, the mean concavity value from the TRMM-weighted χ-analysis. For all channel steepness indices, catchment-mean k_{sn} was calculated for the channel network upstream of the sample location.

3.3.3 ^{10}Be TCN-Derived Denudation Rates

Basin-wide denudation rates were estimated based on in-situ ^{10}Be in fluvial river sands (*Brown et al.*, 1995; *Bierman and Steig*, 1996; *Brown et al.*, 1995; *Granger et al.*, 1996). In total, we collected and analyzed 34 samples in the Arun Valley, from the border with India in the south to the border with Tibet (China) in the north. Our primary sample targets were: (1) the mainstem Arun, sampled in intervals along its N-S course; (2) tributaries to the Arun, ranging in size from <10 km^2 to >1,000 km^2; and (3) the Sun Kosi (ARU-11-27) and Tamor (ARU-11-25) rivers near their confluence with the Arun. Samples were taken from fresh sand banks on active channels of the mainstem Arun and its tributaries. The only exception was ARU-11-12; this sample was taken from a recently abandoned or high water channel as the active channel was not accessible. In total, 7 samples were collected from the mainstem Arun, one sample each from the Sun Kosi and Tamor, and 25 samples from tributaries to the Arun. Sample site selection was also dictated by accessibility, limiting our ability to sample some major tributaries. In addition to the 34 samples collected for present-day denudation rates, we sampled paleo-river sands from a large fill terrace at Tumlingtar (ARU-12-21, ARU-12-22) and from one smaller terrace in the lower reaches of the Arun (ARU-11-21) to quantify ^{10}Be concentrations in transiently stored sediments.

3.3.3.1 Sample preparation and processing

Samples were prepared at the University of Potsdam and the University of California – Santa Barbara following standard procedures (e.g., *Bookhagen and Strecker*, 2012a). A low-ratio ^{9}Be spike (^{10}Be/^{9}Be ratio of ~1×10^{-15}) was added to the cleaned quartz and samples were dissolved in hydrofluoric acid. Ion-exchange

chromatography was used to extract Beryllium from the dissolved samples (*von Blanckenburg et al.*, 2004; *Bookhagen and Strecker*, 2012a). Samples were sent to CAMS, Lawrence Livermore National Laboratory, USA for accelerator mass spectrometry measurements. Ratios of $^{10}Be/^{9}Be$ were normalized using the 07KNSTD3110 standard ($^{10}Be/^{9}Be$ ratio of 2.85×10^{-12}) (*Nishiizumi et al.*, 2007).

3.3.3.2 Calculation of catchment-mean denudation rates

Production rates of cosmogenic ^{10}Be in Arun tributary catchments were calculated for every 90-m pixel of the SRTM DEM, including the effects of altitude, latitude, topography, and glaciation (see below). The same procedure was used for mainstem Arun, Sun Kosi, and Tamor samples for every 1-km pixel using the USGS GTOPO30 global DEM (https://lta.cr.usgs.gov/gtopo30/). Topographic shielding was calculated following Dunne et al. (1999). We used the Lal/Stone scaling procedure (*Lal*, 1991; *Stone*, 2000), which takes time-dependent muogenic production and non-dipole geomagnetic effects into account (*Balco et al.*, 2008), and the revised ^{10}Be half-life of 1.387±0.016 Myr (*Chmeleff et al.*, 2010; *Korschinek et al.*, 2010). $^{10}Be/^{9}Be$ concentrations were corrected using the mean of 8 laboratory blanks ($1.43 \times 10^{-14} \pm 1.23 \times 10^{-15}$). ^{10}Be concentrations were converted to erosion rates using the MATLAB-functions of the CRONUS-Earth online calculator version 2.2 (*Balco et al.*, 2008) in an iterative scheme provided by Scherler et al. (2014).

3.3.3.3 Ice shielding and glaciation

Recent studies have shown that present-day and past glaciations reduce ^{10}Be concentrations in detrital quartz and can, when unaccounted for, result in apparent denudation rates that are significantly overestimated (*Godard et al.*, 2012; *Glotzbach et al.*, 2013). To mitigate this effect, we applied an ice shielding mask to production rate calculations based on present-day glacier cover from the GLIMS glacial database; this assumes that the production rate in ice-covered areas of the catchment is zero, and all ^{10}Be in the detrital sample is derived from ice-free surfaces. The ice shielding mask was applied to three tributary catchments (ARU-11-14, ARU-11-15, ARU-12-11) where glaciers are currently present, the mainstem Arun, the Sun Kosi, and the Tamor. Currently, there is insufficient data about the glacial history of the Arun Valley available to correct for past glacial coverage (e.g., *Glotzbach et al.*, 2013).

3.3.4 Comparison of topographic and climatic metrics and denudation rates

To better understand regional influences on denudation rates, we performed a suite of ordinary least-squares (OLS) regressions between our TCN denudation rates and catchment-mean topographic and climatic metrics. We excluded outliers (BBRS01, ARU-12-09, ARU-12-19A), where we observe evidence of recent voluminous landsliding (see section 3.4.3.4), and presently glaciated tributaries. Glaciated tributaries were excluded from regression analysis because many of the topographic metrics used (e.g., k_{sn}, SSP) assume fluvial processes and are not applicable to glaciated catchments. Due to the high incidence of landsliding (see section 4.4.4) we removed ARU-11-10 and ARU-11-11 from the regression analysis. ARU-12-06 is a small tributary with a pronounced knickpoint cutting through a perched low-relief topography that may still be subjected to the impact of a previous erosion regime and we therefore remove ARU-12-06 from the regressions.

Catchment topography has traditionally been characterized by the catchment mean or median value of a chosen metric (e.g., relief, k_{sn}). Despite this common assumption, catchment topography is often not normally distributed, especially in transient landscapes. In order to perform a more robust comparison between denudation rates and catchment climate and topography, we extend our regression analysis beyond the catchment mean or median metric value. To do this, we calculate every fifth percentile from the 10^{th} to 90^{th} percentile of the data and use percentile values to perform multiple OLS regressions of our catchment-mean denudation rates against catchment topographic and climatic metrics. Additionally, we performed Lilliefors (*Lilliefors*, 1967; 1969) and skewness tests to decide if catchment metrics are normally or non-normally distributed at the 95% confidence level.

3.3.5 ^{10}Be Mass Balance Calculations

Standard TCN denudation rate calculation assumes that a fluvial sand sample is a uniform representative sample of the entire upstream area. Models of downstream sediment transport typically assume that particles <2 mm diameter are kept in suspension in high-energy mountain rivers (e.g., *Sklar et al.*, 2006;

Chatanantavet et al., 2010), further suggesting that a detrital sand sample would be uniformly sourced from the upstream area. We test this assumption by comparing ^{10}Be concentrations from mainstem Arun samples from upstream regions on the border with Tibet to ^{10}Be concentrations from the confluence of the Arun, Sun Kosi, and Tamor. We performed a simple mass balance calculation to determine if the changes in ^{10}Be concentration can be achieved under the assumption of uniform upstream sediment sourcing by solving for: (1) variable mass flux from the southern flanks of the Himalaya; and (2) variable ^{10}Be concentration in the southern flanks of the Himalaya:

$$Conc._{\text{Confluence}} = \frac{Area_{\text{Tibet}} MF_{\text{Tibet}} Conc._{\text{Tibet}} + Area_H MF_H Conc._H}{Area_{\text{Confluence}} MF_{\text{Confluence}}} \quad (3.2)$$

where 'Tibet' represents the area upstream of northernmost sample, 'Confluence' represents the area upstream of the southernmost sample before the Sapt Kosi confluence, 'H' denotes the Himalaya between the border with Tibet and the Sapt Kosi confluence, 'Conc.' is measured ^{10}Be concentration in the detrital sample, and MF represents the mass flux (g cm^{-2} yr^{-1}). To solve for mass flux, we assume that the mean ^{10}Be concentration from Arun tributaries is representative of the ^{10}Be concentration of the Himalaya in the region. To solve for variable ^{10}Be concentration, we assume that $MF_H = MF_{\text{Confluence}} - MF_{\text{Tibet}}$.

3.4 Results

3.4.1 Topography and climate

In general, elevation and topographic steepness metrics (e.g., hillslope angle, local relief, channel steepness) increase from south to north across the Arun Valley (Figure 3.3, Table 3.1). Mean hillslope angle across the study area ranges from <5˚ in the alluvial plain to >30˚ in the Higher Himalaya (Figure 3.3b); 3-km radius relief similarly increases from <100 m in the alluvial plain to ~1 km in the LH, then sharply increases at the topographic transition zone into the HH, where it exceeds 2 km (Figure 3.3c). Discrete increases in hillslope angle and local relief are observed at both the LH and HH orographic barrier. Sampled catchments are located in the Lesser and Higher Himalaya where hillslope angle and relief are

moderate to high. In sampled fluvial tributaries, mean hillslope angles range from 18˚ to 35˚; 3-km relief ranges from 876 m to 2261 m (Figure 3.3, Table 3.1).

Channel concavity derived from χ-analysis of the mainstem Arun in our study area indicates a generally graded river profile with a concavity of 0.451 until the first large knickpoint in southern Tibet (Figure 3.2). The channel concavity of tributary streams decreases steadily from 0.57 in the south to 0.02 in the north (Table 3.1, Figure 3.3f), indicating more uniformly steep channels approaching Tibet, Tributary channel concavity calculated from TRMM-weighted flow accumulation does not significantly differ from the non-weighted concavity values at the 95% confidence level. Unlike hillslope angle and relief, no discrete break in concavity values is observed at the topographic transition zone.

Normalized channel steepness is low throughout the Lesser Himalaya in the mainstem Arun and tributary channels, but increases rapidly at the topographic transition zone (Figure 3.4). Throughout the Higher Himalaya, k_{sn} remains high; low values in the upper reaches of some tributaries correspond to glacial valley morphology. Catchment-mean values of k_{sn} for fully fluvial sample tributaries range from 87 $m^{0.9}$ to 342 $m^{0.9}$, normalized by θ=0.45; for θ=0.23 catchment-mean k_{sn} values range from 2.78 $m^{0.46}$ to 11.34 $m^{0.46}$ (Table 3.1). Minimum and maximum k_{sn} values correspond to small tributaries (<20 km^2) that lie entirely in the LHC and HHC units, respectively.

TRMM-weighted flow accumulation results in higher k_{sn} values throughout the HH and LH; ranging from 109 $m^{0.9}$ to 602 $m^{0.9}$ normalized by θ=0.45; and 1.92 $m^{0.4}$ to 9.17 $m^{0.4}$ normalized by θ=0.20 (see Table S3.1). TRMM-weighted k_{sn} has a strong, positive linear correlation with unweighted k_{sn} (R^2=0.88, 0.97 for standard reference concavity (θ=0.45) and χ-determined channel concavity respectively).

Mean annual rainfall follows a steep, two-tiered gradient (cf. section 2.1), increasing from ~2 m yr^{-1} in the alluvial plain to >3 m yr^{-1} at the front of the LH/Siwaliks, then decreases rapidly to <2 m yr^{-1} in the rain shadow of the LH orographic barrier; rainfall steadily increases over the next 40 km approaching the HH orographic barrier to a peak of ~4 m yr^{-1}, then decreases into Tibet (Figure 3.3d). Within our sampled catchments, catchment-mean annual rainfall ranges from 1.03 m yr^{-1} (ARU-11-22) directly north of the LH orographic barrier to 4.22 m yr^{-1} in the Higher Himalaya (ARU-12-06).

Table 3.1 Sample information and basin properties

Sample ID	***Sample Type***	***Easting (m) UTM Z45N***	***Northing (m) UTM Z45N***	***Mean Basin Elevation (m asl)***	***Catchment Area (km^2)***	***Total Elevation Range (m)***
ARU-11-01	ARUN	518661.23	3020907.28	4769.00	31260.29	8525.00
ARU-11-13	ARUN	519112.20	3043306.04	4848.00	30400.97	8236.00
ARU-11-16	ARUN	526948.20	3049019.84	4869.00	29942.76	8046.00
ARU-11-26	ARUN	515397.12	2977951.82	4544.00	33500.94	8678.00
ARU-11-28	ARUN	493136.31	2933320.99	3849.00	57979.93	8732.00
ARU-12-03	ARUN	527108.00	3049168.00	4869.00	29942.76	8048.00
ARU-12-15	ARUN	544346.00	3073168.00	4936.00	28407.20	6888.00
ARU-11-25	TAMOR	531534.41	2978676.31	2869.63	5886.36	2468.00
ARU-11-27	SUN KOSI	514554.34	2978354.97	2958.08	18100.00	3406.00
ARU-11-03	TRIBUTARY	520055.58	3022570.94	1540.16	387.60	1516.00
ARU-11-04	TRIBUTARY	517817.46	3026936.09	761.96	11.48	378.00
ARU-11-05	TRIBUTARY	515173.14	3029284.10	867.32	11.84	631.00
ARU-11-06	TRIBUTARY	513172.29	3029874.40	1606.73	74.19	1023.00
ARU-11-07	TRIBUTARY	512159.53	3032217.16	1979.48	204.45	1130.00
ARU-11-10	TRIBUTARY	514298.52	3038272.85	1173.99	2.67	384.00
ARU-11-11	TRIBUTARY	515765.77	3040048.33	1525.37	10.55	724.00
ARU-11-12	TRIBUTARY	518668.49	3043478.81	1787.03	13.20	699.00
ARU-11-14	TRIBUTARY	522720.87	3046536.67	3476.99	218.09	1328.00
ARU-11-15	TRIBUTARY	525012.39	3049015.72	4027.25	187.86	1595.00
ARU-11-18	TRIBUTARY	517935.99	3022266.40	997.13	33.25	742.00
ARU-11-20	TRIBUTARY	523924.44	3010395.96	1744.75	313.97	834.00
ARU-11-22	TRIBUTARY	526184.15	3006666.68	1177.50	35.11	817.00
ARU-11-23	TRIBUTARY	527336.27	3003012.87	1502.34	88.91	887.00
ARU-11-24	TRIBUTARY	529786.00	2999539.00	1280.30	84.19	706.00
ARU-12-01	TRIBUTARY	531001.00	3047672.00	1644.76	8.35	1431.00
ARU-12-02	TRIBUTARY	534908.00	3048053.00	2455.14	81.67	3855.00
ARU-12-06	TRIBUTARY	534070.00	3052975.00	2420.55	8.53	2128.00
ARU-12-08	TRIBUTARY	534426.00	3057465.00	2170.62	8.87	1938.00
ARU-12-09	TRIBUTARY	535079.00	3059611.00	2193.45	10.29	2248.00
ARU-12-11	TRIBUTARY	535917.00	3063263.00	4757.83	470.11	7231.00
ARU-12-12	TRIBUTARY	525213.98	3068834.00	2872.28	27.86	2584.00
ARU-12-13	TRIBUTARY	536772.00	3071756.00	3070.31	16.27	1999.00
ARU-12-19/A	TRIBUTARY	528040.00	3052286.00	2563.93	102.84	3491.00
BBRS01	TRIBUTARY	514886.16	3039168.71	1403.35	9.01	570.00

Table 3.1. Sample information and basin properties.

Mean 1-km Relief (m)	*Mean 3-km Relief (m)*	*Mean Hillslope Angle (°)*	*Channel Concavity* [a]	*Mean k_{sn} ($m^{0.9}$)* [b]	*Mean k_{sn} Rainfall-weighted ($m^{0.9}$)* [c]	*Mean SSP Rainfall-weighted (W/m^2)* [d]	*Mean TRMM2B21 Annual Rainfall (m/yr)*
416.36	841.30	15.90	0.36	235.40	366.25	63.18	0.38
412.15	832.91	15.50	0.21	411.23	441.69	57.48	0.33
408.62	825.67	15.30	0.53	318.60	512.36	53.46	0.30
416.38	842.12	16.30	0.37	156.02	203.82	69.73	0.46
559.53	1121.50	20.50	0.37	25.86	38.36	124.84	1.03
408.62	825.67	15.30	0.21	318.60	512.36	53.46	0.30
397.33	800.98	14.50	0.25	365.71	162.39	38.36	0.20
837.73	1648.68	26.38	0.42	283.63	329.67	209.50	1.65
767.19	1517.77	25.57	0.45	299.96	341.25	151.62	1.81
819.34	1718.73	25.89	0.58	191.20	300.08	212.45	2.04
526.26	945.14	18.41	0.26	87.47	109.22	163.36	1.62
634.38	1330.67	20.06	0.38	127.90	168.70	231.59	1.90
753.74	1527.71	23.90	0.27	212.53	296.88	198.39	2.18
919.51	1761.27	29.17	0.34	236.14	375.32	234.58	2.76
858.27	1637.31	25.56	0.06	163.82	211.86	404.50	1.72
885.82	1994.85	26.34	0.22	255.86	359.67	263.04	2.07
1158.52	2110.22	34.78	0.26	235.87	352.91	333.84	2.45
983.76	2037.86	29.96	0.25	325.63	428.38	329.57	2.80
1109.26	2261.01	31.67	0.25	344.25	382.11	242.46	1.67
620.36	1228.03	19.96	0.38	140.91	185.96	127.51	1.79
720.16	1412.96	22.70	0.34	223.20	275.93	127.60	1.35
706.60	1487.80	21.60	0.27	191.39	197.80	123.93	1.03
700.26	1424.97	22.17	0.20	219.21	250.31	96.07	1.23
694.83	1377.37	24.16	0.36	191.10	215.03	108.75	1.23
691.28	1586.03	30.80	0.16	189.48	332.31	619.50	3.65
1052.03	2241.86	31.46	0.32	293.83	533.85	328.12	3.87
975.46	2214.09	26.96	0.02	285.21	545.28	365.63	4.22
968.00	2057.83	28.84	0.06	342.21	601.97	468.01	3.49
1031.90	2056.13	31.04	0.26	243.63	418.26	516.88	3.32
1010.75	2071.29	29.01	0.27	297.09	314.20	246.15	1.17
962.85	2036.90	27.93	0.16	292.02	433.36	221.28	2.66
887.10	2029.00	26.21	0.11	311.00	475.30	351.75	2.61
913.58	2012.41	27.40	0.31	292.67	479.49	252.16	3.30
808.03	1733.43	24.71	0.13	223.87	302.95	335.84	1.90

a Values calculated using least square regression of the chi-transformed stream network [Perron and Royden, 2013; Royden and Perron, 2013].

b Values calculated using standard channel concavity of θ=0.45.

c Values calculated using standard concavity of θ=0.45 and flow-accumulation grid weighted by mean annual rainfall from TRMM (Tropical Rainfall Measurement Mission) product 2B31.

d Values calculated using flow-accumulation grid weighted by mean annual rainfall from TRMM (Tropical Rainfall Measurement Mission) product 2B31.

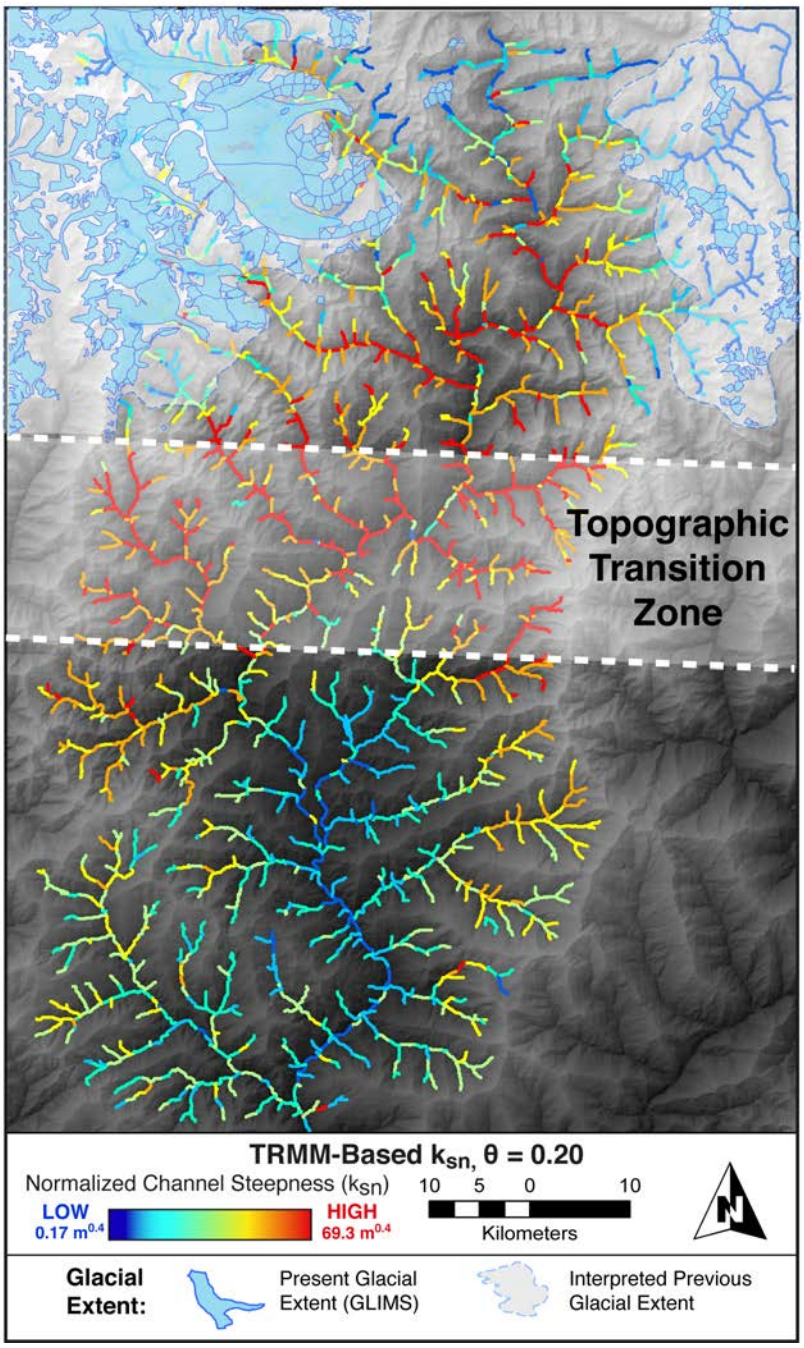

Figure 3.4
Normalized channel steepness.

TRMM-weighted k_{sn} (θ=0.20). Theta values are derived from the mean tributary channel concavity values from χ-analysis. Values of k_{sn} were calculated using the 90-m SRTM DEM for every pixel in the stream network, then averaged over 1-km long stream segments. All k_{sn} calculations follow a similar pattern as shown, with relatively low ksn values in the LH, a steep increase in the topographic transition zone, and a continuation of high k_{sn} values in the HH. Present-day glacial extent based on the GLIMS Glacier Database and the authors' interpretation of previous glacial extent is shown in blue. Normalized channel steepness values are low in these regions corresponding to glacial valley morphology.

TRMM-weighted SSP follows a similar pattern to mean annual precipitation (Figure 3.3e), with peaks of ~500 W m^{-2} at the LH and HH orographic barriers and variably high values (200 – 500 W m^{-2}) throughout the HH. A six-fold range of catchment-mean SSP values is observed in sampled tributaries, with catchment-mean SSP ranging from 104 W m^{-2} in the Lesser Himalaya to 620 W m^{-2} (Table 3.1) at the topographic transition zone, where rainfall and channel slopes are high.

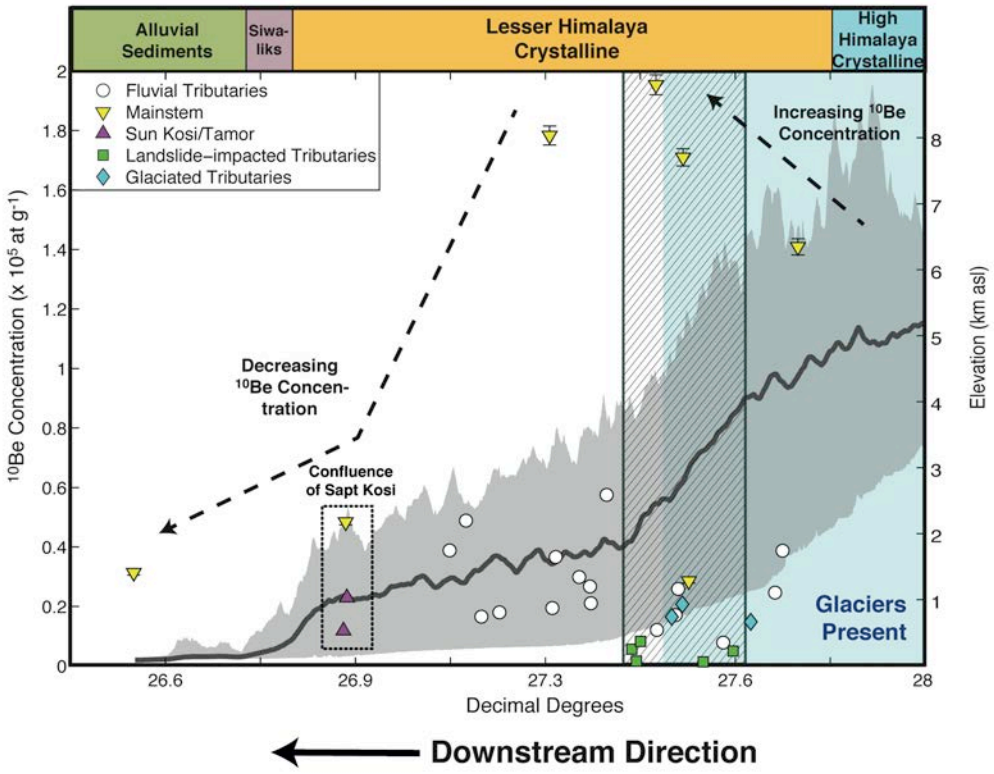

Figure 3.5 ^{10}Be concentration results

^{10}Be concentration from mainstem Arun (yellow triangle), Sun Kosi and Tamor Rivers (purple triangle), fluvial tributaries (white circle), glaciated tributaries (blue diamond), and landslide-impacted tributaries (green square). Lithology along the Arun River from *Grujic et al.*, 2011. Mean elevation is shown in black with min/max elevation in shaded gray, taken from a 75-km swath along the Arun Valley. Glaciated regions of the Higher Himalaya are shaded blue. A region of marked landsliding is shown as gray hatch. Note the increasing ^{10}Be concentration south of the Tibetan Plateau through the HHC and the decreasing ^{10}Be concentration in the LH, which we associated with downstream fining of material derived from the Tibetan Plateau.

3.4.2 ^{10}Be concentration in river-sediment samples

Sample ^{10}Be concentrations are recorded in Table 3.2 and Figure 3.5. We observe two main signals in mainstem Arun ^{10}Be concentration: (1) a high ^{10}Be concentration in the north of the study area; and (2) a low ^{10}Be concentration in the lower reaches of the Arun and Sapt Kosi. Downstream ^{10}Be concentrations in the mainstem Arun are similar to ^{10}Be concentrations from tributaries in the Higher and Lesser Himalaya, as well as low ^{10}Be concentrations observed from the Sun Kosi and Tamor rivers. Tributary ^{10}Be concentrations are an order of magnitude lower than the northern, high ^{10}Be mainstem Arun samples and show a northward decrease from the LH to HH. Within the tributaries, the lowest ^{10}Be concentrations are observed within the transition to the Higher Himalaya and in presently glaciated catchments.

3.4.3 ^{10}Be catchment-mean denudation rates

3.4.3.1 Mainstem Arun, Sun Kosi, Tamor, and Sapt Kosi

Catchment-mean denudation rates in the mainstem Arun decrease from the confluence of the Arun, Tamor, and Sun Kosi rivers (0.75 ± 0.06 mm yr^{-1} at ARU-11-26) northward to the border with Tibet (0.24 ± 0.02 mm yr^{-1}, n=4) (Figure 3.6a, Table 3.2). Near their confluence with the Arun, the Sun Kosi and Tamor have denudation rates of 0.82 ± 0.06 mm yr^{-1} and 1.39 ± 0.11 mm yr^{-1}, respectively. The Sapt Kosi, measured in the alluvial plain, records a denudation rate of 0.91 ± 0.07 mm yr^{-1}. This marks a five-fold decrease in mainstem denudation rates across the Arun/Sapt Kosi River from the alluvial plain to Tibet. Similarly, the relatively high denudation rates in the Sun Kosi and Tamor rivers that drain the southern flanks of the Himalaya are 5 to 7 times greater than in the upper reaches of the Arun.

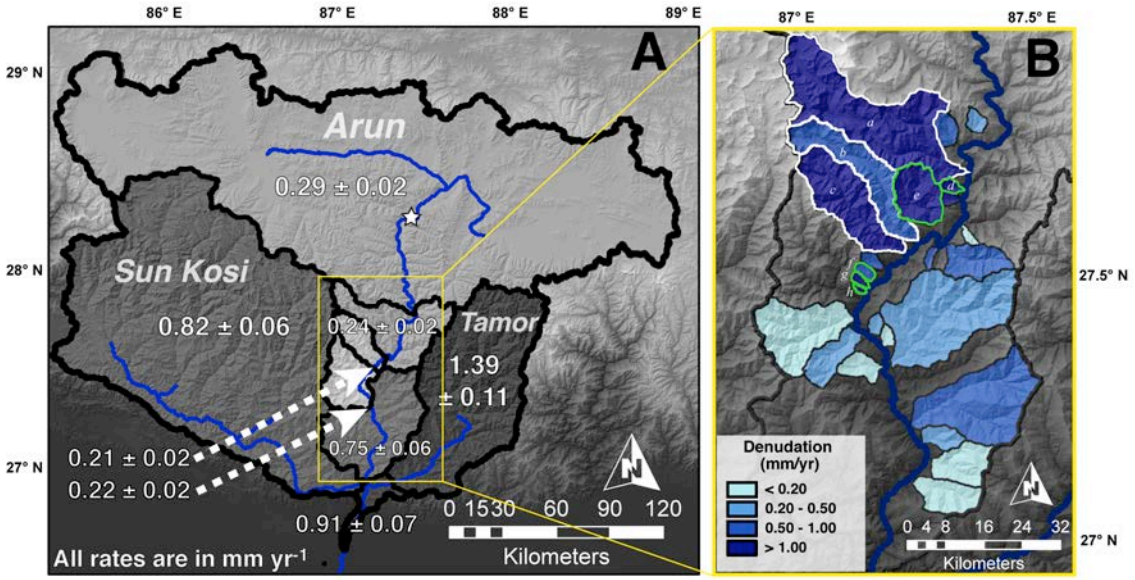

Figure 3.6 Catchment-mean denudation rates

TCN catchment-mean denudation rates for: (A) the mainstem Arun, Sun Kosi, Tamor, and Sapt Kosi, showing northward decrease in apparent denudation rate; and (B) sampled tributaries to the Arun, showing northward increase in the Himalaya. Denudation rates are shown alongside the river network (blue), elevation (hillshade), and the major knickzones in the mainstem Arun (star). All denudation rates are shown in mm yr^{-1}. Glaciated tributaries are outlined in white ((a) ARU-12-11, (b) ARU-11-15, (c) ARU-11-14). Landslide-impacted tributaries outlined in green ((d) ARU-12-09, (e) ARU-12-19A, (f) ARU-11-11, (g) BBRS01, (h) ARU-11-10).

Table 3.2 Sample ^{10}Be results and denudation rates

	Sample ID	Quartz Mass (g) [a]	Muonic Production-tion Rate (atoms / (g yr)) [b]	Mean Spallio-genic Production Rate (atoms/ (g yr)) [b]	Topo-graphic Shielding [c]	Ice Shielding [d]	10Be conc. (atoms/ g) [e]	±10Be (atoms/ g)	Basin-Average Denudation (mm/yr) [f]	Apparent Age (yr) [g]	Used in Regression Analysis?
Arun, Sun Kosi, Tamor	ARU-11-01	149.37	0.74	65.16	0.999	0.943	1.78E+05	3.18E+03	0.22 ± 0.02	2.74E+03	NO [h]
	ARU-11-13	72.41	0.75	67.12	0.999	0.941	1.95E+05	3.34E+03	0.21 ± 0.02	2.92E+03	NO [h]
	ARU-11-16	69.87	0.76	67.89	0.999	0.940	1.71E+05	2.88E+03	0.24 ± 0.02	2.53E+03	NO [h]
	ARU-11-25	124.71	0.48	26.39	0.997	0.849	1.18E+04	4.44E+02	1.39 ± 0.11	445.4164	NO [h]
	ARU-11-26	125.70	0.71	62.83	0.999	0.946	4.84E+04	9.88E+02	0.75 ± 0.06	7.79E+02	NO [h]
	ARU-11-27	88.55	0.50	30.34	0.997	0.930	2.29E+04	5.17E+02	0.82 ± 0.06	745.5625	NO [h]
	ARU-11-28	153.06	0.62	48.59	0.998	0.938	3.13E+04	8.22E+02	0.91 ± 0.07	6.48E+02	NO [h]
	ARU-12-03	102.78	0.76	67.65	0.999	0.940	2.85E+04	6.97E+02	1..35 ± 0.11	4.22E+02	NO [h]
	ARU-12-15	152.31	0.77	69.32	0.999	0.943	1.41E+05	2.73E+03	0.29 ± 0.02	2.04E+03	NO [h]
Lesser Himalaya	ARU-11-03	170.66	0.31	12.55	0.964	1.000	1.94E+04	2.60E+02	0.47 ± 0.03	1.50E+03	YES
	ARU-11-04	108.20	0.24	6.46	0.993	1.000	2.99E+04	7.18E+02	0.19 ± 0.01	4.48E+03	YES
	ARU-11-05	173.45	0.24	6.97	0.987	1.000	2.67E+04	4.17E+02	0.22 ± 0.01	3.72E+03	YES
	ARU-11-06	216.55	0.31	12.44	0.983	1.000	2.10E+04	6.16E+02	0.43 ± 0.03	1.66E+03	YES
	ARU-11-07	99.87	0.35	15.77	0.970	1.000	5.75E+04	1.03E+03	0.19 ± 0.01	3.60E+03	YES
	ARU-11-18	96.92	0.26	7.76	0.984	1.000	3.66E+04	5.08E+02	0.18 ± 0.01	4.59E+03	YES
	ARU-11-20	46.62	0.33	13.54	0.985	1.000	1.80E+04	1.49E+02	0.54 ± 0.04	1.31E+03	YES
	ARU-11-22	85.74	0.27	8.89	0.981	1.000	1.66E+04	1.56E+02	0.42 ± 0.03	1.82E+03	YES
	ARU-11-23	138.93	0.30	11.56	0.935	1.000	4.88E+04	8.43E+02	0.18 ± 0.01	4.15E+03	YES
	ARU-11-24	226.03	0.28	9.60	0.982	1.000	3.88E+04	7.64E+02	0.19 ± 0.01	3.95E+03	YES
Topographic Transition Zone	ARU-11-10	122.01	0.27	8.67	0.938	1.000	5.61E+03	7.27E+01	1.21 ± 0.08	6.32E+02	NO [i]
	ARU-11-11	110.40	0.30	11.17	0.971	1.000	8.24E+03	5.67E+01	1.00 ± 0.06	7.24E+02	NO [i]
	ARU-11-12	103.54	0.33	13.13	0.835	1.000	1.21E+04	3.58E+02	0.78 ± 0.06	9.05E+02	YES
	ARU-12-01	202.79	0.31	11.99	0.981	1.000	1.71E+04	5.74E+02	0.51 ± 0.04	1.40E+03	YES
	ARU-12-02	200.02	0.40	20.79	0.958	1.000	2.59E+04	3.81E+02	0.53 ± 0.04	1.24E+03	YES
	ARU-12-06	206.34	0.39	19.68	0.974	1.000	9.12E+04	1.59E+03	0.15 ± 0.01	4.59E+03	NO [k]
	BBRS01	104.18	0.2861	9.94	0.980	1.000	1.61E+03	2.50E+01	4.58 ± 0.30	1.58E+02	NO [i]
	ARU-11-14 I	107.16	0.55	37.45	0.921	0.944	1.65E+04	2.09E+02	1.36 ± 0.10	4.39E+02	NO [j]
	ARU-11-15 I	163.54	0.64	31.30	0.925	0.710	2.07E+04	2.83E+02	0.94 ± 0.07	6.57E+02	NO [j]
Higher Himalaya	ARU-12-08	166.05	0.37	16.83	0.960	1.000	7.85E+03	2.99E+01	1.44 ± 0.10	4.61E+02	YES
	ARU-12-09	149.74	0.37	17.19	0.955	1.000	4.97E+03	2.95E+02	2.30 ± 0.21	2.86E+02	NO [i]
	ARU-12-11	142.05	0.75	36.29	0.951	0.688	1.48E+04	2.92E+02	1.48 ± 0.11	4.05E+02	NO [j]
	ARU-12-12	215.14	0.45	27.26	0.865	1.000	2.47E+04	1.30E+03	0.68 ± 0.06	9.32E+02	YES
	ARU-12-13	190.31	0.47	28.99	0.725	1.000	3.87E+04	1.18E+03	0.47 ± 0.04	1.33E+03	YES
	ARU-12-19A I	138.89	0.4164	22.43	0.971	1.000	1.36E+03	2.72E+01	10.36 ± 0.76	6.01E+01	NO [i]

a - Mass of quartz dissolved for 10Be extraction.
b - Production rate calculations were performed for every gridpoint of the 90-m DEM using the Lal/Stone scaling scheme [Lal, 1991; Stone, 2000]. Production rate depends on altitude, latitude, and topographic and ice shielding.
c - Topographic shielding based on 90-m SRTM DEM following Dunne et al. [1999].
d - Ice shielding is based on present ice coverage from the National Snow & Ice Data Center (NSIDC) Global Land Ice Measurements from Space (GLIMS) database.
e - Derived from blank-corrected AMS measurements undertaken at Lawrence Livermore National Laboratory and normalized to ICN standard (Nishiizumi et al., 2007).
f - Denudation rates are calculated with a bedrock density of 2.6 g cm– 3 and an attenuation length for spallation of λ = 160 g cm2.

g - Time over which denudation rates are averaged (yr).
h - Mainstem sample, or other tributary that integrates entire topographic and climatic gradient.
i - Landslide-impacted tributary with apparent denudation rate that likely does not represent temporal average.
j - Glaciated tributary.
k - Small tributary (<10 km2) with pronounced transient profile.
l - Catchment lies within multiple physiographic regions, but has been grouped with dominant area.

3.4.3.2 Tributary catchments

The highly dynamic orogenic environment of the Himalaya includes several non-fluvial processes (e.g., landsliding, glaciation) that complicate the interpretation of TCN-derived denudation rates (e.g., *Brown et al.*, 1995; *Niemi et al.*, 2005; *Yanites et al.*, 2009; *Godard et al.*, 2012). To avoid these complications, we first present denudation rates from fluvial tributaries that do not show evidence of recent landsliding or glaciation, then describe results from glacial and landslide-impacted catchments. Fluvial tributaries show an order-of-magnitude northward increase in catchment-mean denudation rates from the Lesser to Higher Himalaya (Figure 3.6b, Table 3.2). Denudation rates in the LH are low to moderate (<0.5 mm yr^{-1}) and vary over a relatively narrow range (~0.2-0.5 mm yr^{-1}) (n=10). Denudation rates increase in the topographic transition zone (~0.5-0.8 mm yr^{-1}) (n=3) and are highest in the Higher Himalaya (1.44 mm yr^{-1} in ARU-12-08), then appear to decrease further into the orogen (e.g., 0.47 mm yr^{-1} in ARU-12-13) (n=3). Higher denudation rates in the topographic transition zone and the Higher Himalaya, however, may be mainly driven by glacial and hillslope processes.

Glaciers occupy some tributary valleys in the Higher Himalaya (Figure 3.6) and have the potential to alter TCN denudation rates. We observe high denudation rates in the heavily glaciated Barun Valley (ARU-12-11, 1.48 ± 0.11 mm yr^{-1}), as well as in two less glaciated valleys directly south of the Barun (ARU-11-14, 1.36 ± 0.10 mm yr^{-1}; ARU-11-15, 0.94 ± 0.07 mm yr^{-1}). However, there are fundamental problems interpreting denudation rates from these valleys: (1) shielding of bedrock from cosmogenic rays by glacial ice; (2) the assumption of steady-state erosion through time (*Bierman and Steig*, 1996); and (3) the assumption that each area in the basin contributes sediment in proportion to long-term erosion rates. The dynamics of glacial erosion and sediment delivery are complicated and poorly understood and are likely not steady through time. All of these processes may result in an overestimation of true denudation rates (*Godard et al.*, 2012; *Glotzbach et al.*, 2013). The application of an ice shielding grid to the

denudation rate calculation accounts for glacial shielding of sediment in the detrital sample, thus producing more reliable denudation rate estimates. However, we note that we cannot account for possible non-steady state or proportionate denudation through time, and therefore consider denudation rates from glacial catchments as apparent denudation rates that may differ from temporal-averages.

Landsliding is common throughout the steep-slope terrain of the Himalaya (e.g., *Bookhagen et al.*, 2005b; *Dahal and Hasegawa*, 2008). Because landslides frequently erode material from below the absorption depth of cosmogenic nuclides, they have the potential to dilute the ^{10}Be signal within a detrital sample. If the catchment is sufficiently large and well-mixed, TCN concentrations from landslide-dominated catchments can still provide reliable denudation rates (*Niemi et al.*, 2005; *Yanites et al.*, 2009). However, small, poorly-mixed catchments or samples collected shortly after recent landslide events may result in calculated denudation rates that do not reflect the time-averaged denudation rate (*Yanites et al.*, 2009). To quantify the potential impact of landsliding on our samples, we mapped visible landslide scars in all sampled tributary catchments using high-resolution imagery from Google Earth (see data repository Figure S3.1 for further information) (*Fisher et al.*, 2012). While small landslides are ubiquitous in the study area, we observed five catchments with a pronounced amount of landsliding as a percentage of total catchment area: three small catchments (<10 km^2) in the topographic transition zone (ARU-11-10, ARU-11-11, BBRS01); and one small catchment (~10 km^2) and one medium-sized catchment (~100 km^2) in the Higher Himalaya (ARU-12-09, ARU-12-19A respectively). In each catchment, the landslide area is markedly higher than the 0.001% of total catchment area proposed by Yanites et al. (2009) that will still produce a reliable denudation rate. BBRS01, ARU-12-09, and ARU-12-19A have anomalously high apparent denudation rates (4-10 mm yr^{-1}) and the five landslide-affected tributaries represent the lowest observed ^{10}Be concentrations in our study area. Due to the likely recent delivery of material from below the ^{10}Be absorption depth from landslides in these samples, measured ^{10}Be concentrations may not be representative of the temporal average. We therefore consider the calculated denudation rates as maximum apparent denudation rates.

A more complex picture of denudation across the Arun Valley emerges when we consider the entire set of denudation rates, incorporating glacial and

landslide-impacted apparent denudation rates. We observe largely fluvial denudation through the Lesser Himalaya, with low to moderate rates that do not vary considerably (0.2-0.5 mm yr^{-1}). In the topographic transition zone, fluvial denudation rates increase (0.5-0.8 mm yr^{-1}) concurrent with an increase in landsliding, with apparent denudation rates of ~5 mm yr^{-1}. This marks the changeover to an erosion regime that is more variable in both rates and processes. Significant landsliding continues at the front of the Higher Himalaya (ARU-12-09, ARU-12-19A) with maximum denudation rates in excess of 10 mm yr^{-1}. Glaciation additionally begins to play a role in the Higher Himalaya, maintaining denudation rates similar to the highest fluvial denudation rates (~0.9-1.5 mm yr^{-1}). Fluvial denudation rates, meanwhile, appear to decrease into the Higher Himalaya away from the high-relief, high-rainfall frontal zone (e.g., ARU-12-13).

3.5 Discussion

^{10}Be TCN samples from the Arun Valley record a pronounced northward increase in denudation rates across the Himalaya in tributary catchments, and a four-fold decrease in mainstem denudation rates from the lower reaches of the Arun to the upper reaches bordering Tibet. In a dynamic environment such as the Himalaya, several factors can influence ^{10}Be concentrations (e.g., non-uniform sediment-sourcing, transient sediment storage) (*Bierman and Steig*, 1996; *Granger et al.*, 1996; *von Blanckenburg*, 2005). However, we did not find evidence of major impacts from potentially variable sediment-sourcing or transiently stored sediments on our measured ^{10}Be concentrations and calculated denudation rates (see supporting material S1 for details of the analyses performed). Below, we further discuss the interpretation of ^{10}Be concentrations and denudation rate calculation.

3.5.1 Downstream evolution of mainstem ^{10}Be concentration

In order to better understand the impact of regional factors on denudation rates, we first consider measured ^{10}Be concentrations directly (Table 3.2, Figure 3.5). For the following discussion, we interpret the two distinct groupings of ^{10}Be concentrations discussed in 4.2 as: (1) the Tibetan signal, comprising high ^{10}Be concentrations measured in the upper reaches of the mainstem Arun; and (2) the Himalayan signal, comprising low ^{10}Be concentrations measured in tributaries to

the Arun, the Sun Kosi and Tamor, and from the downstream sections of the mainstem Arun.

3.5.1.1 Downstream fining

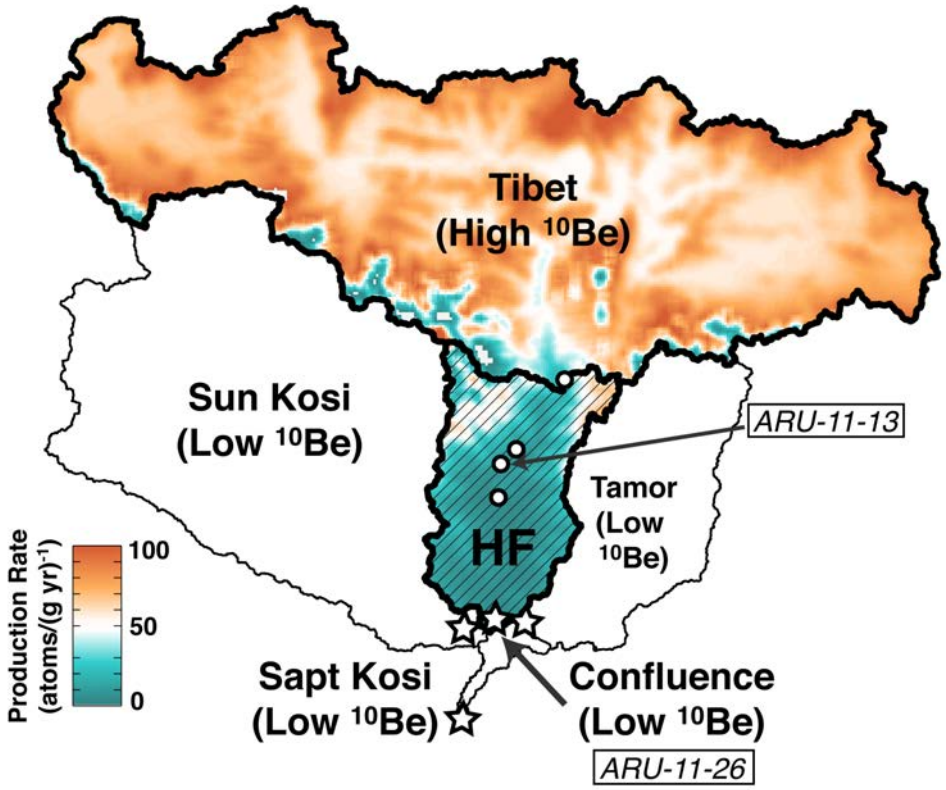

Figure 3.7 Production rates and mass balance

Schematic of mainstem ^{10}Be concentration mass balance calculations on map showing ^{10}Be production rates. Observed ^{10}Be concentrations at mainstem Arun, and other major river sand sample locations are shown as circles (high observed ^{10}Be, ~10^5 atoms g^{-1}) or stars (low observed ^{10}Be, ~10^4 atoms g^{-1}). The Tibet, Himalaya (H), and confluence locations used in the mass balance calculation are highlighted; Himalayan section of the catchment shown in hatch. Higher ^{10}Be production rates (at/(g yr)) in Tibet compared to the Himalaya results in a distinct signal that allows for the detection of downstream fining from Tibet to the confluence of the Sapt Kosi.

One of the most prominent features of the ^{10}Be concentrations is the pronounced downstream reduction of ^{10}Be in the mainstem Arun (Figure 3.5). This order-of-magnitude difference must be the result of either: (1) a large sediment flux from the Himalaya able to sufficiently dilute the ^{10}Be signal from Tibet to the levels recorded at the Sapt Kosi confluence; or (2) significant sediment storage within the Himalayan section of the valley. Comparing the ^{10}Be concentration in ARU-11-13 (high ^{10}Be) and ARU-11-26 (low ^{10}Be), we solve the mass-balance problem presented in Equation 3.2 as:

$$Conc._{\mathrm{ARU-11-26}} = \frac{Area_{\mathrm{ARU-11-13}} MF_{\mathrm{ARU-11-13}} Conc._{\mathrm{ARU-11-13}} + Area_H MF_H Conc._H}{Area_{\mathrm{ARU-11-26}} MF_{\mathrm{ARU-11-26}}} \quad (3.3)$$

where H denotes the Himalaya between Tibet and the Sapt Kosi confluence and MF represents the mass flux (g cm^{-2} yr^{-1}) (Table 3.1, 3.2; Figure 3.7). To solve for mass flux, we assume that the mean ^{10}Be concentration from Arun tributaries (2.56 x 10^4 ± 4.6 x 10^2 at g^{-1}, n=20) is representative of the ^{10}Be concentration of the entire Himalayan section of the valley. However, using this ^{10}Be concentration, the resulting mass flux for the southern flanks of the Himalaya is negative (-0.12 g cm^{-2} yr^{-1}), indicating sediment storage in a region where no significant modern sediment storage is observed (see supporting material S1). As such, it is impossible to reconcile the ^{10}Be concentration measured at ARU-11-26 with a positive mass flux from the Himalaya under these assumptions. Similarly, if we define the Himalayan mass flux as MF_H=MF_{26} - MF_{13} (0.15 g cm^{-2} yr^{-1}), the calculated ^{10}Be concentration is likewise negative, a physical impossibility unless the system is undergoing either sedimentation or sediment loss through grain fining. We therefore assume that the collected sample cannot be a uniform representation of the upstream area. Instead, we suggest that downstream sediment fining continues for particles <2 mm, resulting in the Tibetan sediment passing through our 250-750 μm sample sieve. This effect is identifiable in the Arun due to the large difference in ^{10}Be production rate between the high-altitude, low-relief Tibetan region (high ^{10}Be production) and the relatively low-altitude, high-relief Himalaya (low ^{10}Be production, Figure 3.7). However, similar problems could remain undetected in sufficiently large watersheds with uniform or near-uniform ^{10}Be production rates, such as the Sun Kosi or Tamor or large watersheds in other orogens.

The exclusion of upstream sediment grains from the analyzed samples results in estimated denudation rates that do not reflect the entire upstream area. We therefore interpret the calculated "high" denudation rates from the mainstem Arun (e.g., ARU-11-26, 0.75 mm yr^{-1}) as primarily reflecting the denudation rate of the southern flanks of the Himalaya and not the Tibetan section of the watershed, resulting in an overestimation of the true denudation rate for the watershed. This finding calls into question the use of large watersheds or distal sampling sites to characterize regional denudation rates, particularly in the Himalaya and in trans-Himalayan rivers. Recent studies have highlighted

differences in ^{10}Be concentrations in different grain size fractions from detrital sand samples (*McPhillips et al.*, 2014; *Puchol et al.*, 2014). While the motivation for these analyses has been primarily to quantify the impact of landslide processes and focus on larger grain and cobble sizes, measuring ^{10}Be concentration from various grain size fractions, including those <200 μm, may also mitigate the problems downstream fining poses for denudation rate estimation.

3.5.1.2 Climate-driven dilution of ^{10}Be concentration

The northernmost mainstem sample, ARU-12-15, has a noticeably lower ^{10}Be concentration than nearby samples from the northern mainstem Arun, resulting in a local southward increase in ^{10}Be concentration before the more drastic decrease near the topographic transition zone. This southward increase of ^{10}Be is restricted to the glaciated portion of the Higher Himalaya (Figure 3.5). Glaciated catchments measure amongst the lowest ^{10}Be concentrations in the Arun Valley. North of our study area, extensive glaciation exists on the northern flank of the HH. Specifically, a large and heavily glaciated tributary that drains the northern slopes of the Sagarmatha/Everest massif joins the Arun approximately 10 km north of the sampling point of ARU-12-15. This nearby influx of highly shielded sediment may locally dilute the ^{10}Be concentration measured at ARU-12-15 before it is measured again over 40 km downstream. A modeled ^{10}Be concentration for ARU-12-15 assuming an erosion rate of 0.2 mm yr^{-1} (approximate denudation rate from nearby mainstem samples ARU-11-01, -13, -16; Figure 3.6, Table 3.2) and the mean upstream production rate is nearly 1.5 times the measured value (2.09×10^5 at g^{-1} modeled as opposed to 1.41×10^5 at g^{-1} measured in ARU-12-15), suggesting a large, local influx of low ^{10}Be sediment is responsible for the ^{10}Be concentration measured at ARU-12-15. We also observe a relatively low ^{10}Be concentration (and therefore higher apparent denudation rate) in the Tamor compared to the mainstem Arun or the Sun Kosi. Glaciers occupy a larger area of the Tamor basin (~15%) compared to these other large rivers (~5-7%) and the higher degree of glaciation in the Tamor may be the cause of lower ^{10}Be concentrations and higher apparent denudation rates.

In addition to local dilution from glacial input, we observe one mainstem sample in the northern section of the study area (ARU-12-03) with a low ^{10}Be ratio

where we would expect to measure a high ^{10}Be signal from Tibet. This sample was taken less than 2 km downstream of a medium-sized tributary with large, recent landslides (ARU-12-19A) that are likely to have diluted the ^{10}Be concentration of the mainstem sample (ARU-12-19A has the lowest measured ^{10}Be concentration in our dataset). Landsliding predates the 2012 field season when samples ARU-12-03 and ARU-12-19A were collected. The timing of the large landslides in ARU-12-19A is not easily constrained with high-resolution imagery due to high cloud cover and poor image resolution, but some landslide scars are visible as early as 2009. A nearby sample collected in 2011 (ARU-11-16) does not show the low ^{10}Be concentration derived from the landslide. This may be due to the timing of the landslides or to different sediment sourcing in the river system during and after the monsoon season (e.g., *Lupker et al.*, 2012).

It is notable that landslide-impacted tributaries are focused at the front of the Higher Himalaya where elevation, rainfall, and relief rapidly increase from the Lesser Himalaya. While relief and elevation remain high throughout the Higher Himalaya, rainfall decreases northward toward the high topography. Landslide-impacted tributaries are focused in a zone where both relief and rainfall peak, showing the importance of focused rainfall in triggering mass movements (Figure 3.5).

3.5.2 Denudation gradient across the Arun Valley

In general, denudation rates in tributaries to the Arun increase from south to north coincident with the increase of topographic metrics such as hillslope angle, k_{sn}, and local relief (Figure 3.3, Table 3.3). Due to the tectonic window, nearly all sampled basins are composed of both LHC and HHC units and no major lithologic boundaries are crossed by the mainstem Arun in our study area (Figure 3.1d). Although the percentage of HHC rocks increases northward as the Arun Tectonic Window narrows and denudation rates increase, no relationship is observed between catchment-mean denudation rates and lithology (see Figure S3.2).

The across-strike pattern of northward increasing denudation rates we observe is similar to those reported by Godard et al. (2014) and Scherler et al. (2014). In both studies, denudation rates in the Lesser Himalaya are reported

between ~0.1-0.5 mm yr^{-1} and increase rapidly at the transition to the Higher Himalaya, where denudation rates exceed 1 mm yr^{-1}. The similar pattern between the Arun Valley and the results of studies where denudation rates are fit to tectonic drivers suggests that, at first order, a similar process drives the rates and pattern of denudation in the Arun Valley. We note, however, that the highest rates of denudation (>2 mm yr^{-1}) reported by Godard et al. (2014) and Scherler et al. (2014) are derived form regions with high rainfall rates and high local relief, similar to where we found the highest incidence of landslide-impacted catchments in the Arun, and may be overestimations of true denudation rate.

Figure 3.8 Power law relationship of denudation rates and k_{sn}.

Power-law relationship of the standard area-weighted k_{sn} (θ=0.45, R^2=0.54) and denudation rates, shown with 95% confidence interval in shaded gray compared to published relationships from Bookhagen and Strecker (2012a), Ouimet et al. (2009); Safran et al. (2005), and Scherler et al. (2014). The observed power law exponent b (from the relationship $y=ax^b$) for the Arun is b=1.96 (95% confidence interval, upper and lower bounds b=0.33, 1.19).

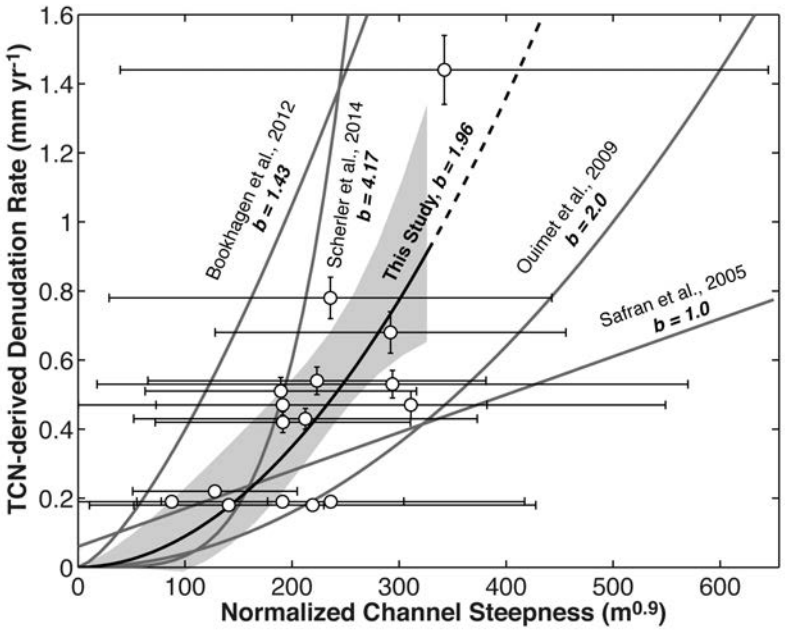

Previous studies have suggested a nonlinear relationship between topographic metrics (e.g., slope, k_{sn}) and denudation rates, such that for a given topographic metric, $(topographic\ metric)^b \sim denudation\ rate$, with power-law values ranging from b=1 to b=4 (*Safran et al.*, 2005; *Ouimet et al.*, 2009; *DiBiase et al.*, 2010; *DiBiase and Whipple*, 2011; *Bookhagen and Strecker*, 2012a; *Fisher et al.*, 2013; *Scherler et al.*, 2014). We observe the highest correlation between denudation rate and χ-determined k_{sn} (R^2=0.66 for area-weighted k_{sn}, R^2=0.67 for TRMM-weighted k_{sn}, compared to R^2=0.54, 0.57 for area- and TRMM-weighted

for the standard k_{sn} normalized by θ=0.45). The power-law relationship between k_{sn} and denudation rate in our dataset ranges from b=1.33-1.96, similar to studies in other active tectonic environments (Figure 3.8 and references therein). Fluvial incision models (e.g., *Whipple and Tucker*, 1999; *Snyder et al.*, 2003a; *Sklar and Dietrich*, 2004; *Lague et al.*, 2005) predict a monotonic relationship between channel slope and rock uplift at steady-state, and numerous studies have shown positive correlations between k_{sn} and rock uplift (e.g., *Snyder et al.*, 2000; *Kirby and Whipple*, 2001; *DiBiase et al.*, 2010). The large knickpoints in the mainstem Arun upstream of our study area (Figure 3.2) and several perched low-relief surfaces (see section 5.3 below), however, cast doubt on the assumption that the Arun is in landscape equilibrium. Localized high k_{sn} values have also been shown to correlate with areas where the river is adjusting to a transient perturbation. When this is the case, high k_{sn} values will follow knickzones as they propagate through the channel network as it adjusts to the perturbation (e.g., base-level drop, change in uplift rates) (e.g., *Wobus et al.*, 2006). Such a perturbation can be climatic or tectonic, however several studies along strike have found evidence for relatively high uplift rates in the Higher Himalaya with respect to the Lesser Himalaya (e.g., *Lavé and Avouac*, 2001; *Godard et al.*, 2004; *Herman et al.*, 2010; *Coutand et al.*, 2014). We therefore associate high k_{sn} and corresponding high denudation rates with locally high uplift rates.

Table 3.3 OLS regression results

	All fluvial tributaries					***Excluding landslide-affected tributaries***				
Metric	***R^2***	***F-value***	***p-value***	***a***	***b***	***R^2***	***F-value***	***p-value***	***a***	***b***
				$y=ax^b$					*$y=ax^b$*	
Topographic Metrics										
Hillslope Gradient	0.19	5.80	0.0277	1.32E+00	1.35E+00	0.35	13.01	0.0029	1.49E+00	1.67E+00
1-km Relief	0.23	6.48	0.0209	1.47E-05	1.57E+00	0.37	11.81	0.0040	2.35E-06	1.84E+00
Area SSP	0.26	2.81	0.1121	3.56E-02	5.10E-01	0.26	2.98	0.1062	3.56E-02	5.10E-01
Area k_{sn} (θ=0.45)	0.18	3.79	0.0682	1.26E-03	1.11E+00	0.54	11.33	0.0046	1.08E-05	1.96E+00
Area k_{sn} (θ=0.23)	0.26	5.47	0.0318	5.72E-02	1.14E+00	0.66	16.59	0.0011	1.14E-02	1.90E+00
Climatic Metrics										
TRMM	0.04	1.19	0.2910	3.73E-01	3.43E-01	0.23	6.40	0.0241	1.90E-01	9.22E-01
TRMM SSP	0.35	4.99	0.0392	1.06E-02	6.93E-01	0.35	7.10	0.0185	1.06E-02	6.93E-01
TRMM k_{sn} (θ=0.45)	0.15	3.30	0.0872	1.26E-02	6.44E-01	0.57	14.83	0.0018	2.04E-04	1.33E+00
TRMM k_{sn} (θ=0.20)	0.23	5.04	0.0384	1.30E-01	8.52E-01	0.67	19.14	0.0006	3.44E-02	1.59E+00

Although we observe a moderately strong correlation between denudation rates and k_{sn}, our denudation rates correlate poorly with many other standard topographic and climatic metrics (Table 3.3). We were not able to constrain several factors of the fluvial network, such as channel width, depth, and geometry. Recent studies have highlighted the importance of channel width and geometry in the stream-power model and in erosional proxies, such as specific stream power (*Fisher et al.*, 2013). In our SSP calculations, we scaled channel width to discharge following a power-law relationship (*Knighton*, 1999; *Whipple*, 2004; *Craddock et al.*, 2007). This approach results in channel width increasing nonlinearly as upstream area increases. However, the low concavity values we derived from χ-analysis of the fluvial network indicate that many channels in the Arun continue to have steep channels gradients in their lower reaches, and thus narrow channel widths (*Yanites et al.*, 2010b; *Fisher et al.*, 2012). Discharge scaling is therefore likely an inaccurate estimate of channel width in this environment, and may explain why SSP poorly describes denudation rates in the Arun compared to other orogens (e.g., *Bookhagen and Strecker*, 2012a). Similar scaling issues may exist in other regions with steep channels and low concavity.

3.5.3 Percentile regression of catchment characteristics and denudation rates

In dynamic landscapes, topography and topographic metrics within a catchment may not always follow a normal or Gaussian distribution. Such skewed or multi-modal catchment distributions can result in mean or median values that are not the best representatives of the data population. Lilliefors tests suggested a non-normal distribution of elevation, hillslope gradient, 1-km local relief, and mean annual rainfall in all sampled catchments at a 95% confidence level. On the other hand, k_{sn} values do not show evidence of non-normal distributions in some basins; however, this result may be an artifact of sample size, as a smaller sample is less likely to reject the null hypothesis of normal distribution. Similarly, we found a systematic positive skew (right-tail) in the distribution of hillslope gradient and k_{sn} (see Table S3.2).

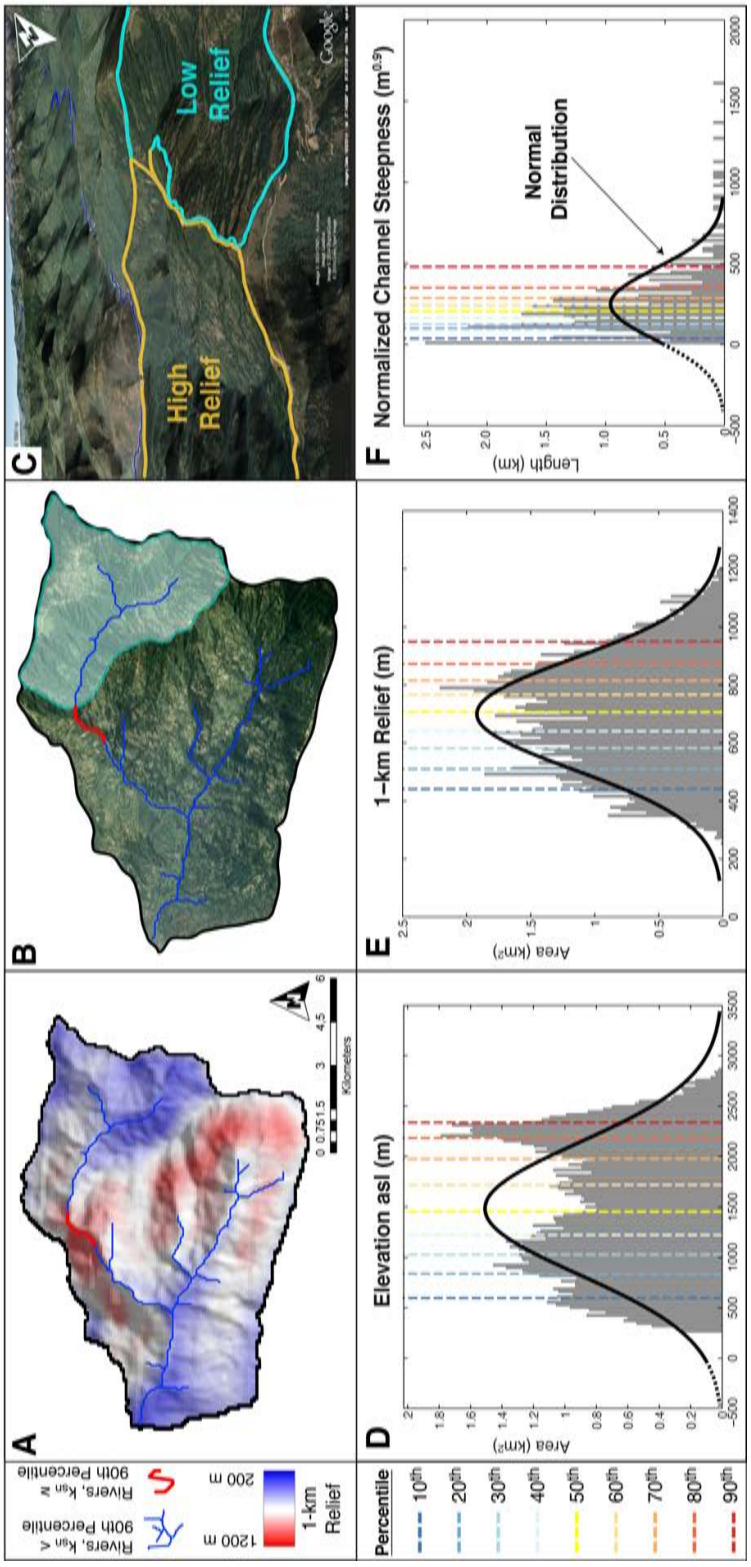

Figure 3.9 Example of non-normal topographic distribution.

Example catchment demonstrating non-normal topographic distribution (ARU-11-23). (A) 1-km relief map of the catchment, paired with 90th percentile of k_{sn} located at the foot of the transient surface. (B) Our interpretation of the relief map, with perched, low-relief surface shown in blue. (C) Google Earth view of low-relief topography. (D-F) Histograms of topographic metrics: (D) elevation (m asl), (E) 1-km relief (m), (F) k_{sn} ($m^{0.46}$), shown with approximate normal distribution (black line) and percentile values (dashed lines).

Figure 3.9 shows an example of how such non-normal distributions may arise within a catchment as the result of transient topography. Relatively small areas of perched, low-relief topography were observed throughout the study area. Here, a low-relief area in the upper reaches of the catchment (Figure 3.9c) results in a bimodal distribution of elevation, and quasi-bimodal distribution of 1-km local relief (Figure 3.9d,e). High k_{sn} is focused at the foot of the perched low-relief area where knickpoints propagate into relict topographies and the catchment moves towards equilibrium. As shown in the histograms of elevation, local relief, and k_{sn}, the normal distribution and associated statistics (mean, standard deviation) assumed by averaging do not fit the data population. While catchments with transient features are likely to be the most problematic in this regard, evidence for skewed and non-normal distributions were found in all catchments for nearly all metrics.

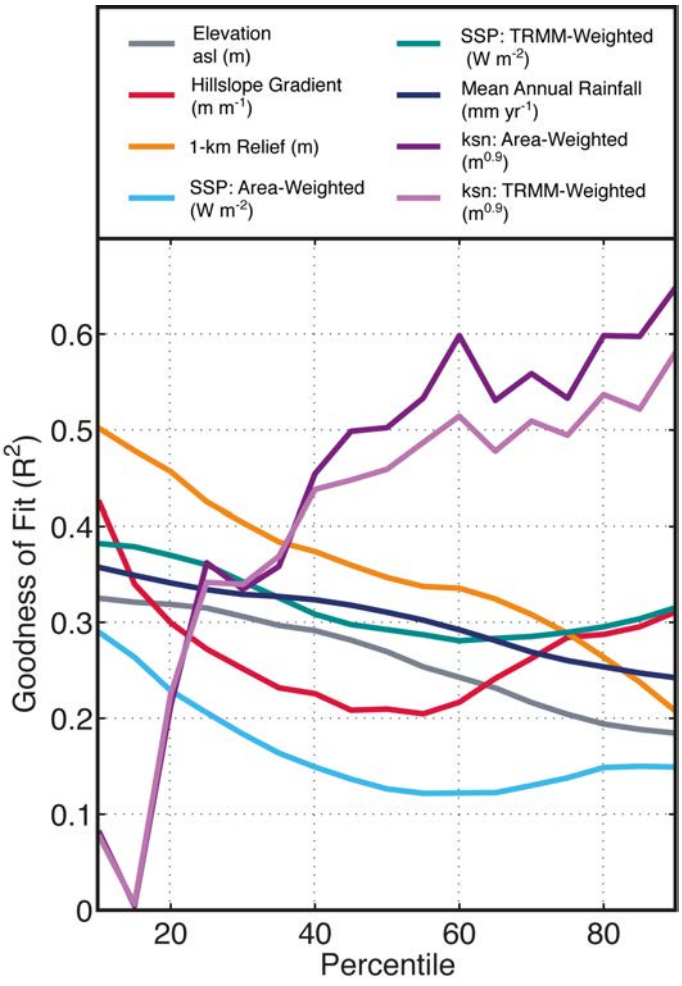

Figure 3.10 Percentile regression results.

Regression results between various catchment-mean topographic and climatic metrics and denudation rates based on percentiles of catchment metrics and denudation rates, showing the variable goodness-of-fit depending on which catchment value is used. Normalized channel steepness values calculated using channel concavity from χ-analysis, showing the moderately strong correlation between k_{sn} and denudation rates.

Figure 3.10 shows the goodness of fit (R^2) of the regression analysis using the catchment-mean value and the catchment percentile values of various topographic and climatic metrics. The strength of the correlation between denudation rate and catchment topography and climate varies by as much as a factor of six (e.g., k_{sn}) depending on the metric and the percentile used. In the case of k_{sn}, the correlation increases positively with the percentile used. However, the systematic positive skew in the distribution of k_{sn} values in sampled catchments suggests that channel segments where $k_{sn} > 90^{th}$ percentile comprise relatively small portion of the channel network. Thus, the rate of denudation may be most sensitive to, and focused at, locations in the catchment that do not correspond with standard averaging techniques (e.g., mean, median, or mode). The disconnect between catchment average statistics, the catchment distribution of topographic metrics, and the areas (sometimes small) that correlate best with denudation rates highlights the problem of uniformly characterizing catchments in a highly dynamic landscape. While such topographic metrics are useful first-order approximations, they are far from exact proxies for the processes that drive erosion.

3.6 Conclusions

Based on our 34 new ^{10}Be TCN measurements in eastern Nepal combined with field observations and topographic and climatic analyses, we reach the following conclusions:

Catchment-mean denudation rates show an order-of-magnitude northward increase from the Lesser Himalaya to the Higher Himalaya, as elevation, hillslope, and channel steepness increase. The spatial pattern of denudation rates is most strongly correlated with normalized channel steepness, following a non-linear power-law relationship $(k_{sn})^b \sim$ *denudation rate* with best-fit parameter for b=1.89 (θ=0.23, $R^{2=}$0.66, 95% confidence interval b_{lower}=1.01, b_{upper}=2.27). The strong relationship between denudation rates and k_{sn}, as well as a similar observed pattern of denudation rates derived from studies arguing for tectonic drivers (*Godard et al.*, 2014; *Scherler et al.*, 2014), suggests a prominent role of rock uplift in forcing denudation rates in the Himalaya (cf. *Godard et al.*, 2014; *Scherler et al.*, 2014). However, we observe multiple climatic influences on the processes of erosion in

the Arun Valley, such as the extent of glaciation and localized landsliding in the area of peak rainfall and relief.

Non-fluvial processes such as extensive glaciation and landsliding upstream of sample sites can cause local dilution of ^{10}Be concentrations in detrital samples. Local dilution of detrital sand from the mainstem Arun demonstrates that such processes can even impact very large watersheds that are typically assumed to integrate upstream perturbations (e.g., landslides). When left unaccounted for, dilution of ^{10}Be concentration caused by local geomorphic processes could result in overestimation of catchment-mean denudation rates.

Downstream fining of fluvial sand continues past <2 mm diameter grains, resulting in sand grains sourced from upstream (Tibetan) sections of the watershed passing through the 250 μm sieve in samples collected downstream. Therefore, downstream mainstem Arun samples are likely representative of the Himalayan section of the catchment, rather than the entire watershed. Though the Arun provides a well-suited setting to record this effect, the exclusion of fined upstream sediment may also occur undetected in large watersheds in other mountain belts. We therefore call into question the use of distal detrital samples to characterize denudation rates in extensive mountainous catchments. Consequently, sampling multiple grain sizes in high-mountain environments may yield a more robust characterization of denudation rates, including potentially fined upstream sediments.

Non-normal distribution of catchment topographic and climatic parameters in many sampled basins in our study highlight the importance of using caution when choosing how to characterize catchments with regard to erosion processes. Skewed and multi-modal distributions of catchment topography and variations in sensitivity to denudation rates suggest that while such topographic metrics may be a useful first order approximation of the processes that drive erosion at the regional scale, they are far from ideal proxies at the catchment scale.

Acknowledgements

Data supporting Figure 3.10 are available in Table S3.3. This project was funded by the graduate school GRK1364 “Shaping Earth's Surface in a Variable Environment: **Interactions between tectonics, climate and biosphere in the African-Asian monsoonal region”** of the German Science Foundation (DFG,

Deutsche Forschungsgemeinschaft; Project GRK 1364/2). In addition, funding for one field season and all analytical work was provided by the HIMPAC research project (Himalayas: Modern and Past Climates), funded by DFG (STR 373/27-1 and 28-1) We thank Dirk Scherler and Taylor Schildgen for valuable discussions, Ed Sobel, Burch Fisher, and Jessica Thompson for help with laboratory work, and Bhim Chand of Earth's Paradise GeoTrekking for logistical support in the field. Finally, we thank Nicole Gasparini, Elizabeth Safran, and Ken Ferrier for their constructive input into greatly improving this manuscript.

Chapter 4: Role of climate and vegetation in modulating denudation rates in the Himalaya

Abstract

Vegetation cover has long been hypothesized to impact the form and rates of surface processes. We test the possible impact of vegetation and climate on denudation rates at orogen scale by taking advantage of a six-fold along-strike gradient in rainfall and vegetation density in the Himalaya. We combine 214 published ^{10}Be catchment-mean denudation rates from the Himalaya with remotely-sensed measures of vegetation density and rainfall metrics, tectonic and lithologic constraints. In addition, we perform topographic analyses to assess the contribution of vegetation and climate in modulating denudation rates along strike. We find that while denudation rates in the Higher Himalaya correlate with long-term tectonic exhumation rates, denudation and exhumation rates are decoupled along strike in the Lesser Himalaya. We observe variations in denudation rates and the relationship between denudation and topography that cannot be explained by tectonics or lithology alone, and instead appear to be controlled by variations in rainfall amount and vegetation density. The along-strike trend in denudation rate variability positively correlates with vegetation seasonality (R=0.99). Vegetation density modulates the topographic response to changing denudation rates, such that the functional relationship between denudation rate and topographic steepness becomes increasingly linear as vegetation density increases. We therefore suggest that while tectonic processes may dominate the pattern of denudation rates across strike of the Himalaya (i.e., S-N in the Himalaya), along strike of the orogen (i.e., E-W) climate exerts a measurable influence on denudation rates and on the relationship between topography and denudation.

4.1 Introduction

The role of vegetation in shaping landscapes and moderating denudation has been long recognized (e.g., *Langbein and Schumm*, 1958; *Douglas*, 1967; *Wilson*, 1973; *Rogers and Schumm*, 1991; *Tucker and Slingerland*, 1997; *Wolman and Gerson*, 1978), but our understanding of the impact of vegetation cover over

differing time and spatial scales remains incomplete (e.g., *Dietrich and Perron*, 2006; *Osterkamp et al.*, 2012). Langbein and Schumm (1958) posited that as effective precipitation increases, sediment yield will increase until there is sufficient precipitation to support a stable vegetation cover, causing subsequent decrease in sediment yield. Modeling studies have suggested that vegetation inhibits erosion and ultimately creates oversteepened landscapes, resulting in more variable and extreme erosion events (e.g., landsliding) (*Collins et al.*, 2004; *Istanbulluoglu et al.*, 2004; *Istanbulluoglu and Bras*, 2005). Several field studies have demonstrated that the absence of vegetation following wildfires or forest degradation can have a dramatic impact on erosion and sediment yield over short timescales (e.g., *Prosser and Soufi*, 1998; *Lamb et al.*, 2011; 2013; *Moody et al.*, 2013; *West et al.*, 2015). However, the general applicability of these findings has not been confirmed in large-scale field studies, or over longer timescales. While some large-scale studies have addressed this problem in recent years (*Carretier et al.*, 2013; *Torres Acosta et al.*, 2015), documenting how vegetation influences denudation rates in active orogens can prove difficult due to the strong interdependence of tectonics, topography, regional climate, and vegetation.

In the Himalaya, the present-day climate is strongly influenced by tectonically-created topography. Seasonal rainfall from the Indian Summer Monsoon (ISM) is focused at orographic barriers along the southern flank of the orogen (Figure 4.1a) (*Bookhagen and Burbank*, 2006), although this effect decreases toward the west. In general, vegetation density (Figure 4.1b) is highly influenced by available moisture and temperature, which is controlled primarily by geographic location and elevation. Thus, across strike of an orogen, peak rainfall and vegetation density correspond to orographic barriers and coincide with abrupt increases in topographic steepness. The resulting high interdependence of climate, vegetation, and topography complicates potential strike-perpendicular comparisons of these highly dynamic variables. However, samples for the determination of centennial to millennial denudation rates or million-year exhumation rates are mostly collected in transects perpendicular to strike of the most important structures and topographic relief (e.g., *Robert et al.*, 2009; *Bookhagen and Strecker*, 2012a; *Scherler et al.*, 2014; *Olen et al.*, 2015; *Portenga et al.*, 2015).

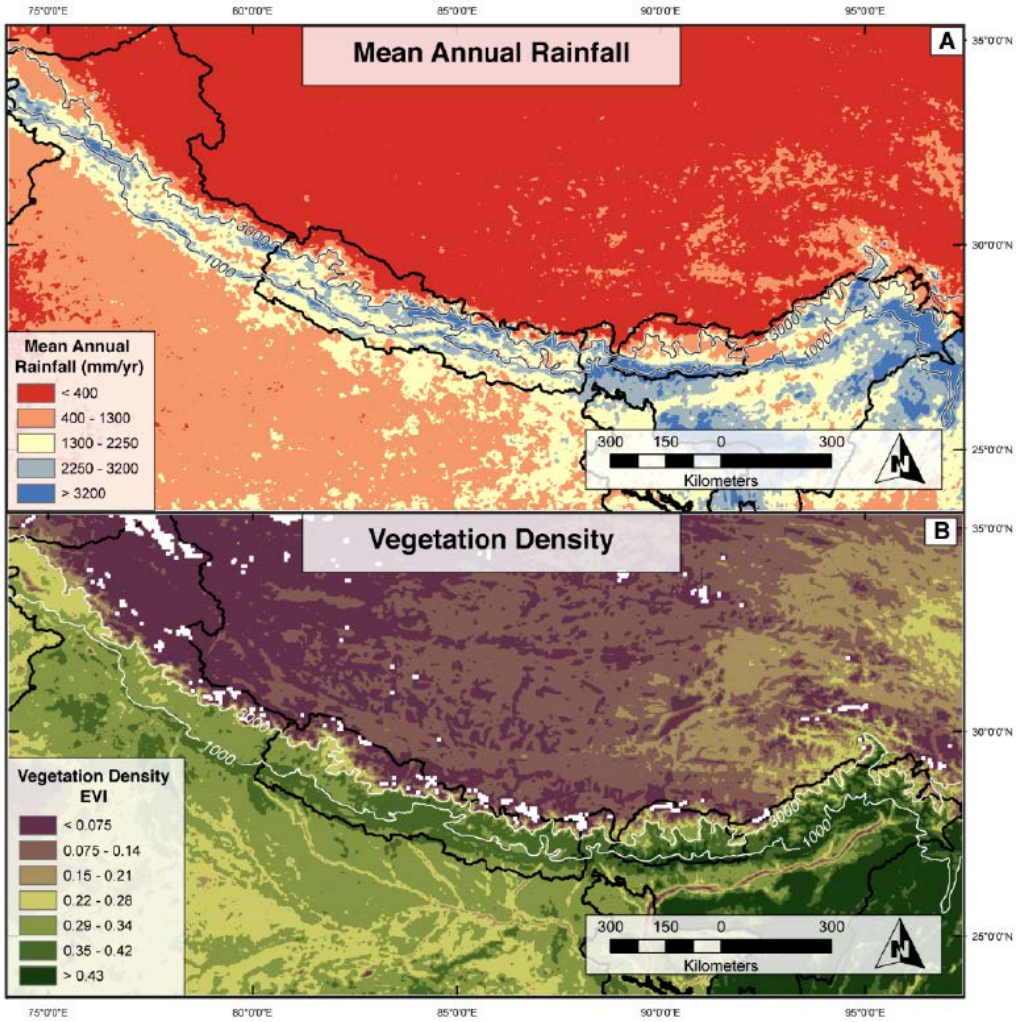

Figure 4.1 Rainfall and vegetation density of the Himalaya.

Regional distribution of mean annual rainfall (A) and vegetation density (B) of the Himalayan region. Mean annual rainfall (MAR) is from the Tropical Rainfall Measuring Mission (TRMM) calibrated 12-year average product 2B31 (*Bookhagen and Burbank*, 2010). Bands of high rainfall are focused along the orographic barriers of the Lesser and Higher Himalaya, corresponding approximately to the 1000 m asl and 3000 m asl contours shown in grey. Mean annual vegetation density is characterized by the Enhanced Vegetation Index (EVI), derived from MODIS multi-spectral satellite imagery (*Huete et al.*, 1994; *Justice et al.*, 1998) and averaged over 14 years. Low EVI values represent sparse or bare vegetation, while high values represent dense vegetation cover. 1000 m asl and 3000 m asl contours are shown for reference in white. White areas indicate no-data regions that are snow covered. Summer and winter EVI maps can be found in Figure S4.1. Black lines indicate political boundaries in both maps.

One way to minimize these complications is to consider a broader region characterized by an along-strike climatic gradient. In the Himalaya, mean annual rainfall (MAR) decreases as the moisture-bearing winds of the ISM travel westward from their primary moisture source in the Bay of Bengal (e.g., *Gadgil*, 2003; *Bookhagen and Burbank*, 2010). The six-fold east to west rainfall gradient (Figure 4.1a) corresponds to an along-strike decrease in in vegetation density (Figure 4.1b). We take advantage of these along-strike gradients and published

^{10}Be terrestrial cosmogenic nuclide (TCN) denudation rates (*Bookhagen and Strecker*, 2012b; *Bookhagen*, submitted to Geology; *Godard et al.*, 2012; 2014; *Scherler et al.*, 2014; *Le Roux-Mallouf et al.*, 2015; *Morell et al.*, 2015; *Olen et al.*, 2015; *Portenga et al.*, 2015) to investigate the relationships between climate, denudation rates, and topography along strike of the Himalaya. We assess the potential influence of rainfall and vegetation using 12 years of calibrated remotely-sensed rainfall (TRMM 2B31, *Bookhagen and Burbank*, 2010) and 14 years of remotely-sensed vegetation density measurements (MODIS MOD13C1, *Huete et al.*, 1994; *Justice et al.*, 1998). We combine this analysis with topographic metrics, lithologic and tectonic constraints, and the compiled dataset of ^{10}Be TCN denudation rates. Despite several studies that highlight the dominance of tectonic uplift in forcing denudation rates across strike (e.g., *Burbank et al.*, 2003; *Godard et al.*, 2014; *Scherler et al.*, 2014; *Morell et al.*, 2015), we find evidence that climate and vegetation exert a strong influence on the range and variability of denudation rates along strike of the Himalayan orogen, and on the nature and strength of the relationship between denudation rate and topographic steepness.

4.2 Synthesis and new observations: Denudation rates across the Himalaya

To characterize denudation rates along strike of the Himalaya, we compiled a dataset of 214 ^{10}Be TCN denudation rates from recently published studies (Table S4.1). From west to east, the compiled dataset includes: the Sutlej Valley in northwest India (*Bookhagen and Strecker*, 2012b; *Bookhagen, submitted to Geology*); Garhwal Himalaya West *(Scherler et al.*, 2014); Garhwal East (*Morell et al.*, 2015); Central Nepal (*Godard et al.*, 2012; 2014); Eastern Nepal (*Olen et al.*, 2015); and Bhutan (*Le Roux-Mallouf et al.*, 2015; *Portenga et al.*, 2015), hence referred to as Bhutan West and Bhutan East, respectively (Figure 4.2a). All denudation rates were recalculated using the Lal/Stone (*Lal*, 1991; *Stone*, 2000) scaling scheme, which takes into account time-dependent muogenic production and non-dipole geomagnetic effects (*Balco et al.*, 2008), and the revised ^{10}Be half-life of 1.387±0.016 Myr (*Chmeleff et al.*, 2010; *Korschinek et al.*, 2010) to ensure standardized data. We have, to the best of our ability, accounted for the possibility of native ^{9}Be in the compiled dataset (see Supplementary Material S1). To avoid complications from non-fluvial and transient processes in our dataset, we excluded

samples from the following environments: (1) catchments with >5% modern glacial coverage (45 samples total; 25 from Bhutan East (*Portenga et al.*, 2015)); (2) catchments with suspected or known recent landslide activity (6 samples total (*Scherler et al.*, 2014; *Olen et al.*, 2015); (3) catchments in a state of topographic transience (21 samples total; see Supplemental Material S2 for detailed description of how topographic transience was determined); and (4) large trans-Himalayan catchments that integrate several climatic, tectonic, and topographic regimes (14 samples total from the Sutlej and Arun Rivers). After excluding transient and non-fluvial catchments, our compiled dataset contains 136 samples collected in environments dominated by fluvial erosion.

Across strike in each region, we observe that high catchment-mean denudation rates generally correspond to topographic rises, with relatively low denudation rates where topographic change is low (Figure 4.2c-e). Median denudation rate along strike remains relatively constant (0.30 ± 0.12 mm/yr) (Figure 4.2b) over a distance of ~1500 km. The range of denudation rates generally decreases from west to east, primarily by a decrease in the highest denudation rates (e.g., 75th percentile) (Figure 4.2b). This is reflected in a steady west-to-east decrease in mean denudation rates, from 0.8 ± 0.9 mm/yr in the Sutlej Valley to ~0.29 ± 0.33 mm/yr in Bhutan.

Figure 4.2 (Next Page)

Compilation of ^{10}Be terrestrial cosmogenic nuclide (TCN) denudation rates from the Himalaya. (A) Digital elevation map of Himalaya (USGS GTOPO30, nominal 1-km resolution), with major rivers (dark blue), location of the Main Frontal Thrust, the current surficial expression of the Main Himalayan Thrust (black), extent of present-day glaciation (light blue) (GLIMS, 2005; http://www.glims.org/), and political boundaries (white). Mt. Everest/Sagarmatha is shown for spatial reference. Sample locations (catchment centroids) of ^{10}Be dataset are colored by original publication; gray circles represent samples that were excluded from the final dataset. (B) Boxplot of denudation rates from each study area, with coloring following sample color in (A). Median values for each study site are represented by the thick black bar; boxes extend from the 25th to 75th percentiles; whiskers extend to all samples not considered outliers. Mean values for each study area are shown in white. It is important to note that the discrepancy between median and mean denudation rates likely results from denser sampling in the more slowly denuding Lesser Himalaya. (C-E) Strike-perpendicular swath profiles from (C) NW India (*Bookhagen and Strecker*, 2012b; *Bookhagen, submitted to Geology*, *Scherler et al.*, 2014; *Morell et al.*, 2015), (D) Nepal (*Godard et al.*, 2012; *Godard et al.*, 2014; *Olen et al.*, 2015), and (E) Bhutan (*Le Roux-Mallouf et al.*, 2015; *Portenga et al.*, 2015). Elevation is averaged over swaths oriented perpendicular to local strike that encompass all included sample sites, denoted in (A). Thick black line denotes mean elevation, dark gray shade ±1σ, light gray shade ranges from minimum to maximum elevation values. Sample denudation rates are plotted against distance from the MFT, and follow the same color scheme as (A). This color scheme will be used for figures throughout the remainder of the manuscript.

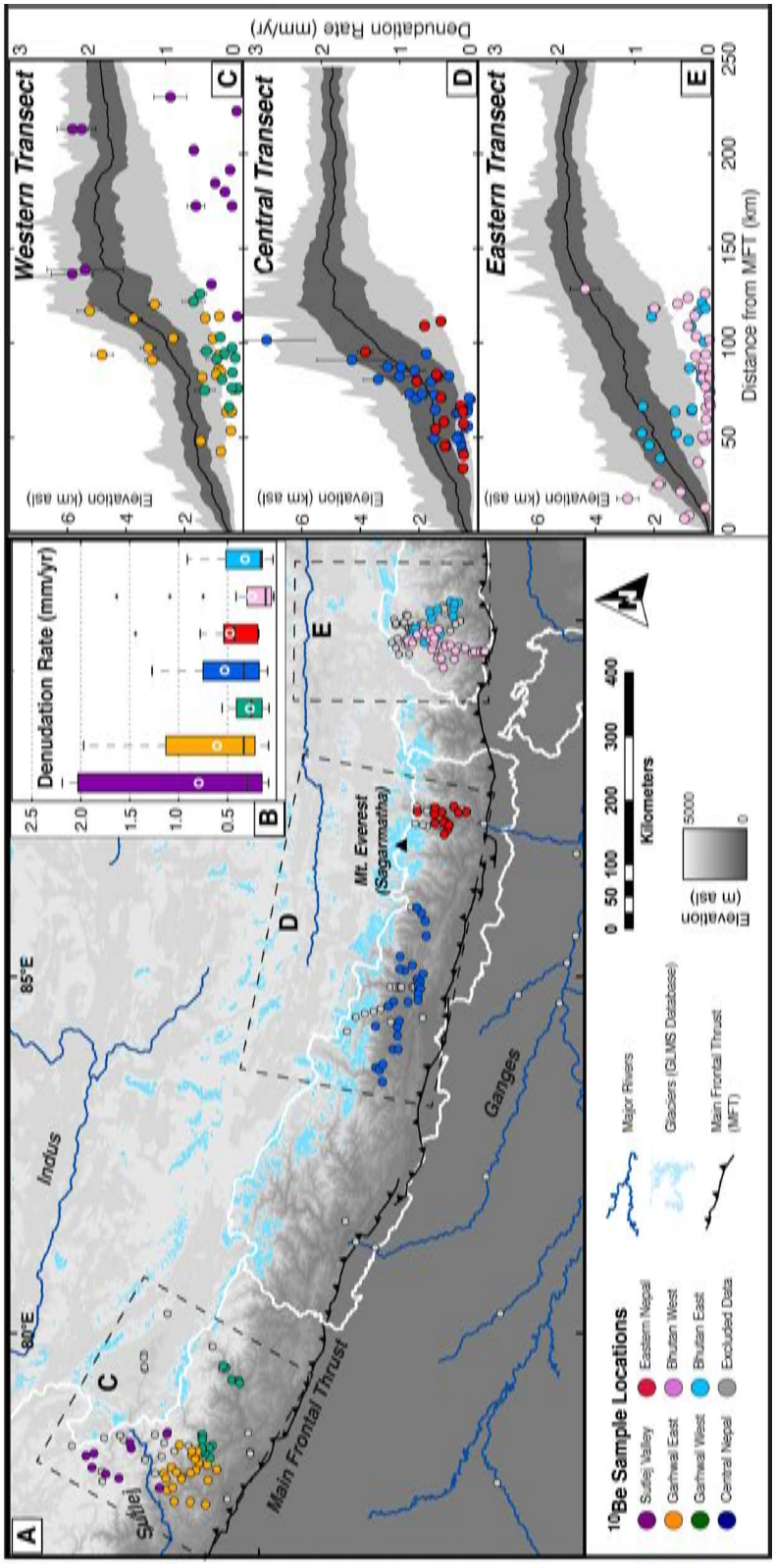

Figure 4.2 Compiled ^{10}Be dataset.

A traditional approach for empirically estimating the controls of denudation rates in active orogens is to compare local (e.g., catchment-scale) denudation rates with metrics that have been shown to positively correlate with tectonic uplift, e.g., hillslope gradient, normalized channel steepness (k_{sn}), or specific stream power (SSP) (*Whipple*, 2004; *Wobus et al.*, 2006; *Ouimet et al.*, 2009; *DiBiase and Whipple*, 2011; *Bookhagen and Strecker*, 2012a; *Kirby and Whipple*, 2012). We have calculated hillslope gradient, k_{sn}, and SSP for each sampled catchment in the dataset. To account for the possibility that higher rainfall rates will induce higher erosion, we additionally calculate k_{sn} and SSP with an MAR-weighted upstream area and discharge, respectively (see Supplementary Material S3 for topographic metric calculations). In Figure 4.3, we show the relationship between denudation rates and (1) k_{sn} and (2) hillslope gradient in the Himalaya. The raw data is shown with ordinary least squares (OLS) power law regressions for each study area and for the compiled dataset, following several studies that have observed a power law relationship between topography and denudation, where *topographic metric ~ (denudation rate)*^{b} (e.g., *DiBiase and Whipple*, 2011; *Bookhagen and Strecker*, 2012a; *Kirby and Whipple*, 2012; *Lague*, 2014). In most study areas (with notable exceptions, discussed below), the power law regression provides a moderate to good fit between denudation rates and tectonically-linked topographic metrics. However, the nature of the power law relationship varies considerably between study areas (see Table S4.2 for full regression results for each study area). Although denudation rates and topographic metrics are significantly correlated for the entire Himalaya dataset ($p<0.05$), the regressions provide a poor fit to the data (e.g., $R^2_{ksn}=0.26$, $R^2_{Hillslope}=0.18$) (Figure 4.3c,d). The range of power law exponents in each individual regression, and the poor goodness-of-fit in the compiled regression, suggests that there are one or more complicating factors causing scatter in the dataset (e.g., *Kirby and Whipple*, 2012). In a global compilation of ^{10}Be derived catchment-mean denudation rates, Lague (2014) also found that the relationship of k_{sn} *~ (denudation rate)*^{b} varied considerably between regions, with the power law exponent ranging from highly non-linear (b=0.25 in the Mendocino Triple Junction) to nearly linear in the Siwaliks (b=0.93). In the Himalaya, we likewise observe a range of power law values characterizing the relationship between

denudation rates and k_{sn}; from shallow and highly nonlinear in the Garhwal Himalaya (b_{ksn}=0.21-0.23), to a steeper and increasingly linear relationship in Nepal (b_{ksn}=0.44-0.49). In the following sections, we investigate possible causes and contributing factors to the distribution of denudation rates along strike of the Himalaya and the relationship between denudation rates and topography.

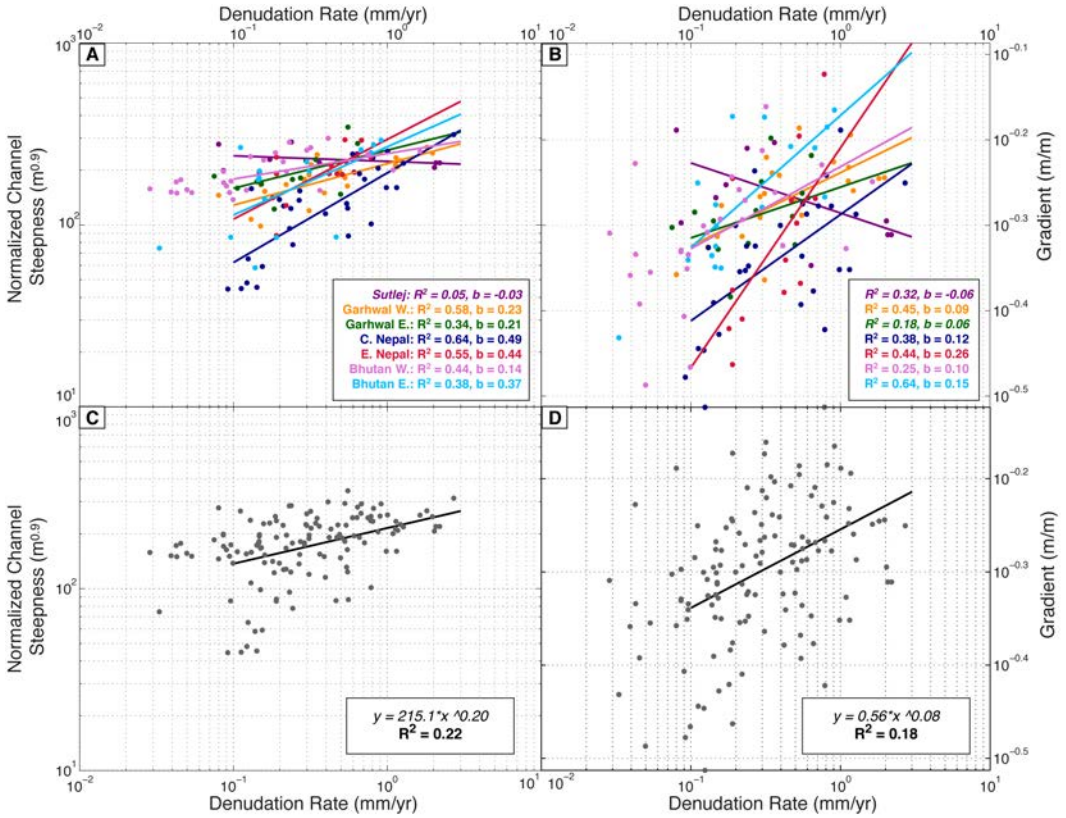

Figure 4.3 Functional relationships between topography and denudation.

Power law relationship between ^{10}Be TCN-derived denudation rates and catchment-mean values of (A,C) normalized channel steepness (k_{sn}), and (B,D) hillslope gradient. (A) and (B) show data plotted with individual OLS power law regressions for each study area. Inset gives power law exponent *b*, following the relationship $f(x)=ax^b$, and goodness-of-fit (R^2) for each regression. Italic text denotes where correlation is not significant at the 95% confidence level. Additional correlation statistics for each study area can be found in Table S4.1. (C, D) show regression for the compiled dataset, highlighting the poor fit between denudation rates and topographic metrics when all data is considered together.

4.3 Data and methods

4.3.1 Geology and tectonics

The Himalayan orogen can be divided into four major lithologic groups, separated by four major fault systems. From the foreland to the hinterland, they are: (1) the Cenozoic sedimentary deposits of the Siwaliks north of the Main Frontal Thrust (MFT); (2) the Lesser Himalaya Series, ranging from low- to high-grade metasediments (high-grade metasediments are also known as the Lesser

Himalayan Crystalline, or LHC) north of the Main Boundary Thrust (MBT); (3) the Higher Himalayan Crystalline (HHC), predominantly granites and high-grade metamorphic rocks, separated from the LHC by the Main Central Trust (MCT); and (4) the Paleozoic sedimentary rocks of the Tethyan Himalaya, north of the South Tibetan Detachment (STD) (e.g., *Gansser*, 1964; *Le Fort*, 1975; *Gansser*, 1980; *Hodges*, 2000). Using the compiled geologic maps of Hodges (2000) for NW India and Nepal and Grujic et al. (2011) for Bhutan, we created a simplified lithologic map for the Himalaya divided into: Quaternary sedimentary deposits, sedimentary rocks, metasedimentary rocks, and crystalline rocks; approximately corresponding with the Siwaliks and intermontane basins, Tethyan Himalaya, Lesser Himalayan Series, and Higher Himalayan Crystalline, respectively. Based on this simplified lithologic map, we characterize each basin by the percent area in each lithology.

If lithology exerts a primary control on denudation rates or on the relationship between denudation rates and topography, we might expect basins from similar lithologies to fit the same relationship between denudation rate and topographic metric. Thus, by separating denudation rates into subsets based on basin lithology, one would expect a reduction of scatter in each subset. To test this, we binned our dataset into dominant lithology (>50% area) and perform a suite of regressions and correlation analysis between denudation rates and common tectonically-linked topographic metrics (Table 4.1).

Table 4.1 Geologic, tectonic, climatic, biotic, and topographic metrics

Lithology and Tectonics	Climate	Vegetation	Topography
% Crystalline [1]	TRMM 12-year MAR (mm/yr) [3]	14-year mean annual EVI [4]	Hillslope gradient (m/m) [6]
% Metasediments [1]	MAR - ET (mm /r) [5]	Vegetation seasonality index (SI) [4]	k_{sn} ($m^{0.9}$) [6]
% Sediments [1]	MAR - PET (mm/yr) [5]	Dominant land cover [7]	MAR-weighted k_{sn} ($m^{0.9}$) [6]
HHC exhumation rate (mm/yr) [2]		(75th - 25th percentile EVI) annual, summer [4]	SSP (W/m^2) [10]
LHC exhumation Rate (mm/yr) [2]			MAR-weighted SSP (W/m^2) [10]

The exposure of lithologic units in the Himalaya corresponds to relatively old phases of tectonic activity and mountain building during the Cenozoic (*Hubbard and Harrison*, 1989), and is likely not representative of very recent tectonic activity. Thus, to investigate the link between modern denudation rates and geologically young uplift and exhumation rates, we compare our data to the low-temperature thermochronology dataset compiled by Thiede and Ehlers (2013). This dataset comprises Apatite fission track, Zircon fission track, and (^{40}Ar/^{39}Ar)-white mica ages and calculated exhumation rates for HHC and LHC lithologies along strike of the orogen. Exhumation rates calculated from low-temperature thermochronology are averaged over millions of years (e.g., *Ehlers*, 2005); such values therefore represent chronologies three to four orders of magnitude longer than ^{10}Be-derived denudation rates. Consequently, we use exhumation rates based on low-temperature thermochronology data as relatively long-timescale estimates of present-day tectonic uplift or exhumation (last 0-2 Myr for the LHC and 0-4 Myr for the HHC). We used the nearest measurements of tectonic exhumation along strike to characterize recent uplift for each study area. In the case of data gaps, (e.g., HHC exhumation rates in Eastern Nepal, see Figure 4.4), we perform a bilinear interpolation between observations. Exhumation rate estimates for the LHC do not spatially extend to the east past Central Nepal, and we accordingly assign no-data values to Eastern Nepal and Bhutan.

Present rates of tectonic uplift are believed to be reflected in a physiographic divide between the low-elevation and relatively low-relief Lesser Himalaya and the high-elevation, high-relief Higher Himalaya (e.g., *Hodges et al.*, 2001; *Avouac*, 2003; *Bollinger et al.*, 2004; *Robert et al.*, 2009). This physiographic transition, commonly termed the PT_2 (*Hodges et al.*, 2001), does not correspond to the geologic boundaries of the Lesser Himalayan Series/Crystalline and the Higher Himalayan Crystalline or to the location of the Main Central Thrust (MCT) along strike (*Hodges et al.*, 2001; *Wobus et al.*, 2005; *van der Beek et al.*, 2006; *Harvey et al.*, 2015). Although there are different models for what may cause this transition, including out-of-sequence thrusting (*Hodges et al.*, 2004; *Wobus et al.*, 2005) or exhumation over a mid-crustal ramp (*Cattin and Avouac*, 2000; *Avouac*, 2003; *Bollinger et al.*, 2004; *Schulte-Pelkum et al.*, 2005; *Morell et al.*, 2015), there is considerable data documenting

differential uplift on either side of the PT_2 (e.g., *Copeland et al.*, 1991; *Jackson and Bilham*, 1994; *Wobus et al.*, 2005; *Blythe et al.*, 2007; *Robert et al.*, 2009; *Morell et al.*, 2015). We therefore separated our dataset into physiographic bins corresponding to: (1) the physiographic Lesser Himalaya (LH), from the MBT to the PT_2; and physiographic Higher Himalaya (HH), extending from the PT_2 to the STD. Due to its differing tectonic and topographic setting (*Coutand et al.*, 2014; *Adams et al.*, 2015; *Le Roux-Mallouf et al.*, 2015) (Figure 4.2e), we exclude the Bhutan data from these bins. We perform regression and correlation analysis between denudation rates and topographic and climatic metrics (Table 4.1) to determine if the spread of denudation rates in the compiled dataset can be explained by physiographic region and, we therefore infer, recent tectonic activity.

4.3.2 Climate and vegetation

Rainfall in the Himalaya was characterized using the Tropical Rainfall Measurement Mission (TRMM) 2B31 12-year calibrated mean annual rainfall (MAR), with a nominal spatial resolution of 5-km (*Bookhagen and Burbank*, 2010). We acknowledge that the TRMM 2B31 product does not include snowfall, which has a larger influence in the Western Himalaya, where winter precipitation is greater due to proximity to the Westerlies (e.g., *Bookhagen and Burbank*, 2010). To estimate effective water availability for surface processes, we also take into consideration the effects of evapotranspiration (ET) and potential evapotranspiration (PET). Evapotranspiration is the sum of evaporation and plant transpiration. This value is based on the Penmen-Montieth equation, which incorporates remotely-sensed atmospheric and terrestrial data, such as temperature, wind speed, relative humidity, and solar radiation (*Monteith*, 1965; *Mu et al.*, 2007; *Mu et al.*, 2011); potential evapotranspiration is the amount of evaporation and transpiration that would occur given sufficient water. We calculated MAR-ET and MAR-PET using the MOD16 product from the Moderate-Resolution Imaging Spectroradiometer (MODIS) sensor aboard the NASA Earth Observing System Terra satellite *(Mu et al.*, 2011).

Vegetation density in the Himalaya was quantified using the Enhanced Vegetation Index (EVI). EVI is a remotely-sensed measure of vegetation density

derived from multispectral analysis of the red, near infrared, and blue wavelengths (see Supplementary Material S4 for details) (*Huete et al.*, 1994; *Justice et al.*, 1998; *Huete et al.*, 1999). Valid values of EVI range from 0 to 1, with 0 representing bare land and 1 representing extremely dense vegetation cover. Due to its relatively long temporal coverage, we use the MODIS product MOD13C1, a 16-day composite EVI at 0.05 degree (nominal 5-km) resolution. Employing 14 years of available MODIS vegetation indices, we calculated mean annual, monthly, summer (May to October, MJJASO), and winter (November to April, NDJFMA) EVI. To test if denudation rates are sensitive to the seasonality of vegetation density, rather than mean annual vegetation density, we calculated a seasonality index (SI) to quantify the difference between summer and winter vegetation, such that:

$$\mathrm{SI} = \frac{\mathrm{EVI}_{MJJASO}}{EVI_{NDJFMA}} \tag{4.1}$$

The seasonality index therefore quantifies how much denser summer vegetation is than winter vegetation (e.g., a value of SI=1 indicates no vegetation seasonality, while a value of SI=2 implies that vegetation is twice as dense in the summer than in the winter; see Figure S4.1). The range of annual and summer EVI within each basin was measured as the difference between 75th and 25th percentiles. Assuming that higher and lower values of EVI correspond to changes in vegetative land cover type (e.g., forest, grassland, alpine vegetation), we used this range as a proxy for the variety of land cover within each basin (see Supplementary Material S4.1 for the relationship between EVI and land cover in the Himalaya). We assume that a low range of EVI within a basin corresponds to relatively uniform land cover, while a large range represents a variety of land covers within the basin. Correspondingly, we expect that when land cover is more uniform, the erosive processes acting within a basin will be more spatially uniform; when land cover varies, the erosive processes within a basin are more likely to vary

4.3.3 Denudation rate variability and regression analysis

In the compiled dataset, we observe that the range of denudation rates generally decreases from west to east (Figure 4.2b). To test possible factors

controlling the variability of denudation rates along strike, we calculate the denudation rate variability for each study area as the (75^{th}–25^{th}) percentile of all denudation rates within a given study area. Correlation and regression statistics (R^2, R, and corresponding p values) were then calculated between the denudation rate variability of each study area and the median value of topographic, rainfall, and vegetation metrics for each study area (Table 4.1).

As discussed in section 2 above, we observe markedly different power law relationships between denudation rates and topography between the study areas along strike. These relationships vary both in the strength of the correlation (R and R^2; Table S4.2) and in the power law coefficient *b*. We examine the correlation between the strength (R^2, R) and degree of linearity (power law coefficient *b*) of the *topographic metric ~ (denudation rate)*^{b} relationship to dominant lithologic unit, and tectonic, climatic, and vegetation metrics for each study area (Table 4.1). Such correlation analysis allows us to examine if, e.g., higher tectonic uplift rates result in a more or less linear relationship between denudation rates and hillslope gradient; or if increased rainfall rates lead to a stronger or weaker correlation between denudation rates and normalized channel steepness. Several studies have highlighted the importance of channel geometry and width to the relationship between topography and denudation (*Finnegan et al.*, 2005; *Yanites and Tucker*, 2010; *Yanites et al.*, 2010b; *Fisher et al.*, 2013). We acknowledge that variations in channel width along strike may impact the relationship between topographic metrics and denudation rates; however, due to lack of accurate estimates of channel width at the orogen scale, we do not presently consider this factor.

4.4 Results

4.4.1 Geology and tectonics

Catchments in the compiled ^{10}Be dataset are predominantly located within crystalline and metasedimentary rocks of the HHC and LHC lithologic units. Basins dominated by Tethyan Sediments are confined to the Sutlej Valley and Bhutan (Table 4.2). We observe no basins with dominant Quaternary sedimentary fill deposits, therefore our binned subsets are: sedimentary, metasedimentary, and crystalline catchments. Denudation rates binned by lithologic units show

significant correlation at the 95% confidence level with several topographic metrics, but significant correlation is not consistent between lithologies, and the regression provides a poor fit to the data ($R^2 \leq 0.45$), and in most cases the correlation is weak ($|R|<0.5$). See Table S4.3 for full regression and correlation results.

Table 4.2 Regional lithology

Lithology	Sutlej Valley	Garhwal West	Garhwal East	Central Nepal	Eastern Nepal	Bhutan West	Bhutan East
Crystalline	24.30%	50.30%	23.70%	18.60%	13.20%	95.40%	71.30%
Metasediments	3.90%	49.70%	76.30%	80.00%	86.80%	0.00%	0.00%
Sediments	71.80%	0.00%	0.00%	0.00%	0.00%	4.60%	28.70%
Quaternary Fill	0.00%	0.00%	0.00%	1.40%	0.00%	0.00%	0.00%

Figure 4.4 depicts long-term exhumation rates along strike from the Higher and Lesser Himalaya, along with ^{10}Be denudation rates from the corresponding physiographic region. In the Lesser Himalaya, Thiede and Ehlers (2013) document a west to east increase in exhumation rates over the last 2 Myr from ~1 to 2.5 mm/yr. However, we observe no along-strike gradient in denudation rates during the past 10^2-10^3 yr (Figure 4.4b). There is no significant correlation between exhumation rates from low-temperature thermochronology and ^{10}Be denudation rates in the LH. The opposite is observed in the Higher Himalaya: although denudation rates remain generally lower than long-term exhumation rates, they follow a similar spatial pattern along strike, with highest exhumation and denudation rates in Central Nepal, moderate rates in the Western Himalaya, and relatively low rates of exhumation and denudation in Bhutan. We observe a significant positive relationship between long-term HH exhumation rates and short-term HH denudation rates ($R=0.83$, $p<0.05$). However, despite the apparent influence of long-term exhumation on millennial denudation rates, there are no significant correlations between denudation rates and tectonically-linked topographic metrics (e.g., k_{sn}) in the Higher Himalaya. In the Lesser Himalaya, despite the apparent decoupling of denudation rates from long-term exhumation rates, there are significant correlations at the 95% confidence level between denudation rates and tectonically-linked topographic metrics; however, the correlation is weak ($|R|<0.5$, $R^2 \leq 0.30$ for all metrics). See Table S4.4 for full regression results.

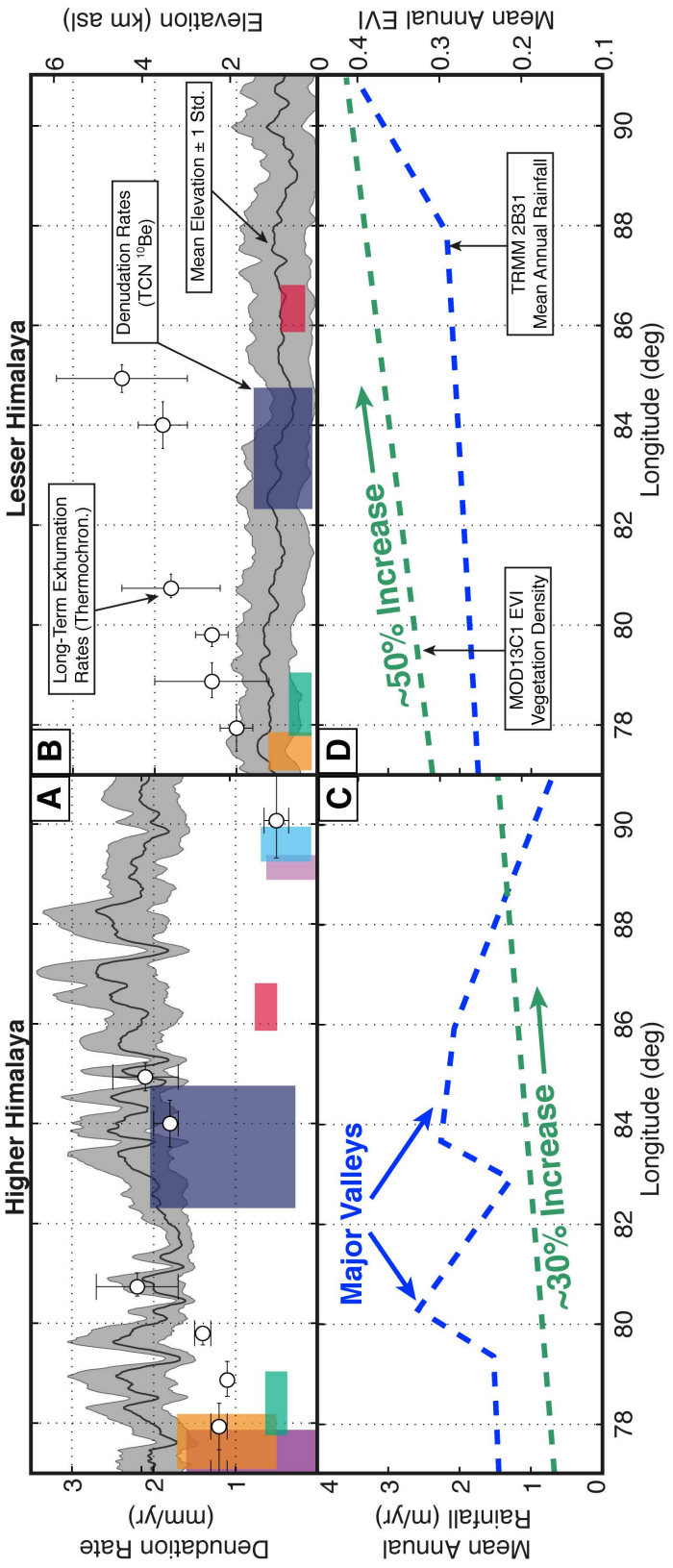

Figure 4.4 Exhumation and denudation rates in the Higher and Lesser Himalaya.

(A, B) Comparison between short-term denudation rates derived from ^{10}Be TCN concentrations and long-term exhumation rates from low-temperature thermochronology (*Thiede and Ehlers*, 2013) for the Higher and Lesser Himalaya, respectively. Elevation along strike is shown in dark gray, with ±1σ in light gray. Long-term exhumation rates are shown as white circles, with horizontal error bars extending to the area integrated into mean exhumation rate values (following Thiede and Ehlers (2013); vertical error bars show ±1σ uncertainty. Short-term denudation rates are shown in boxes that extend, horizontally, to spatial extent of dataset and, vertically, to the ±1σ uncertainty. Long-term exhumation rates and short-term denudation rates show a similar pattern in the Higher Himalaya, with highest denudation/exhumation in Central Nepal and lower rates in both NW India and Bhutan. Long-term exhumation and short-term denudation rates in the Lesser Himalaya, however, appear to be decoupled. While exhumation rates increase towards the east, short-term denudation rates remain relatively constant throughout the Lesser Himalaya. (C, D) Simplified mean annual rainfall (blue) and vegetation density (green) along strike for the Higher and Lesser Himalaya, respectively. Swaths were taken from 1.5 decimal degree (~110 km) wide swaths parallel to the strike of the mountain range, centered on the Higher Himalayan front and binned by elevation, approximately corresponding to the Lesser (< 2500 m asl) and Higher (> 2500 m asl) Himalaya.

4.4.2 Climate and vegetation

In general, rainfall and vegetation density increase from west to east along the strike of the Himalaya (Figure 4.4). At lower elevations (<2500 m asl), vegetation density and rainfall increase relatively steadily from west to east. At high elevations, however, rainfall no longer follows a clear along-strike gradient and is instead influenced by large valleys that are oriented approximately perpendicular to strike, funneling moisture into the orogen (*Bookhagen et al.*, 2005b; *Anders et al.*, 2006) (Figure 4.4c). Vegetation density continues to increase eastward at higher elevation, but the gradient is more subdued.

We performed correlation analysis between the entire ^{10}Be dataset, as well as the HH and LH subsets, and climatic and vegetation metrics from each sample basin. Denudation rates from the entire dataset, and from the Higher Himalaya in particular, show a significant positive correlation with the range of summer EVI values in each catchment (entire dataset: $R=0.67$, $p<0.05$; Higher Himalaya: $R=0.70$, $p<0.05$). A similar, though slightly weaker, correlation exists between denudation rates and annual EVI range. We do not see the same correlation in the Lesser Himalaya, where the range of EVI (summer or annual) is relatively small. See Table S4.4 for full regression results.

4.4.3 Denudation rate variability

Denudation rate variability in each study area shows a strong correlation with all vegetation density metrics (Table S4.5). The strongest correlation is with the seasonality index, with denudation rate variability increasing as vegetation seasonality increases ($R^2=0.97$, $R=0.99$, $p<0.05$) (Figure 4.5). There is also a strong negative correlation between denudation rate variability and vegetation density (EVI; $R^2=0.80$, $R=-0.90$, $p < 0.05$), where denudation rate variability decreases as mean annual vegetation density increases (Figure 4.5). Notably, there are no significant correlations between denudation rate variability and topographic, tectonic, lithologic, or rainfall metrics (cf. Table S4.5). Denudation rate variability is significantly higher in the Sutlej Valley, where vegetation density and rainfall are considerably lower, and seasonality higher, than in the rest of the dataset. Therefore, to test whether or not the relationship between denudation rate variability and vegetation holds without this outlying data point, we performed regressions excluding the Sutlej Valley. Without the Sutlej Valley

data, the relationship between mean annual EVI and denudation rate variability breaks down (R^2=0.15, R=-0.38, p>0.1) (Figure 4.5a). However, seasonality remains highly correlated to denudation rate variability even when the Sutlej Valley data is excluded (R^2=0.87, R=0.93, p<0.05) (Figure 4.5b). The regression excluding the Sutlej Valley is nearly identical to the regression of all study areas.

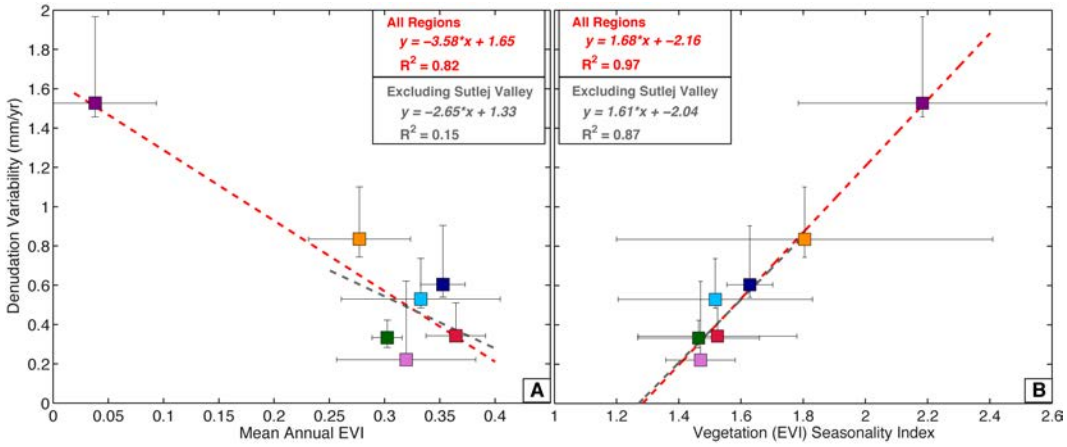

Figure 4.5 Denudation rate variability.

Denudation rate variability in each study area plotted against (A) mean annual EVI; and (B) EVI seasonality index (summer/winter vegetation density, cf. Equation (4.1)). Denudation rate variability for each study area is calculated as the 75^{th}-25^{th} percentile of denudation rates in each study area. Vertical error bars extend to the 90^{th}-75^{th} percentile and 25^{th}-10^{th} percentile. Linear OLS regressions were performed for the entire dataset (red); and for the dataset excluding the Sutlej Valley (gray). Correlation and regression statistics of denudation rate variability compared to all lithologic, tectonic, and climatic parameters can be found in Table S4.4.

4.4.4 Regression analyses

We observe no significant relationship between the power law exponent and tectonic uplift rates or lithology along strike (Table S4.6). Instead, we note strong significant correlations between the power law exponent and both climate and vegetation metrics (Figure 4.6). We document statistically significant, positive correlations between the power law exponent *b* and MAR (as well as MAR-ET and MAR-PET) and vegetation density (R>0.8 in all cases, see Table S4.6 for complete correlation statistics). Thus, as rainfall or vegetation density increase, the relationship between denudation rates and topographic metrics becomes increasingly linear. Conversely, when rainfall or vegetation density is low, the relationship between denudation rates and standard topographic metrics is increasingly non-linear.

There is also a significant correlation between rainfall and vegetation metrics and the strength of the correlation between denudation rates and topographic metrics. Both R^2 and R values increase as rainfall (MAR, MAR-ET, MAR-PET) and vegetation density (EVI) increase (see Table S4.7 for all results). No significant correlation was observed between tectonic or lithologic units and the strength of the correlation between denudation rates and topography.

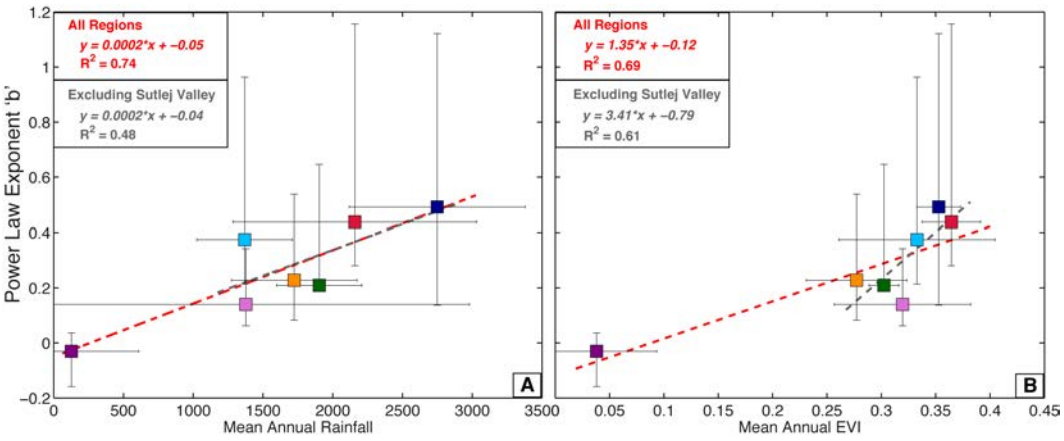

Figure 4.6 Degree of linearity.

The power law exponent *b* of the functional relationship *(topographic metric)*^{b} *~ denudation rate* plotted against (A) mean annual rainfall and (B) mean annual EVI for each study area. Vertical error bars extend to the 95% confidence intervals of *b*. Linear OLS regressions were performed for the entire dataset (red) and for the dataset excluding the more interior Sutlej Valley (gray). Correlation and regression statistics of power law exponent *b* to all lithologic, tectonic, and climatic parameters can be found in Table S4.5.

4.5 Discussion

Several studies have put forth evidence that tectonic processes control the rates and patterns of denudation across strike in the Himalaya (*Burbank et al.*, 2003; *Scherler et al.*, 2014; *Godard et al.*, 2014; *Morell et al.*, 2015; *Le Roux-Mallouf et al.*, 2015). Conversely, other recent studies argue for an along-strike climatic impact in the evolution of the Himalayan fold-and-thrust belt (*Hirschmiller et al.*, 2014). In our analysis, we find no clear evidence that tectonic uplift or lithologic units control the variations in denudation rates that we have observed along strike of the orogen. No consistent significant correlation is observed between denudation rates and common, tectonically-linked topographic metrics when samples are binned by physiographic region, assumed to correspond to modern and recent tectonic uplift, or by major lithologic unit (%HHC, %LHC). Similarly, when we compare the exponent *b* of the power law relationship between denudation rates and topography, we find no correlation between *b* and dominant lithologic unit, or recent exhumation rates from the Higher or Lesser

Himalaya. We therefore interpret that the along-strike patterns we observe in denudation rate variability and the linearity of the functional relationship between topographic metrics and denudation rates cannot be explained by variations in the degree of tectonic activity or lithology along strike. Accordingly, we infer that one or more other factors must be responsible for the along-strike variations in denudation rate variability and the relationship between denudation rate and topography.

Vegetation density and seasonality show a strong correlation to denudation rate variability (R=-0.90 and R=0.99, respectively). Denudation rate variability decreases linearly as vegetation density increases, and increases as seasonality increases (Figure 4.5). The strong correlation between an increase in denudation rate variability as the seasonality of vegetation increases suggests that not only is the mean annual vegetation density important in stabilizing erosive regimes and decreasing denudation rate variability, but that the degree of seasonal change in vegetation density also plays an important role. High seasonality results in dynamic and temporally variable vegetation cover and density, marked by annual transitions from sparse or bare winter cover to denser summer vegetation. We also measure spatially variable vegetation density by the range of EVI values within a catchment. The positive correlation we observe between denudation rates and EVI range suggests that the spatial variability of vegetation also directly impacts denudation rates. Studies in other regions have suggested that transitional vegetation regimes correspond to high denudation rates in the Central Andes of Chile (*Carretier et al.*, 2013) and in the Kenyan Rift (*Torres Acosta et al.*, 2015). Seasonality and EVI range may have a similar effect, with the highest denudation rates corresponding to regions where transitional vegetation regimes bridge the gap between temporally and spatially variable vegetation density and land cover. The link between vegetation density, seasonality, and denudation rate variability may also be applicable when interpreting the results of paleo-denudation rates (e.g., from fluvial terraces). Significant scatter observed in paleo-denudation rates from past glacial periods (e.g., Late Pleistocene in the Garhwal Himalaya (*Scherler et al.*, 2015)) may be the result of more variable denudation during periods with sparser and more seasonal vegetation cover. Consequently, potential environmental changes, such as past increases in seasonality, will need to be taken into account when interpreting paleo-denudation rates.

The high variability of denudation rates in sparsely vegetated regions with high seasonality may also explain the correlation we observe between vegetation density and the strength of the relationship between denudation rates and topographic metrics (R_{ksn}=0.82; Table S4.7). High denudation variability induced by lack of vegetation cover results in poor correlation of denudation rates to standard topometrics. In wetter, more densely vegetated environments of the Himalaya, we consequently expect to observe a stronger correlation between denudation rates and topography than in sparsely vegetated environments. We also observe a positive relationship between the power law exponent *b* and both vegetation density and rainfall rate. Thus as rainfall rate or vegetation density increases, there is a corresponding increase in the linearity of the relationship between denudation rate and topographic metrics. In Eastern Nepal, where rainfall and vegetation density is high, the relationship between denudation rate and k_{sn} is more linear than in the Sutlej Valley or Garhwal Himalaya, where rainfall rate and vegetation density are lower (Figure 4.6). It is notable that in the wet and densely vegetated Siwaliks, Lague (2014) found a highly linear relationship between denudation rate and k_{sn} (*b*=0.93) (*Kirby and Whipple*, 2001; *Wobus et al.*, 2006; *Lague*, 2014), supporting our observation of increasing linearity with greater vegetation density and higher rainfall.

A similar result was found by Torres-Acosta et al. (2015) in the East African Rift System. In this tectonically and climatically very different region, where denudation rates and uplift rates are slow and topographic steepness is low, the observed relationship between denudation rate and hillslope gradient is linear. However, these authors found that the slope of the relationship between denudation rate and hillslope gradient (where hillslope is the dependent variable) steepens as vegetation density increases. Thus on the steep and densely vegetated slopes of the rift escarpments, denudation rates are lower than in regions where vegetation is considerably sparser. Both the increasing linearity of largely non-linear functional relationships in the tectonically very active Himalaya and the increasing slope of the linear functional relationships in the tectonically less active East African Rift suggest that denser vegetation cover allows landscapes to become increasingly steep as a function of denudation rate, confirming the results of modeling studies (*Collins et al.*, 2004). The shift in linearity in the relationship between denudation rates and topographic steepness can also reflect a change in

the relative importance of topographic threshold values as denudation rates increase. Several studies have found that topography will steepen in response to increasing denudation rates until it reaches a threshold value, above which the landscape cannot continue to steepen in response to changes in uplift or denudation rates (e.g., *Burbank et al.*, 1996b; *Montgomery*, 2001; *Binnie et al.*, 2007; *Ouimet et al.*, 2009). As denudation rates increase in densely vegetated regions, however, topography is able to continue to steepen to a greater degree than in sparsely vegetated regions, where threshold hillslope angles are reached earlier as denudation rates increase. A positive relationship between vegetation cover and topographic steepness has been observed in other orogens; in the Central Andes, for example, Jeffery et al. (2014) observed that hillslope gradients positively correlate to vegetation cover, and that more continuously vegetated slopes tend to be steeper than gentler hillslopes with bare or patchy vegetation cover.

4.5.1 Deciphering the effects of rainfall and vegetation

The observation that the highest mean denudation rates and the highest denudation rate variability are associated with regions characterized by the lowest rainfall rates (e.g., in the Sutlej Valley) to provide surface runoff for erosion appears counterintuitive at first sight. If rainfall sets the along-strike pattern of denudation rates, the highest denudation rates should correspond to high rainfall rates. However, mean annual rainfall may not be characteristic of how rainfall impacts denudation rates. The temporal variation of rainfall (e.g., seasonality) has been hypothesized to modulate erosion (*Snyder et al.*, 2003b; *Lague et al.*, 2005). Storminess has also been proposed as an important driver for erosion and sediment transport (e.g., *Gabet et al.*, 2004; *Wulf et al.*, 2010; 2012). We analyzed the seasonality of Himalayan rainfall and the number of extreme rainfall events (Figure 4.7). The percent of annual rainfall that occurs during the summer (MJJASO) increases from west to east, from 40 to 80% in the western Himalaya to >80% in the central Himalaya and Bhutan (Figure 4.7a) (cf. *Bookhagen and Burbank*, 2010). This decrease in seasonality is caused by the greater impact of moisture from the winter Westerlies in the western Himalaya (e.g., *Barros et al.*, 2006; *Wang*, 2006; *Cannon et al.*, 2015), resulting in higher winter rainfall in the

western Himalaya with respect to the monsoon-dominated regions to the east. Extreme rainfall events are defined as rainfall events that exceeded the 90th percentile rainfall rate for the 12-year time series of TRMM data at that pixel (number/year) (cf., *Bookhagen*, 2010). The highest number of extreme rainfall events is documented in the eastern syntaxis of the orogen in NE India and decreases steadily westward (Figure 4.7b). Higher seasonality of rainfall or an increased number of storms and extreme rainfall events may drive higher and more variable denudation rates, even when mean annual rainfall is low. However, we observe that denudation rate variability is lowest where rainfall seasonality is high (>80%) and extreme rainfall events are relatively frequent (3-9/year). We argue that this effect is due to the stabilizing influence of vegetation on the landscape.

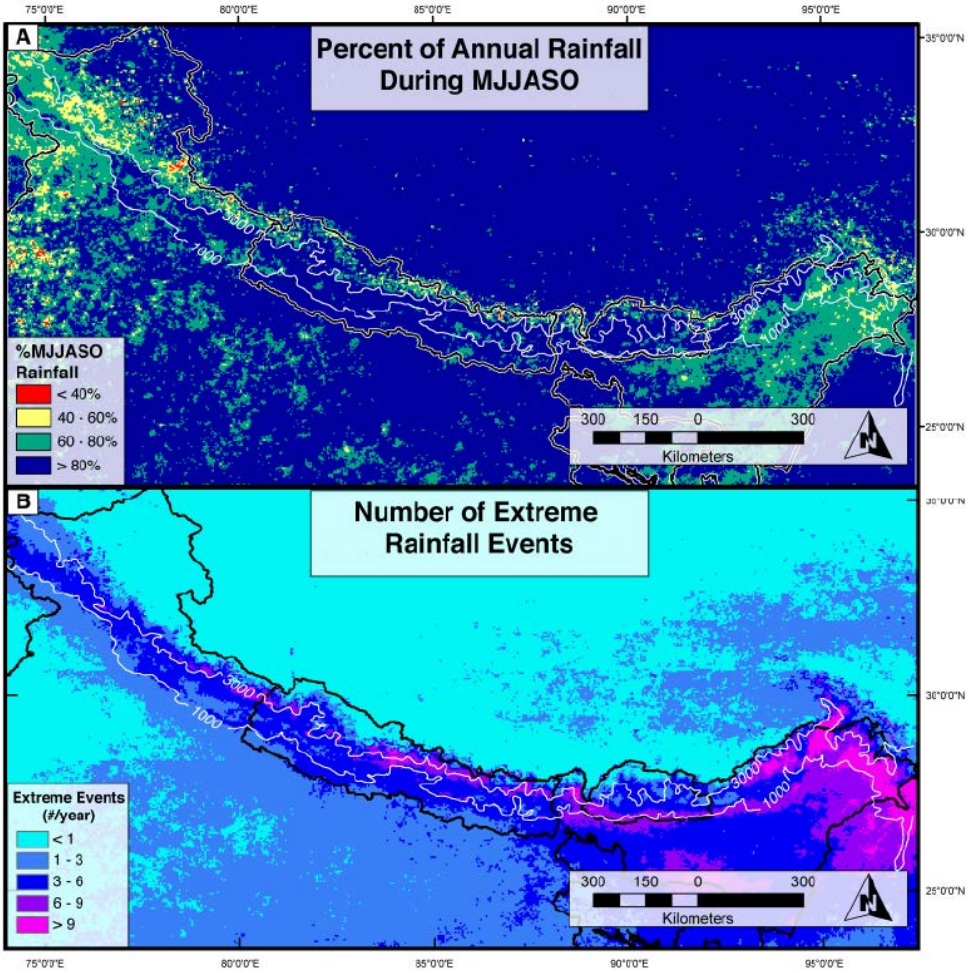

Figure 4.7 Rainfall seasonality and extreme events

(A) Map of TRMM2B31 rainfall seasonality for the Himalaya region. Rainfall seasonality is defined as the percent of total annual rainfall that occurs during the MJJASO summer months (*Bookhagen and Burbank*, 2010). (B) Map of extreme rainfall events for the Himalaya region. Extreme events are defined as those above the 90th percentile of the 12-year time series for each pixel.

We suggest that in humid, monsoon-influenced regions with high vegetation density, vegetation cover moderates the effects of highly seasonal rainfall and the impact of extreme rainfall events, resulting in less variable denudation rates. The dense, persistent vegetation cover in these regions buffers the landscape from rainfall-driven erosion via the stabilizing effect of root cohesion, higher infiltration rates, and shielding from rain splash (e.g., *Prosser and Dietrich*, 1995; *Wainwright et al.*, 2000; *Gyssels and Poesen*, 2003; *T Dunne et al.*, 2010). Where vegetation density is low, rainfall converts rapidly into surface runoff to drive erosion. The western regions of the Himalaya (e.g., Garhwal, Sutlej Valley) simultaneously display high vegetation seasonality and relatively low seasonality of rainfall. Persistent winter rainfall, rare in Nepal and Bhutan, therefore has the potential to cause a greater impact on the landscape when vegetation density is especially low. Although the number of extreme events are typically lower in the NW Himalaya, storms that do occur or penetrate far into the region can have a larger impact. Without the stabilizing effect of dense vegetation cover, rainfall in these sparsely vegetated regions is able to mobilize and evacuate significantly more sediment (*Wulf et al.*, 2010; 2012) than in more vegetated regions. This results in highly variable denudation rates that are likely driven by climatic events (e.g., storms) rather than reflecting tectonic uplift rates (cf., *Bookagen*, submitted to Geology). This may also explain the poor correlation between denudation rates and tectonically-influenced topographic metrics in the Sutlej Valley.

4.5.2 A change in denudation rates or erosive agents?

In high-relief, tectonically active orogens, such as the Himalaya, landsliding and other mass movements are expected to play a critical, and perhaps dominant, role in erosion of the landscape (e.g., *Burbank et al.*, 1996b; *Bookhagen et al.*, 2005a). Modeling studies have suggested that vegetated landscapes may be more likely to be dominated by landsliding, whereas bare landscapes are typically dominated by runoff-erosion (*Collins et al.*, 2004; *Istanbulluoglu et al.*, 2004; *Istanbulluoglu and Bras*, 2005). Based on these assumptions, we might expect landsliding to be a more dominant erosional

process in more densely vegetated regions of the Himalaya than in the sparsely vegetated regions. Recent studies of ^{10}Be TCN denudation rates have highlighted the potential sampling bias in detrital samples (*McPhillips et al.*, 2014; *Puchol et al.*, 2014; *Olen et al.*, 2015). Specifically it has been shown that the typical clast size used to calculate catchment-mean denudation rates with ^{10}Be (typically between 250 μm and 500 μm) may not be sensitive to landslide denudation rates. McPhillips et al. (2014) analyzed single cobble-sized clasts analysis as a record of landslide erosion rates and argue that the erosion signal of landsliding is absent in multi-grain analysis of sand-sized grains. It is therefore possible that denudation from landsliding is missing in our along-strike compilation of ^{10}Be denudation rates. Such a change in erosional processes could result in ^{10}Be TCN concentrations more accurately recording denudation rates in less vegetated regions of the orogen, and an apparent trend in denudation rates (especially high denudation rate) may in fact be an artifact created by the sensitivity of ^{10}Be concentrations to different erosional processes. This could also explain why denudation rates derived from ^{10}Be TCN in the densely vegetated Lesser Himalaya appear decoupled from long-term denudation rates along strike. If landslide-driven denudation rates are not recorded or are under-represented in the standard grain size used for sample analysis, we could lose our ability to detect a potential along-strike gradient in denudation rates in densely vegetated regions. Our current dataset cannot differentiate these possible factors. Further work mapping the spatial extent and temporal frequency of landslides, as well as estimates of denudation rates independent of ^{10}Be TCN or including a wider array of grain sizes, will need to be done to explore this possible complication.

4.6 Conclusions

Our study of denudation rate measurements from fluvial catchments along strike of the Himalayan orogen highlights the importance of climate and vegetation in influencing both the rates and variability of denudation. First, in contrast to recent studies that have argued for a strong link between denudation rates and tectonic drivers across strike of the Himalaya (*Godard et al.*, 2014; *Scherler et al.*, 2014; *Le Roux-Mallouf et al.*, 2015; *Morell et al.*, 2015), along-strike centennial to millennial denudation rates are decoupled from long-term

tectonic exhumation rates obtained from thermochronometric inversion (*Thiede and Ehlers*, 2013), particularly in the Lesser Himalaya. Second, we observe a strong link between the pattern of denudation rates and climatic factors, such as rainfall and vegetation, along strike. Importantly, denudation rate variability is strongly correlated to the vegetation seasonality (R=0.99). Third, we document that vegetation modulates the relationship between denudation rates and topography in a highly active and dynamic orogen. The degree of linearity between denudation rate and topographic metrics (e.g., hillslope gradient, SSP, k_{sn}) increases as mean annual rainfall and vegetation density increase. The result is a more linear response of topography and topographic steepness to changes in denudation rates in wet, densely vegetated environments, as opposed to a highly nonlinear response in dry, sparsely vegetated environments. However, we note that ^{10}Be TCN samples may not accurately record landslide-driven denudation rates (e.g., *Puchol et al.*, 2014) and the observed patterns of denudation rates may be a reflection of a change in erosive processes as erosion driven by surface-runoff in sparsely vegetated environments transitions into landslide-dominated erosion in densely vegetated regions. Overall, our study highlights the importance of vegetation in understanding the relationship between denudation rates and regional climate and tectonics, even in a tectonically active and highly dynamic orogen such as the Himalaya. Further studies of how vegetation affects denudation and topography in different tectonic settings will greatly increase our understanding of how these important surface processes interact globally.

Acknowledgements

This project was funded by the graduate school GRK1364 of the German Science Foundation (DFG, Deutsche Forschungsgemeinschaft; Project GRK 1364/2). We thank Veronica Torres Acosta for helpful discussions.

Chapter 5: Ecologic, climatic and geomorphic drivers of terrestrial organic matter transport in the trans-Himalayan Arun River catchment, E Nepal

Abstract

Fixation of atmospheric CO_2 in terrestrial vegetation, subsequent export and deposition of terrestrial plant organic matter (tOM) in marine sediments is an important component of the global carbon cycle, yet it is difficult to quantify. This is partly due to the lack of understanding of relevant processes and mechanisms responsible for tOM transport throughout a landscape. Here we present a new approach to identify tOM source areas, quantify contributions and ascertain the role of ecologic, climatic and geomorphic drivers controlling tOM export in the eastern Nepalese Arun River catchment spanning the world's largest elevation gradient from 205 to 8,848 m asl. Our approach takes advantage of the distinct stable hydrogen isotopic composition (expressed as δD values) of plant wax *n*-alkanes produced along this gradient, transported in river waters and deposited in riverbanks alongside the Arun and its tributaries. Informed by remote sensing data, we applied four differently weighted isotopic mixing models to identify and quantify sourcing of tributary plant-derived tOM along the Arun. The weighting parameters included catchment area, vegetation cover and annual rainfall amounts combined with normalized channel steepness (k_{sn}) as a proxy for erosion. We find that catchment area, landscape steepness and vegetation cover weighting alone could not explain actual field observations. When including annual rainfall amount and vegetation cover weighted by k_{sn} as a measure of erosion, isotopic mixing models captured the observed δD value pattern along the Arun. In riverbank sediments of the Arun mainstem, we found that plant wax *n*-alkanes were mostly derived from the lower elevations constituting only a small fraction (15%) of the catchment. We conclude that regions with dense vegetation, high precipitation and high erosion rates dominate tOM export from the studied Himalayan landscape.

5.1 Introduction

Fixation of atmospheric carbon in terrestrial organic matter (tOM) and subsequent export into marine basins is one of the key mechanisms responsible for long term carbon burial with a direct impact on global atmospheric CO_2 levels (*Berner*, 1990; *Burdige*, 2005). In the Neogene Ganges-Brahmaputra river system the transfer of C, fixed in tOM, has been suggested to be more important than the weathering of silicate rocks, long thought to be the primary mechanism for atmospheric CO_2 drawdown (*France-Lanord and Derry*, 1997). Whereas total tOM fluxes to marine sinks have previously been estimated using a variety of different methods (*France-Lanord and Derry*, 1994; *Galy et al.*, 2015, 2011; *Goñi et al.*, 1997; *Hedges et al.*, 1986, 1994; *Weijers et al.*, 2009), other studies go further to understand the sourcing of tOM within large river catchments (*Bouchez et al.*, 2014; *Galy et al.*, 2011; *Goñi et al.*, 2000; *Hedges et al.*, 2000; *Kim et al.*, 2012; *Ponton et al.*, 2014; *Tao et al.*, 2015). Erosion has been suggested to be the dominant control of tOM transport from such catchments globally (Galy et al. 2015), but little information exist on the interplay of climatic and geomorphic drivers within individual catchments. The identification of important tOM source regions and in particular climatic and geomorphic controls on tOM transport processes will allow for a better understanding of the sensitivity of particular landscapes to disturbances with consequences for the global carbon cycle.

Plant wax lipid biomarkers and their stable isotopic composition (expressed as δD or $\delta^{13}C$ value) are an established tool to reconstruct paleoclimatic changes from sedimentary archives (e.g. *Freeman and Colarusso*, 2001; *Schefuß*, 2003; *Tierney et al.*, 2008). They are emerging in applications tracing tOM within rivers draining catchments with strong topographic gradients, because their δD values encode signals of elevation (*Galy et al.*, 2011; *Ponton et al.*, 2014). While plant wax biomarkers make up only a small fraction of tOM, their resilience makes them a persistent tracer for ultimately plant-derived material, whose sources include living (i.e., leaves) and dead plants (i.e., litter) as well as soils. For brevity we refer to this pool of terrestrial organic matter as tOM. Our approach implicitly assumes that the sourcing of tOM follows that of plant waxes; however, we acknowledge that tOM is heterogeneous, with associated differential sourcing, preservation and transport. Nevertheless, studies employing plant waxes in fluvial catchments have revealed novel insights into tOM transport

processes: Galy et al. (2011) for example used δD values of plant waxes extracted from riverine fine particulate organic matter as a diagnostic tracer for the sourcing of tOM within the Ganges-Brahmaputra watershed. At the mouth of the Ganges-Brahmaputra, they found tOM from the Indian plains overprinted the signal of tOM emanating from the Himalaya. With more detailed progressive downstream sampling within the Madre de Dios River system in the Peruvian Andes, Ponton et al. (2014) similarly reported plant wax δD values of riverine fine particulate organic matter. While they inferred that this material is representative of its respective catchment, they found a seasonal offset equivalent to ~1km higher sourcing in the wet season, associated with more Andean erosion.

While physical erosion has been suggested to be the main driver of tOM transport in large river systems worldwide (*Galy et al.*, 2015), no study has yet attempted to quantify the relative importance of vegetation cover, climate and erosional processes within heterogeneous catchments. In this study, we assess catchment wide plant-derived tOM contributions of tributaries to the trans-Himalayan Arun River (33,508 km²), covering a steep altitudinal (Figure 5.1a) and climatic (Figure 5.1b) gradient (cf., *Bookhagen and Burbank*, 2006; *Olen et al.*, 2015). Whereas the lower catchment is characterized by tropical to subtropical evergreen forests, sparse alpine vegetation consisting of grasses and shrubs dominates the higher Himalaya and the Tibetan Plateau (Figure 5.1c) (*Carpenter and Zomer*, 1996; *Dobremez and Shakya*, 1975). We take advantage of the systematic change of precipitation δD values (*Dansgaard*, 1964; *Gonfiantini et al.*, 2001) and plant wax δD (*Ernst et al.*, 2013; *Jia et al.*, 2008; *Kahmen et al.*, 2013a; *Peterse et al.*, 2009; *Sachse et al.*, 2006; *Tipple and Pagani*, 2012) along altitudinal and hydrological gradients, and make use of it to characterize plant wax δD values along the Arun valley. Together with these observations we employ remote sensing techniques to estimate sourcing of plant wax *n*-alkane contributions from across the catchment and identify ecological, climatic, and geomorphic drivers responsible for tOM export from the tributaries.

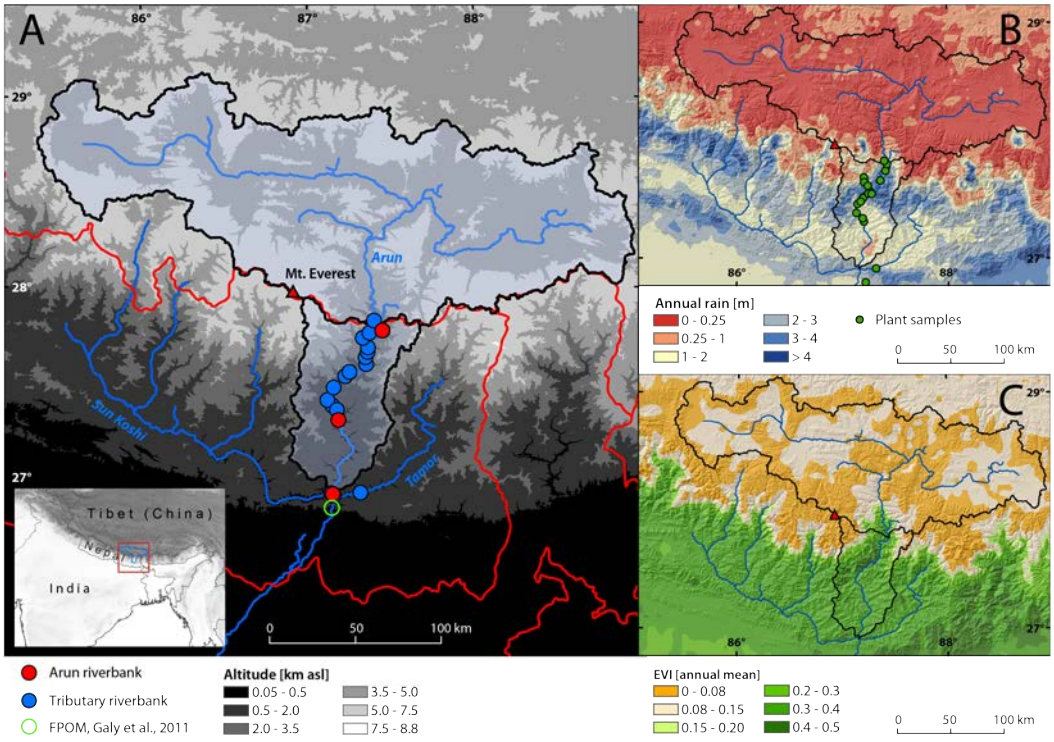

Figure 5.1 Study area characteristics

(A) Topographic map delineating two nested Arun catchments (black lines) above the lowermost and the uppermost mainstem riverbank samples (red circles). Riverbank sample sites are denoted by blue circles, fine particulate organic matter sampling site by Galy and Eglinton (2011) is shown as light green circle. (B) Mean annual rainfall based on calibrated TRMM satellite data (Bookhagen and Burbank, 2010) together with modern plant sampling locations (dark green circles). (C) Mean annual Enhanced Vegetation Index (Huete et al., 1994; Justice et al., 1998) showing denser vegetation towards lower elevations.

5.2 Geographic setting

The Arun River drains the southern Tibetan Plateau and flows through the eastern Nepalese Himalaya before confluences in the Siwalik Hills with the Tamor and Sun Koshi Rivers to form the Sapta Kosi (Figure 5.1a). The altitudinal range of the catchment extends from 8848 m asl at the summit of Mount Everest to 203 m asl at its outlet into the Sapta Kosi over a horizontal distance of less than 160 km. Downstream, the Sapta Kosi continues ultimately into the Bay of Bengal via the Ganges-Brahmatputra River system.

The climate of Eastern Nepal is dominated by the Indian Summer Monsoon (ISM) contributing ~70% of the annual rain during its peak season between June and September (*Bookhagen and Burbank*, 2010). The Siwaliks in the south and the main Himalaya range, including Mount Everest and Makalu, act as orographic barriers to the ISM (Figure 5.1b, 5.2) (*Bookhagen and Burbank*, 2006). The Tibetan region of the Arun receives very small amounts of rainfall, but

additional snow from winter westerly disturbances originating from the Caspian, Black and Mediterranean Seas (*Bookhagen and Burbank*, 2010; *Lang and Barros*, 2004).

Vegetation in the lower Arun Valley is characterized by near-tropical dipterocarp monsoon forest (< 1000m) with large stands of *Shorea robusta* in its upper part. Subtropical forests (1000-2000m) are dominated by *Schima Wallichii* and *Castanopsis spp*. Temperate forests further up the valley (2000-3000m) are characterized by a mix of evergreen (*Quercus, Persea, Rhododendron*) and deciduous (*Acer, Prunus*) taxa. Fir, birch and *Rhododendron* stands dominate mountainous alpine forests until the treeline at ~4000m (*Carpenter and Zomer*, 1996; *Dobremez and Shakya*, 1975). The area until 500m above the treeline is characterized by alpine woody scrubs dominated by *Rhododendron spp.* followed further up by alpine meadow and subnival plant communities (*Carpenter and Zomer*, 1996).

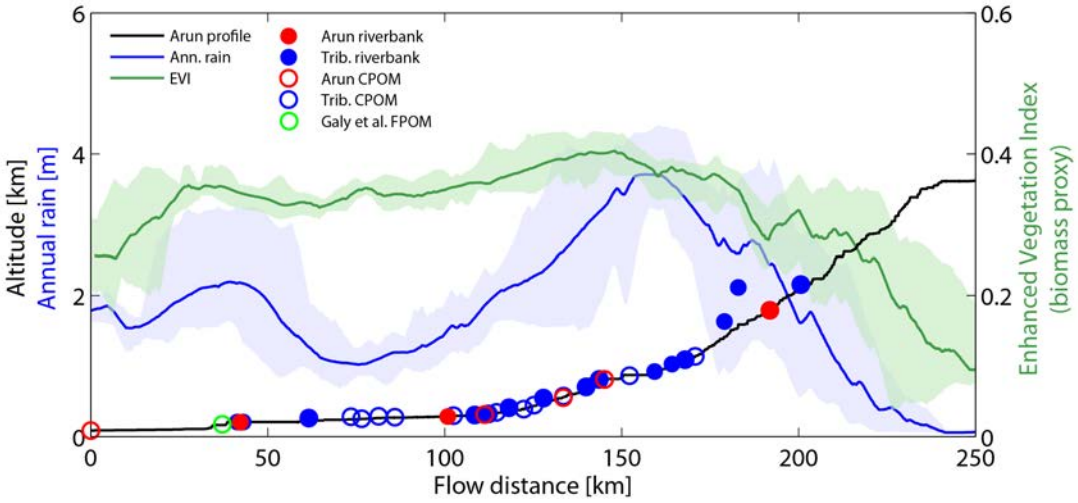

Figure 5.2 Arun River profile

Longitudinal river profile of the Arun River from the Ganges Plain to the Tibetan Plateau (black) with sample sites along the river. Enhanced vegetation index (green; Huete et al., 1994; Justice et al., 1998) and mean annual rainfall rates (blue; Bookhagen and Burbank, 2010); for each dataset we show the mean (line) and minimum and maximum range (shading) from values within a 50-km wide swath along the Arun River's N-S path.

5.3 Methods

5.3.1 Sampling

Samples were obtained during two sampling campaigns in September 2011 and October/November 2012 (indicated by first two digits of sample ID). River water was sampled at 37 locations (8 mainstem and 29 tributaries; Table 5.1). Water samples were taken to accompany each of the sediment and CPOM samples. They were stored in gas-tight 2 ml glass vials that were flushed before being filled.

Leaves of modern trees and shrubs were sampled at 17 locations along the Arun Valley, at elevations ranging from 87 to 4070 m asl. We attempted to sample same C_3 plant species present throughout the catchment as much as possible and focused on *Shorea robusta*, a dry-season deciduous or evergreen tree, depending on water availability, the evergreen tree *Schima wallichii* and mostly evergreen *Rhododendron spp.* (cf. Table S5.1). At each site three individual plants from one to three of the dominant tree species were sampled, in total 113 individual plants. For each tree, 5-20 mature leaves were randomly sampled from approximately 2 m height, then stored and dried in paper bags.

Riverbank sediments were sampled from narrow overbank deposits (within ~1 m of elevation of the river) of the Arun River and its tributaries collecting ~300 g of fine-grained sediments. These samples represent deposits from most recent ISM flooding, which occurred 1-2 months prior to sampling. The northernmost Arun mainstem riverbank deposit sample was taken at 27.8°N at an altitude of 1793 m asl representing input from the Tibetan Plateau. The southernmost mainstem sample was taken approximately 1 km north of the confluence with the Tamor and Sun Koshi Rivers at 26.9°N (205 m asl), thus integrating over both Tibetan and Himalayan drainage areas (Figure 5.1a and 5.2). One intermediate mainstem sample was taken at 27.3°N, and 285 m asl. Riverbank deposits of major tributaries, defined as bankfull channels > ~8 m, were sampled when accessible, yielding a total of 16 sampled tributaries, including two Tamor and one Sun Koshi samples.

Suspended material floating in the river was sampled with a net (mesh-size 1 mm). This material was mostly composed of macroscopic plant debris and we

therefore refer to it as coarse particular organic matter (CPOM). CPOM samples were collected at 6 mainstem locations and from 20 tributaries (Figure 5.1a, 5. 2).

5.3.2 Laboratory Methods

5.3.2.1 Water isotope analysis

$\delta^{18}O$ and δD values of river water were determined by laser spectroscopy using a Liquid Water Isotope Analyzer (Los Gatos Research, Mountain View, California, USA), at the Institute of Earth and Environmental Sciences, University of Potsdam. Before analysis, samples were filtered through 0.45 µm polyethylene filters. Three standards were interspersed between every five samples (Los Gatos Research water isotope standard). Out of 6 replicate sample injections, the first three runs were discarded and a mean of the last three measurements was used. To convert sample values to the Vienna Standard Mean Ocean Water (VSMOW)-Standard Light Antarctic Precipitation (SLAP) scale, we used the linear regression function describing the relation between measured and known isotope standard $\delta^{18}O$ and δD values. Precision is reported as one σ of replicate measurements of the standards, and is 0.06‰ and 1‰ for $\delta^{18}O$ and δD respectively.

5.3.2.2 Plant wax extraction and quantification

Riverbank sediments and CPOM samples were freeze-dried and a total lipid extract (TLE) of the homogenized sample was obtained by extracting the sample on a Dionex ASE 350 accelerated extraction system using 9:1 dichloromethane:methanol. Dried leaf samples were ground and a TLE was obtained using ultrasonic extraction with the same solvent mixture. The aliphatic fraction containing plant wax *n*-alkanes was obtained through solid phase extraction. For quantitative and qualitative analysis the purified samples were measured using an Agilent GC MSD (Agilent 5975C MSD, Agilent 7890A GC with Agilent J&W HP-5ms column, 30 m x 0.25m x 0.25 µm film) equipped with an additional FID (for a more detailed description of sample processing see *Hoffmann et al.*, 2013).

In order to characterize the samples *n*-alkane distribution, we calculated the average chain length (ACL) using the formula

$$ACL = \Sigma (C_n \cdot n)/\Sigma C_n, \quad (5.1)$$

where n is the number of carbon atoms from 25 to 33 and C_n is the relative abundance. The carbon preference index (CPI) was used to quantify odd over even chain length predominance:

$$CPI = 0.5 \cdot (\Sigma_{odd} C_{25-31} + \Sigma_{odd} C_{27-33})/\Sigma_{even} C_{26-32} \quad (5.2)$$

5.3.2.3 Plant wax isotope analysis

δD values of riverbank, CPOM and tree derived *n*-alkanes from the 2012 field campaign were measured at the Institute of Earth and Environmental Sciences at the University of Potsdam. Samples taken in 2011 were measured at University of Southern California. A Thermo Delta V Plus IRMS coupled to a Thermo Trace 1310 GC (Agilent DB-5 column, 30 m × 0.25 mm × 0.25 µm film) via a Thermo GC Isolink pyrolysis furnace operated at 1420° C was used at Potsdam University. At the Department of Earth Sciences, USC, a Thermo Scientific Trace gas chromatograph equipped with a ZB-5ms column (30 m × 0.25 mm × 1µm) was coupled to a Thermo Delta V Plus via an Isolink operated at 1420 °C.

Measured values were normalized to the VSMOW-SLAP scale using an external standard containing C_{16} to C_{30} *n*-alkanes (A-Mix, A. Schimmelmann, Indiana University, Bloomington), run in triplicates after every 6th sample. The overall analytical accuracy of triplicate standard analysis was determined to be 3.2‰ (root mean square 0.9‰, n = 81). The H_3^+ factor was measured daily and mean values were in the range of 2.99 to 3.37‰ (average = 3.13‰, σ = 0.11‰). δD values are reported as the mean and 1 σ of triplicate measurements.

5.3.3 Remote sensing topography and climate analyses

Catchment extent and median elevation was determined using a 90-m ground resolution SRTM digital elevation model (*USGS*, 2006) processed with standard Geographic Information System tools (*Schwanghart and Kuhn*, 2010). The distribution of annual rainfall amounts was averaged based on calibrated

Tropical Rainfall Measurement Mission (TRMM) satellite data product 3B42 from 1998 to 2010 (*Bookhagen and Burbank*, 2010); TRMM3B42 data have a 3-hour temporal resolution and a 0.25° (~30 km) spatial resolution (Huffman et al., 2007). The Moderate Resolution Imaging Spectroradiometer (MODIS) data product MOD13C1 includes the Enhanced Vegetation Index (EVI), a spectral measure of photosynthetic activity (*Huete et al.*, 1994; *Justice et al.*, 1998), which we used to approximate biomass on the landsurface. It comprises 16-day composites of remotely sensed EVI raster data with a spatial resolution of 0.05° (~5 km). We also used MODIS annual mean daytime temperature (MOD11C2, Wan and Dozier (1996)) with the same spatial resolution that is based on 8-day composites. Presented MODIS annual averages are based on 12-years of data (2001-2012). In order to characterize stream catchments, raster data were resampled using a bilinear algorithm to match the DEM spatial resolution.

In order to characterize the spatial distribution of erosion throughout the landscape we calculated two topographic metrics for every DEM-pixel in the channel network: The normalized steepness index (k_{sn}) (1) using drainage area as discharge approximation (*Wobus et al.*, 2006) and (2) using a rainfall-weighted flow accumulation grid to account for the impact of spatially-inhomogeneous rainfall (*Bookhagen and Burbank*, 2010; *Bookhagen and Strecker*, 2012; *Olen et al.*, 2015). For both, the local channel gradient was calculated for each pixel with a moving average of 11 pixels (~1000m), and then divided by (1) upstream area or (2) rainfall-weighted flow accumulation, respectively, to calculate channel steepness (k_s). Subsequently, both grids were normalized by:

$$k_{sn} = k_s \cdot A^{-\theta}, \tag{5.3}$$

where the standard reference concavity of θ is 0.45 (e.g., *Whipple*, 2004; *Wobus et al.*, 2006).

5.4 Results

5.4.1 Surface water δD values

Tributaries sampled from 205 to 2156 m asl (median catchment elevations 761 to 4124 m asl) had δD_{water} values between -45.9 and -92.5‰ (Figure 5.3a).

The relationship between median catchment elevation and tributary δD_{water} values yielded a slope of -8.3‰ km^{-1} ($R = -0.73$, p-value < 0.01). The mainstem Arun River had lower δD_{water} values of -78, -88 and -110‰ from south to north, respectively, as expected due to higher median catchment elevation (4785, 4832 and 4878 m asl, respectively).

5.4.2 Plant wax molecular composition

We identified *n*-alkanes in all plant leaf samples, ranging from 25 to 33 carbon atoms, i.e. chain length, with nC_{29} and nC_{31} being dominant (Table S5.1). The ACL ranged from 26.9 to 31.6 (mean = 29.1, $\sigma = 1.0$, n = 113). CPI values ranged from 0.9 to 22.7 (mean = 6.7, $\sigma = 6$, n = 113). Neither plant leaf ACL nor CPI showed a significant relationship with sample site elevation, annual rainfall amount or EVI.

Riverbank and CPOM samples contained plant wax *n*-alkane distributions that reflect those of plants in the catchment, dominated by nC_{31} and nC_{29} and to a lesser extent nC_{27} (Table S5.2). We do not report absolute abundances as quantification was not deemed representative because of sorting of river sediments.

Average chain length of *n*-alkanes extracted from riverbank sediments (ACL_{bank}) ranged from 27.4 to 30.3 (mean 29.3, $\sigma = 0.6$, n = 17) for tributaries and 28.8 to 30.4 (mean 29.6, $\sigma = 0.5$, n = 3) for the mainstem (Table S5.2). ACL_{CPOM} varied between 28.4 and 31.3 (mean 29.8, $\sigma = 0.8$, n = 20) for tributaries, and 28.4 to 29.5 (mean 28.9, $\sigma = 0.4$, n = 6) for the mainstem.

CPI of riverbank samples ranged from 1.3 to 14.1 for tributaries and 1.3 to 9.1 for the mainstem (Table S5.2). CPI of CPOM ranged from 2.0 to 12.4 for tributaries and from 6.0 to 14.7 in the mainstem. Neither ACL nor CPI of riverbank and CPOM samples were correlated to catchment median elevation, precipitation or temperature.

5.4.3 Plant wax *n*-alkane δD values

Plant wax δD values of living plants (δD_{leaf}) ranged from -78‰ (sample 11004-lc1, nC_{29}, *Shorea robusta*) to -242‰ (sample 11047-lc3, nC_{31}, *Engelhardtia spicata L.*). The mean nC_{29} δD_{leaf} value was -168‰ ($\sigma = 30$‰, n = 113). Due to

strong variability nC_{29} δD_{leaf} values showed only weak correlation with sample site elevation (R = -22, p = 0.02) with a slope of -5.5‰ km^{-1} (Figure 5.3b).

We measured the hydrogen isotopic composition of the C_{29} *n*-alkane in all riverbank (δD_{bank}) and CPOM (δD_{CPOM}) samples. In 42 samples chain length distributions were sufficient to measure additional compounds. We found nC_{29} to be correlated with nC_{27} (R = 0.72, p < 0.01), nC_{31} (R = 0.69, p < 0.01) and nC_{33} δD values (R = 0.72, p < 0.01). We focus on nC_{29} δD values in the subsequent data analysis (see Table S5.2 for complete dataset). No significant interannual difference was observed between riverbank tributary nC_{29} δD values ($\delta D_{bank,trib}$) of September 2011 (n = 6) and November 2012 (n = 7) tributary samples (Wilcoxon-Mann-Whitney-Test rejected, p = 0.16). Therefore, we combined the two riverbank datasets for further analysis. $\delta D_{bank,trib}$ values ranged from -157‰ to -197‰ (n = 13), and were correlated to median catchment elevation with a slope of -5.7 ± 2.6‰ km^{-1} (R = -0.56, p < 0.05) (Figure 5.4a), the same as for living plants within uncertainties (Figure 5.3b).

2011 and 2012 CPOM data were combined as no significant difference between September 2011 (n=16) and November 2012 (n = 4) tributary CPOM nC_{29} δD values ($\delta D_{CPOM,trib}$) was observed (Wilcoxon-Mann-Whitney-Test rejected, p = 0.24). $\delta D_{CPOM,trib}$ values ranged from -145‰ to -217‰ (median = -182‰, n = 20), and were not correlated to median catchment elevation. Arun mainstem CPOM δD values ranged from -210‰ to -175‰ (n = 6), but like tributaries showed no trend with elevation. A comparison of tributary riverbank values with the isotopic composition of surface water (Figure 5.4b) yielded a significant linear relationship, with $\delta D_{bank} = (0.45 \pm 0.19)\ \delta D_{water}$ -147 ± 13‰ (R = 0.54, p = 0.03), but the relationship was not significant for CPOM samples (R = 0.24, p = 0.33).

The three Arun mainstem riverbank samples saw a downstream D-enrichment with δD_{bank} values (from -206‰ to -184‰). We calculated the isotopic enrichment between mainstem riverbank *n*-alkanes sampled at the highest (Tibetan Plateau, TP) and the lowest (Himalayan Range, HR) location ($\varepsilon_{HR/TP}$) to be +27‰ using the equation:

$$\varepsilon_{HR/TP} = ((\delta D_{bank\_TP}+10^3)/(\delta D_{bank\_HR}+10^3)-1)\cdot 10^3 \quad (5.4)$$

Table 5.1 Sample locations and isotope values

Sampling locations with stream water δD and $\delta^{18}O$ vales and the hydrogen isotopic composition of plant waxes extracted from river bank deposits and floating coarse particulate organic matter (CPOM) (cf. Table S5.2 for further details).

Site iD		Site Longitude (˚)	Site latitude (˚)	Catchment Area [km²]	water δD [‰]	water δD stdev [‰]
11029	Arun	87.19	27.51	30431	-99.3	0.4
11049	Arun	87.27	27.56	29958	-105.7	1.1
11069	Arun	87.16	27.38	31189	-96.1	0.4
11104	Arun	86.93	26.52	57927	-90.1	0.2
12009	Arun	87.28	27.57	29958	-88.7	0.3
12083	Arun	87.45	27.78	28416	-109.6	0.7
12142	Arun	87.19	27.31	31269	-88.3	0.2
12150	Arun	87.15	26.93	33508	-77.5	0.8
11005	trib.	87.18	27.37	11	-45.9	0.5
11008	trib.	87.15	27.39	12	-53.9	0.3
11010	trib.	87.13	27.39	75	-58.5	0.7
11013	trib.	87.12	27.41	206	-63	0.1
11018	trib.	87.14	27.45	351	-78.5	0.1
11020	trib.	87.15	27.47	3	-57.5	0.2
11023	trib.	87.16	27.48	12	-60	0.3
11028	trib.	87.19	27.51	13	-58.5	0.5
11037	trib.	87.23	27.54	218	-88.6	0.9
11043	trib.	87.25	27.57	188	-92.5	0.5
11075	trib.	87.18	27.32	40	-59.7	0.1
11080	trib.	87.24	27.22	314	-59.7	0.2
11081	trib.	87.26	27.18	35	-51.7	0.8
11085	trib.	87.28	27.15	91	-57.6	0.5
11086	trib.	87.25	27.12	84	-58.5	0.1
11090	Tamur	87.32	26.93	5885	-85.8	0.5
12005	trib.	87.31	27.56	82	-52.2	0.6
12026	trib.	87.35	27.61	165	-70.9	0.6
12032	trib.	87.35	27.64	9	-51.3	0.5
12035	trib.	87.36	27.67	80	-65.2	0.5
12043	trib.	87.36	27.69	471	-73.7	1.1
12054	trib.	87.33	27.74	29	-58.6	0.6
12063	trib.	87.37	27.77	0	-55.9	0.3
12082	trib.	87.45	27.78	95	-84.3	0.4
12097	trib.	87.4	27.83	8	-62.8	0.3
12149	Tamur	87.15	26.93	18144	-76.2	0.5
12151	Sun Kosi	87.16	26.91	6050	-69	1.4

Site iD	water δ18O [‰]	water δ18O stdev [‰]	Bank nC29 δD [‰]	Bank nC29 δD stdev [‰]	CPOM nC29 δD [‰]	CPOM nC29 δD stdev [‰]
11029	-13.66	0.05			-210	1.5
11049	-14.82	0.08			-184	0.3
11069	-13.44	0.15			-192	2.6
11104	-12.38	0.2			-175	0.5
12009	-12.23	0.02			-185	0.5
12083	-14.92	0.08	-206	2	-176	0.6
12142	-12.59	0.05	-185	3.1		
12150	-11.12	0.08	-184	1.3		
11005	-6.34	0.03	-157	1.5	-217	1.3
11008	-7.79	0.02	-174	0.6	-178	3.8
11010	-8.8	0.03			-143	3.8
11013	-9.29	0.03	-161	2.6	-178	0.6
11018	-11.23	0.01			-193	2
11020	-8.59	0.03			-183	3
11023	-9.29	0.04	-173	2.6	-192	0.6
11028	-8.68	0.04			-159	0.5
11037	-12.37	0.12	-174	1.6	-186	1
11043	-13.4	0.04	-181	5	-187	1.7
11075	-8.78	0.12			-171	1.2
11080	-8.83	0.03			-186	0.2
11081	-7.7	0.04			-181	0.4
11085	-8.73	0.06			-184	0.9
11086	-8.81	0.04			-175	3.6
11090	-12.31	0.1	-184	1.6	-202	1.8
12005	-8.41	0.06			-163	0.5
12026	-10.42	0.05	-197	0.8		
12032	-7.82	0.01	-176	0.9		
12035	-9.3	0.14	-185	0.7	-184	0.7
12043	-10.97	0.15	-160	3.3	-180	0.6
12054	-8.94	0.1	-180	3.7		
12063	-8.73	0.07	-161	3.5		
12082	-12.32	0.01	-189	0.9		
12097	-9.04	0.02	-165	2.5	-171	0.4
12149	-10.93	0.04	-191	3.4		
12151	-10.06	0.14	-188	1.3		

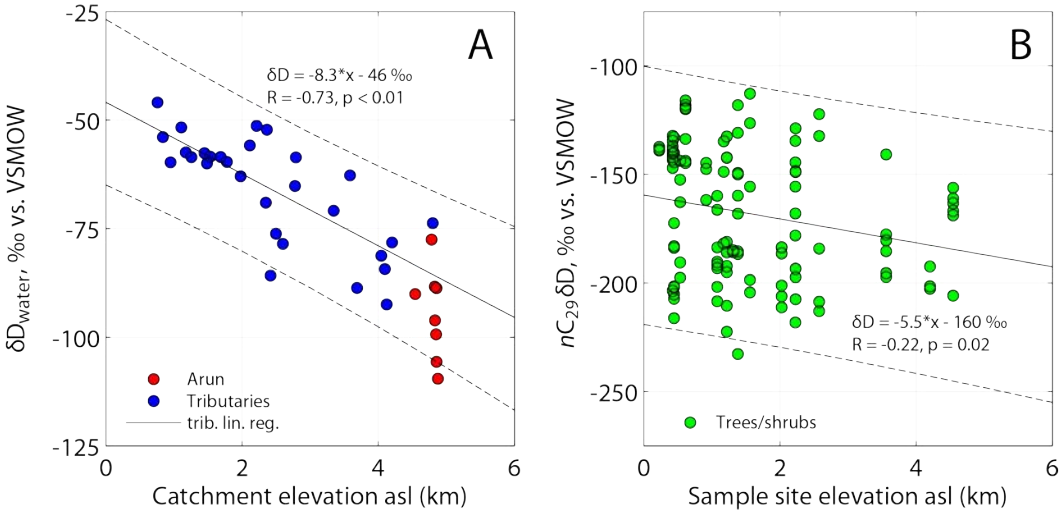

Figure 5.3 Isotopic gradients with elevation.

(A) Surface water δD values vs. median catchment elevation. (B) Plant wax nC_{29} δD values of modern tree samples (each data point is an individual, mixed species) along the elevation gradient. Both plots show linear regression (line) and 95% confidence intervals (dashed lines).

5.4.4 Remote sensing data

TRMM 3B42 satellite rainfall data indicate that only 34.7% of the Arun's annual rainfall occurs in the upper 84.8% of the catchment (north of the Nepal-China border) whereas, the majority, 65.3% is received in the lower 15.2% (between the border and the Arun/Tamor/Sun Koshi confluence). Rainfall peaks at the southern front of the Siwalik Hills (up to 4 m a^{-1}) and the main Himalayan range (locally > 5 m a^{-1}), in between locally dropping to less than 1 m a^{-1}. MODIS-derived annual mean EVI values follow the rainfall distribution: They increase at the southern front of the Siwalik Hills and remain constant until the southern front of the main Himalayan ranges, beyond which EVI drops on the TP as rainfall decreases (Figure 5.1c, 2).

5.5 Discussion

5.5.1 Elevation gradients in precipitation and stream water isotopic composition

A negative correlation between precipitation isotopes and elevation is expected based on the altitude effect (*Dansgaard*, 1964). For the stream waters of the Arun's tributaries, we found a gradient of -8.3‰ km^{-1} (using catchment

median elevation, σ = 1.6‰ km^{-1}) and of -8.8‰ km^{-1} (using mean elevation, σ = 1.5‰ km^{-1}), which is within the observed range of gradients of precipitation δD values with elevation in the tropics worldwide (*Gonfiantini et al.*, 2001). It is also comparable to gradients found for other rivers at the southern Tibetan Plateau margin. Re-evaluating δD_{water} values and mean catchment elevation reported by Hren et al. (2009) from the Lower Yarlung Tsangpo, Po Tsangpo and Siang Tsangpo Basins in the eastern Himalaya, we found slopes of -6.2, -5.7 and -4.3‰ km^{-1} with σ being 5.1, 7.0 and 2.7‰ km^{-1}, respectively (n = 17, 21, 16, R = -0.3, -0.2, -0.4). Garzione et al. (2000) compared sampling elevation of 18 streams, tributaries to the Kali Gandaki River, central Nepal. They found a slope of -21.8‰ km^{-1} across a large altitudinal range (380-4900 m asl), which is still within regressions of precipitation isotopic composition with elevation (*Gonfiantini et al.*, 2001). Re-evaluating the data from Garzione et al. (2000) within a restricted elevation range of 205-2156 m asl (equivalent to our study elevation range) yields a shallower slope of -13.1‰ km^{-1} (σ = 3.1‰ km^{-1}, R = -0.83, n = 10), comparable to our gradient (for mean catchment elevation) within 95% confidence intervals. The measured stream water isotopic lapse rate in this study represents our best estimate of the D-depletion of precipitation with increasing altitude in the Arun valley, and is consistent with regional observations.

5.5.2 Plant wax δD values in Arun tributaries

We find the largest variability in modern plants, when comparing the range of isotopic compositions (90^{th} percentile - 10^{th} percentile) in measured samples from living plants (83‰), CPOM (44‰) and riverbanks (35‰) (Figure 5.5). Similar patterns have been observed when comparing modern catchment vegetation with lake sediments elsewhere (*Hou et al.*, 2007; *Sachse et al.*, 2006). Despite the high variability between individuals and species, we find the same isotopic gradient for modern plants (-5.5‰ km^{-1}) and riverbank sediments in tributaries (-5.3‰ km^{-1}). This suggests that tributary riverbank deposits represent an integrated sample of plant waxes from their catchments, and is consistent with the findings of Ponton et al. (2014) based on tOM samples from the Peruvian Andes.

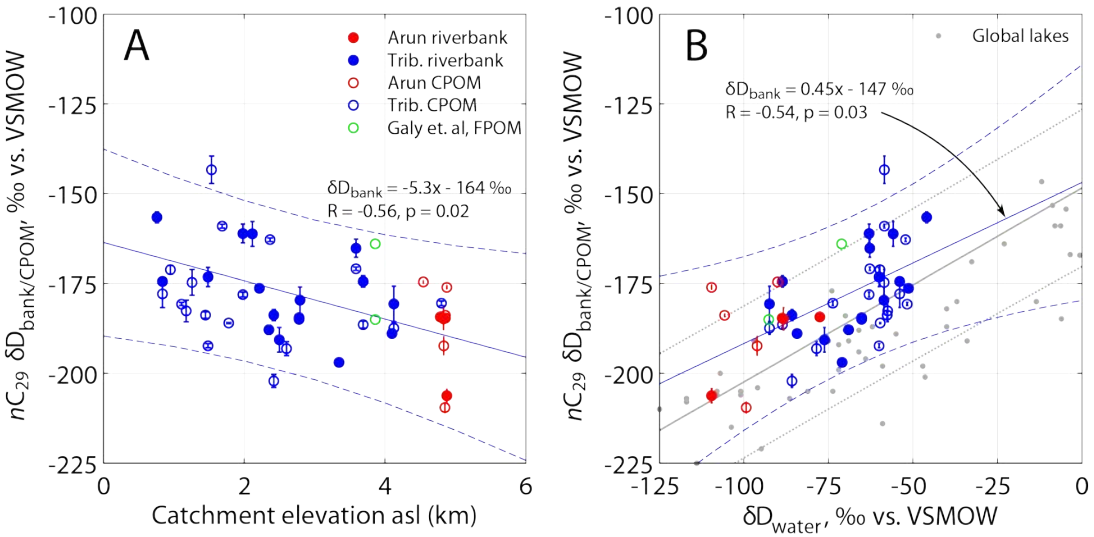

Figure 5.4 Isotopic composition of plant waxes in sedimentary samples.

(A) Shown versus elevation, including riverbank and CPOM samples (this study) and FPOM (Galy et al., 2011). Linear regression for tributary (riverbank and CPOM) values only (blue line), with 95% confidence intervals (dashed line). (B) As in part (A) but shown versus δD_{water} values. Also showing for comparison data for lake sediments versus mean annual precipitation isotopic composition (grey dots) (Garcin et al., 2012; Polissar and Freeman, 2010; Sachse et al., 2004) with regression (δD_{bank} = 0.55*δD_{rain} + 148‰, grey line).

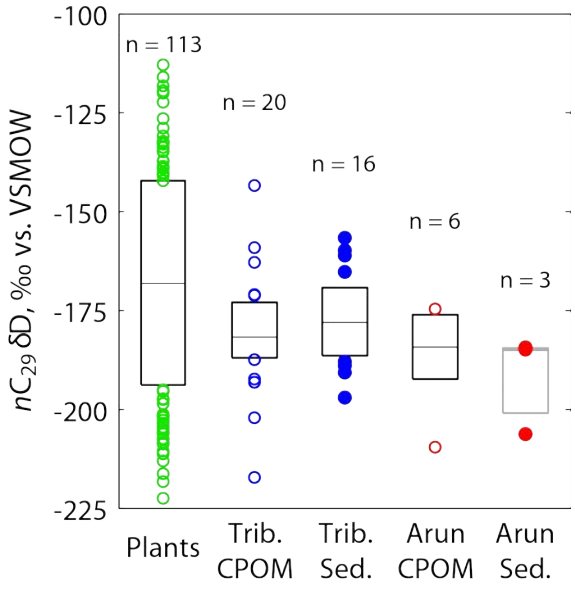

Figure 5.5 nC_{29} δD values

Box plots showing nC_{29} δD values of living plants, tributary CPOM and riverbank sediments, as well as Arun CPOM and riverbank sediments. Box denotes 25th and 75th percentile range, also showing median (line) and outliers (circles).

While bank deposition mostly occurs during the ISM, material mobilized upstream likely integrates over years or decades as plant detritus accumulates as leaf litter and in soils prior to transport and deposition. Galy and Eglinton (2011) determined fine particulate organic matter plant wax nC_{24} alkanoic acids from the Sapta Koshi watershed in the peak ISM season to be 0.05kyr old (cal. ^{14}C age), indicating a negligible fraction of fossil plant waxes and implying the representative status of sampled riverbanks for recent vegetation. In addition, the nC_{30} alkanoic acid δD value (-177‰) of the of the same sample (*Galy et al.*, 2011) was within the range of our CPOM and riverbank nC_{29} alkane δD values sampled ~10 km further south

and north, respectively (-175‰ and -184‰). This similarity between fine particulate organic matter and riverbank and between compound classes allows us to link the two studies, providing confidence in the findings of each and allowing us to infer that waxes in riverbank sediments likely incorporate waxes spanning at least decadal temporal scales.

CPOM, consisting of macroscopic, undegraded plant debris, showed δD values with reduced variability compared to δD_{leaf} indicating integration across a greater number of individual plants and species across the catchment. However, tributary CPOM δD values ($\delta D_{CPOM,trib}$) showed no significant correlation with δD_{water} values, implying that the catchment is not evenly represented. It is for example conceivable that CPOM was biased towards a few individual plants (e.g., uprooted trees). The stronger D-depletion of median $\delta D_{CPOM,trib}$ (-182‰) and $\delta D_{bank,trib}$ values (-174‰) in comparison with median δD_{leaf} values (-164‰) (Figure 4) likely reflects plant material contribution from higher elevated parts of the catchment to CPOM and riverbank sediment samples.

5.5.3 Fluvial integration of plant waxes

Mainstem riverbank samples were characterized by a downstream increase of δD_{bank} values (Figure 7b) due to inflow from lower elevation tributaries. Inputs are expected to be a function of catchment characteristics, including vegetation biomass and erosion rates. Since climate, plant cover, and erosion vary along the steep Himalayan passage of the Arun, tOM is not expected to evenly integrate across the entire catchment as it has been shown for tributaries (this study and *Ponton et al.*, 2014). Here we introduce a new quantitative modelling approach to identify the geomorphic and climatic controls on tOM sourcing.

5.5.3.1 Estimating δD_{bank} values for all Himalayan tributaries of the Arun River

We sampled 16 accessible tributaries between 205 and 1793 m river elevation and report measured $\delta D_{bank,trib}$ values (Table 5.1, Figure 5.7a). We then used the observed relationship between $\delta D_{bank,trib}$ values and median catchment elevation ($R = -0.56$, $p = 0.02$, Figure 5.4a) to predict $\delta D_{bank,trib}$ values for every pixel *k* (90x90m²) within the Arun watershed, using:

$$\delta D_{bank,trib}(k) = -5.31 \cdot alt(k) - 164‰, \quad (5.5)$$

where $\delta D_{bank,trib}(k)$ is the hydrogen isotopic composition of plant waxes produced at any pixel k based on the pixel's altitude alt(k) in km. As the Tamor and Sun Koshi catchments are >5000 km² we regard them as separate rivers rather than tributaries and excluded them for the regression, hence n = 13. We found modelled $\delta D_{bank,trib}$ not significantly correlated to observed $\delta D_{bank,trib}$ (R = 0.47, p = 0.07, Figure 5.6). Therefore, we tested a second multi-parameter approach that indirectly accounts for climatic and plant physiological drivers that affect δD_{leaf} values. We account for plant source water δD values by including mean annual temperature (MAT) and elevation (*Dansgaard*, 1964; *Garzione et al.*, 2000; *Rowley et al.*, 2001) and for evapotranspiration by including temperature and annual rainfall rates (MAP) (*Feakins and Sessions*, 2010; *Kahmen et al.*, 2013a, 2013b). As such, we set up a system of linear equations, where sampled tributary $\delta D_{bank,trib}$ values are described as a function of elevation, annual rainfall rates and temperature:

$$\begin{aligned}
\delta D_{bank,trib,1} &= x_1\, alt_1 + x_2\, Rain_1 + x_3\, T_1 + x_4 \\
\delta D_{bank,trib,2} &= x_1\, alt_2 + x_2\, Rain_2 + x_3\, T_2 + x_4 \\
&\dots \\
\delta D_{bank,trib,n} &= x_1\, alt_n + x_2\, Rain_n + x_3\, T_n + x_4 \quad (5.6)
\end{aligned}$$

where alt_n, $Rain_n$ and T_n represent remotely sensed median estimates of altitude, the MAP and MAT of sampled tributary catchments (n=16). The system of linear equations was numerically solved for 16 sampled tributaries leading to the solution $\boldsymbol{x}$ = (-0.0187 -2.4308 -0.0018 -94). The multi-parameter model derived estimates for $\delta D_{bank,trib}$ values showed a significant correlation to observed values (R = 0.73, p < 0.01) (Figure 5.6). Hence, we used this multi-parameter model to estimate tributary $\delta D_{bank,trib}$ values for further evaluation .

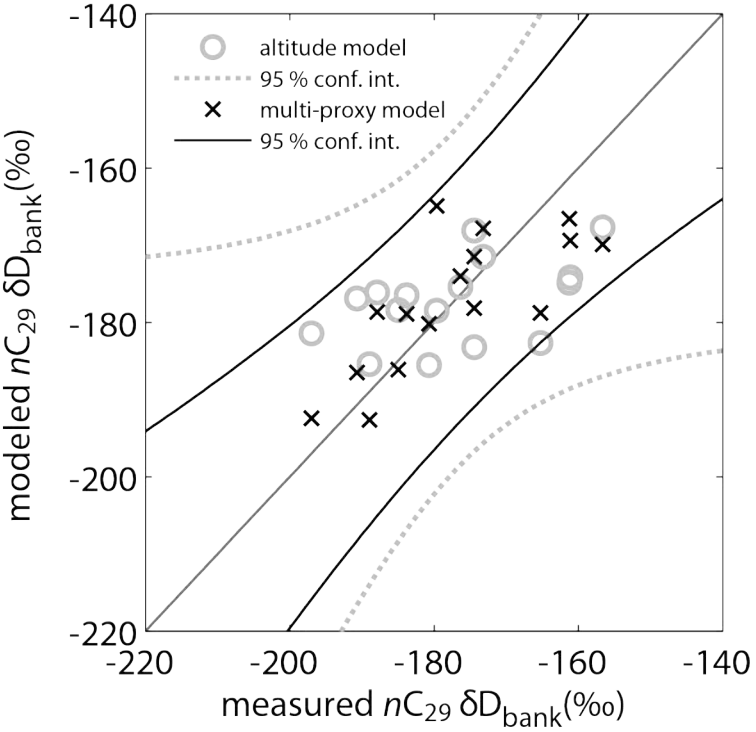

Figure 5.6 Measured versus modeled plant wax *n*-alkane δD

Measured versus modeled plant wax *n*-alkane δD values for tributary riverbank sediments. The linear model (open circles) depends on elevation only, whereas the multi-linear model (crosses) is based on tributary catchment median elevation, temperature and annual rainfall rates. Linear regression equals 1:1 line (grey line), as both δD values models are best fits to measured δD values. 95% confidence intervals shown for linear (grey dotted lines) and multi-linear (black lines) models.

5.5.3.2 Mixing models for sourcing within the Arun catchment

To constrain and quantify the sourcing of tOM contributed to the Arun by its tributaries, we tested four different weighting approaches. In several steps we include ecologic, climatologic, and geomorphic drivers that are expected to influence production and export of tOM.

The first approach assumes that plant waxes are homogeneously produced in and exported from the entire watershed. Thus, we define the function $p_{tOM,trib}(i)$ for tributary tOM contribution relative to the mainstem at confluence *i* as the ratio of the tributary and mainstem catchment areas and we refer to this model as the *catchment size model*:

$$p_{tOM,trib}(i) = A_{trib,i}/(A_{trib,i}+A_{Arun,i}), \quad (5.7)$$

where $A_{trib,i}$ is the tributary catchment area above confluence *i* and $A_{Arun,i}$ the mainstem catchment area above *i* excluding the tributary.

However, because of the inhomogeneous plant cover distribution throughout individual watersheds (Figure 5.1c, 5.2), it is likely that regions with more biomass contribute more tOM than others (*Galy et al.*, 2015). Hence, the second approach uses EVI data as a plant biomass proxy to estimate tOM export

from the tributaries. The relative tOM contributions at confluence *i* ($p_{tOM,trib}$) depend on both catchment size and EVI of the tributary and the mainstem catchments. The relative portion of tOM from catchments is calculated by cumulative EVI above confluence *i* and we refer to it as the *biomass model*:

$$p_{tOM,trib}(i,j,k) = \sum EVI_{trib,i,j}/(\sum EVI_{Arun,i,k}+\sum EVI_{trib,i,j}), \quad (5.8)$$

where $\sum EVI_{trib,i,j}$ is the sum of *j* EVI values within the tributary catchment and $\sum EVI_{Arun,i,k}$ is the sum of *k* EVI values within the Arun catchment above *i*.

In our third approach, we evaluate the role of rainfall on the mobilization of organic matter. Since runoff and particulate organic carbon fluxes are linked (*Schäfer et al.*, 2002), we use annual rainfall as a proxy for runoff and tOM export. We weighted tOM export by TRMM 3B42 derived annual rainfall amounts in the respective catchments as follows and refer to this model as the *runoff model*:

$$p_{tOM,trib}(i,j,k) = \sum TRMM_{trib,i,j}/(\sum TRMM_{Arun,i,k}+\sum TRMM_{trib,i,j}), \quad (5.9)$$

where $p_{tOM,trib}(i,j,k)$ is the relative portion of tOM derived through a tributary at confluence *i*, and $\sum TRMM_{trib,i,j}$ and $\sum TRMM_{Arun,i,k}$ is the tributary and Arun runoff of at confluence *i* calculated as the sum of *j* and *k* TRMM derived values for MAP within the respective watersheds.

Another factor likely affecting export of tOM is erosion. Erosion rates have been argued to relate to topographic indices, for example normalized channel steepness (k_{sn}) (e.g., *Bookhagen and Strecker*, 2012; *DiBiase and Whipple*, 2011; *Kirby and Whipple*, 2012; *Olen et al.*, 2015). The expression of k_{sn} is mostly controlled by tectonic processes (e.g., *Kirby and Whipple*, 2012; *Wobus et al.*, 2006). We tested $p_{tOM,trib}(i,j,k)$ weighting by k_{sn} including TRMM-derived discharge, which has been demonstrated to be a good measure for erosion variability within the Arun valley (*Olen et al.*, 2015). Since the results were not as good as from the *runoff model*, we integrated landscape steepness, discharge, and biomass in our fourth weighting approach based on discharge weighted k_{sn} times

EVI. Each cell of the discharge weighted k_{sn} grid was multiplied with the respective EVI value. We refer to this as the *erosion model*:

$$p_{tOM,trib}(i,j,k) = \sum k_{sn} \cdot EVI_{trib,i,j} / (\sum k_{sn} \cdot EVI_{Arun,i,k} + \sum k_{sn} \cdot EVI_{trib,i,j}), \quad (5.10)$$

where $p_{tOM,trib}(i,j,k)$ is the relative portion of a tributaries' OM at confluence *i*, $\sum k_{sn} \cdot EVI_{trib,i,j}$ is the sum of *j* $k_{sn} \cdot EVI$ values of any pixel *j* within the tributary's watershed and $\sum k_{sn} \cdot EVI_{Arun,i,k}$ the $EVI \cdot k_{sn}$ sum of all pixels *k* within the Arun's watershed above *i*.

We used these four different weighting approaches predicting tOM export from a given tributary (Eq. 5.7 to 15.0) as well as the approximated $\delta D_{bank,trib}$ values (Eq. 5.6) of the respective tributary as input parameters for a mixing model predicting $\delta D_{bank,Arun}$ values along the Arun's mainstem. The calculation of $\delta D_{bank,Arun}$ values at any confluence *i* of the Arun with one of its tributaries' was based on:

$$\delta D_{bank,Arun,i} = p_{tOM,trib,i} \cdot \delta D_{bank,trib,i} + (1 - p_{tOM,trib,i}) \cdot \delta D_{bank,Arun,i-1}, \quad (5.11)$$

where $\delta D_{bank,Arun,i}$ and $\delta D_{bank,Arun,i-1}$ are the Arun mainstem δD_{bank} values below and upstream confluence *i*, $p_{tOM,trib,i}$ is the relative contribution of the tributary (between 0 and 1, derived through Eq. 5.7 to 5.10) and $\delta D_{bank,trib,i}$ is the output of the multi-parameter model (Eq. 5.6). The initial Tibetan Plateau input is represented by the northernmost Arun mainstem sample at 1793 m asl (-206 ± 2‰). Every simulation step incorporated tributaries draining the mainstem within 25 pixels alongside the DEM grid derived flow path of the Arun corresponding to an average distance of 2.6 km. The errors were propagated as follows:

$$\sigma_{bank,Arun,i} = p_{tOM,trib,i} \cdot \sigma_{bank,trib,i} + (1 - p_{tOM,trib,i}) \cdot \sigma_{bank,Arun,i-1}, \quad (5.12)$$

where $p_{tOM,trib,i}$ is the relative plant wax contribution by the tributary at confluence *i*, $\sigma_{bank,trib,i}$ is the standard deviation of modeled $\delta D_{bank,trib}$ values and $\sigma_{bank,Arun,i-1}$ is the uncertainty of the Arun mainstem $\delta D_{bank,Arun}$ value above confluence *i*. The $\sigma_{bank,Arun,i-1}$ start value is 2‰, representing 1σ of the northernmost Arun riverbank sample measurement.

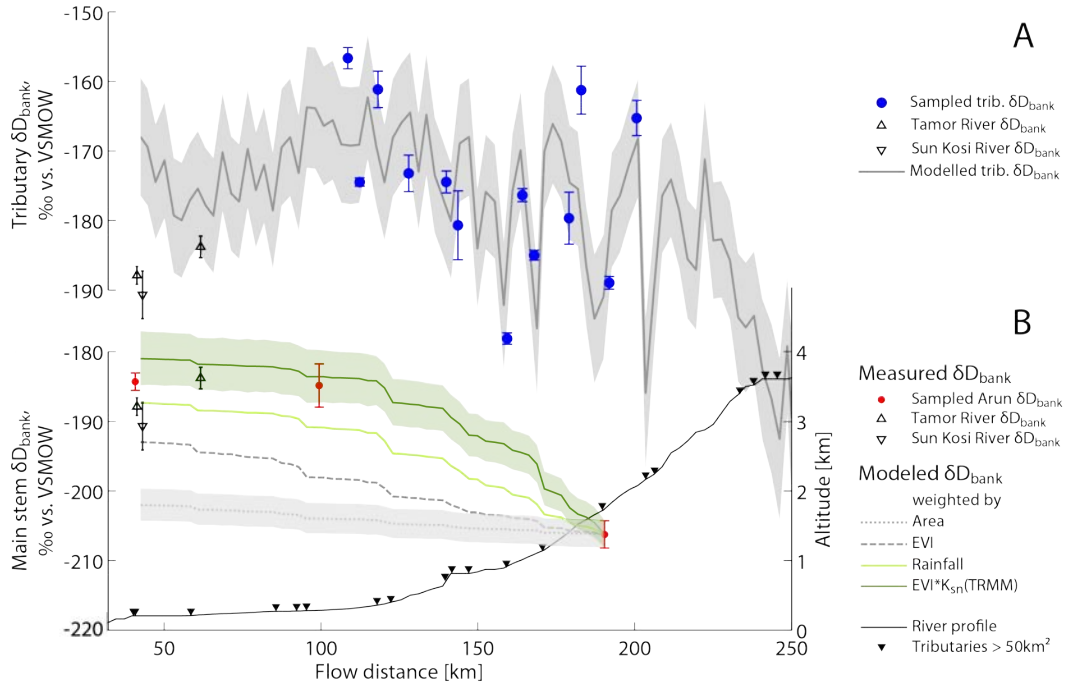

Figure 5.7 Modeling plant wax sources

(A) Tributaries. Modeled δD_{bank} values (grey line) with 95% CI (shading) and measured δD_{bank} values (blue circles, error bars, 1s of triplicate measurements). (B) Arun mainstem. Comparison of model δD_{bank} estimates with mixing proportions of TP and HR sources weighted by catchment size (grey dotted line), EVI (grey dashed line), annual rainfall (bright green solid line) and by EVI combined with the normalized steepness index (k_{sn}) involving discharge (dark green solid line) with standard deviation (shading) for worse and best fit. Measured δD_{bank} values (red circles, error bars as in A) and from Tamor and Sun Koshi rivers sampled nearby (black open triangles, cf. Figure 5.1a).

5.5.3.3 Estimated tOM contributions

The *catchment size model* predicts Tibetan Plateau sources represent 85% of tOM with a predicted value of -202.0 ± 2.3‰ ($\varepsilon_{HR/TP}$ = 5.4 ± 2.9‰) at the lowermost Arun mainstem sampling location, (observed $\delta D_{sed,Arun}$ = -184‰). The *catchment size model* overestimates plant wax export from the plateau, confirming that in the Arun fluvial sourcing is not spatially uniform. The *biomass model* predicts 57% of tOM is sourced from the Tibetan Plateau, with a predicted value of -193.0 ± 3.0‰ at the lowest site and an $\varepsilon_{HR/TP}$ +16.7 ± 3.8‰ (Fig 7B). While these values are closer to observations, the *biomass model* does not capture the full range of downstream $\delta D_{sed,Arun}$ enrichment due to three potential reasons: i) EVI does not differentiate between plant types, which may differ in wax production, and/or ii) EVI does not accurately represent vegetation cover due to the presence of snow in the higher-elevation part of the catchment (Justice et al.,

1998), and/or iii) biomass may not be linearly related to the amount of exported tOM due to additional physical controls on erosion, including catchment geomorphology and climatic conditions.

Therefore, in the third approach we account for runoff by approximating it with rainfall rates. The *runoff model* predicts that 35% of tOM in the Arun is derived from the Tibetan Plateau, and 65% originates from within the Himalayan Ranges. The contribution weighted isotopic composition at the lowermost sample site was -187.3 ± 3.5‰ and $\varepsilon_{HR/TP}$ was +23.9 ± 4.4‰, within error of the observed $\delta D_{sed,Arun}$ value of -184‰ and enrichment of +27.7± 5‰, although the central Arun mainstem sample $\delta D_{sed,Arun}$ value (-185‰) is not well predicted by this approach (Figure 5.7b). The *erosion model* accounting for plant cover (EVI) and erosive capacity (k_{sn}) predicts 21% from the plateau and 79% from the Himalayan Ranges with a predicted $\delta D_{sed,Arun}$ value of -181.0 ± 3.9‰ for the lowermost site and $\varepsilon_{HR/TP}$ of +31.8 ± 4.9‰, within error of the observed enrichment, as well as from the output of the *runoff model*. Only the *erosion model* predicted the isotopic composition of the central Arun mainstem sample within error margins, suggesting that the combination of vegetation abundance and erosive capacity best describes the export of OM in the Arun watershed. We note that uncertainties on k_{sn}*EVI estimates associated with shifting vegetation types and different wax loading are going to be more important to overall uncertainties than those associated with snow cover-EVI interference given the small plant biomass expected in snow-covered regions. The *erosion model* matches observational data in the Arun River and supports recent findings about the role of erosion on OM mobilization in river catchments globally (*Galy et al.*, 2015). Our comparison of four different weighting approaches suggests that weighting that accounts for catchment area, as well as ecologic, climatic and geomorphic parameters can best explain field observations. As such, our model predicts that regions with dense vegetation, high precipitation and erosion rates are most important source areas for tOM.

5.5.4 Implications for the plant wax paleohydrology proxy

Our spatial sampling along a large trans-Himalayan river showed that dD values of plant waxes extracted from tributary riverbank deposits are

representative of the catchments vegetation and δD_{water} values (Figure 5.4b). We found a relationship of $\delta D_{bank,trib} = 0.45*\delta D_{water}-147‰$ ($R = -0.54$, $p = 0.03$) that largely supports earlier studies showing a good correlation in fluvial deposits (*Galy et al.*, 2011; *Ponton et al.*, 2014) and lacustrine archives (*Garcin et al.*, 2012; *Huang et al.*, 2004; *Polissar and Freeman*, 2010; *Sachse et al.*, 2004). Notably, we found a similar relationship between δD_{water} and $\delta D_{bank,trib}$ as Ponton et al. (2014) in a very different climatic and ecological context. Global data of annual mean precipitation and lacustrine plant wax *n*-alkane δD values (*Garcin et al.*, 2012; *Polissar and Freeman*, 2010; *Sachse et al.*, 2004) are characterized by a slightly steeper slope but comparable regression intercept $\delta D(lakes) = 0.55*\delta D_{water}+148‰$ ($r^2 = 0.8$, $p < 0.01$) (Figure 5.4b). However, they are the same within the 95% confidence interval (Figure 5.4b). But most calibration studies in lacustrine environments have compared surface sediment plant wax δD values to annual mean precipitation δD (*Garcin et al.*, 2012; *Polissar and Freeman*, 2010; *Sachse et al.*, 2004), which is assumed to be the source water in most contexts. We correlate $\delta D_{bank,trib}$ to post ISM surface water that is likely different from annual mean precipitation δD values due to evaporation, mixing with ground water and potential melt water input.

Whereas we confirm the link of $\delta D_{bank,trib}$ values and the isotopic composition of environmental water, our plant wax quantification approach further indicates that plant wax sourcing along the Arun is strongly biased towards tributaries with significant vegetation cover and high erosion capacities. This suggests that the interplay between ecological, climatological, and geomorphic processes over geological timescales should to be taken into account for the interpretation of paleoclimate records from comparable fluvial systems.

To illustrate potential effects on paleoclimate archives, we consider climate changes towards more humid conditions with a stronger ISM. Such a scenario would be expected to lead to decreasing precipitation δD values due to the amount effect (*Dansgaard*, 1964) and reduced leaf water isotope enrichment (*Kahmen et al.*, 2013b). In addition, vegetation cover is expected to expand to higher elevations, with more precipitation and more extreme precipitation events (Bookhagen et al., 2005) with increasing erosion in these higher altitude areas. In such a scenario, the export of tOM from higher altitudes with more D-depleted

source waters would be enhanced, leading to an amplified decrease in plant wax δD values of the downstream archive. A dry shift would be expected to have the opposite effects. We therefore anticipate that ecologic and erosional responses to climate changes would amplify recorded signals, which implies that a quantitative reconstruction of past rainfall δD values and by extension rainfall amounts from plant wax δD values alone is difficult in such a setting. Our findings also imply that tectonic changes on longer geological timescales, e.g., as a consequence of mountain range uplift, would change tOM source areas of fluvial deposits to the loci of erosion.

5.6 Conclusions

We measured the plant wax hydrogen isotopic composition of plant leaves, river coarse particulate organic matter and riverbank sediments from the trans-Himalayan Arun River and tributaries in Nepal. We found that plant wax *n*-alkanes in river sediments reflect the isotopic composition of modern plants in their catchments and that those plant waxes carry signatures of the gradient in precipitation isotopes with elevation. We use these relationships together with remote sensing data for vegetation cover, precipitation amount and slope steepness to understand terrestrial organic matter sources of fluvial sediments. Mixing-models accounting for climatic, ecologic and geomorphic factors suggest that fluvial transport does not uniformly mobilize plant waxes from across the vast catchment area. Instead, sourcing is dominated by tributaries within the lowermost 15% of the catchment, draining the Arun between 205 and 1793m river elevation. Our remote sensing-based modeling approaches demonstrated that the presence of vegetation in the Arun's tributaries is necessary, but not sufficient for high terrestrial organic matter export rates. The best fit to plant wax observational data finds areas with high plant cover, high precipitation and steep slopes, to contribute the largest amount of terrestrial organic matter, emphasizing the importance of erosion processes for terrestrial organic matter mobilization. Our novel modeling approach provides quantitative insights into the sourcing of plant wax biomarkers in this catchment and introduces a new interpretative framework. This framework enables robust interpretations of modern terrestrial biomarker

sourcing and provides better constraints on the interpretation of plant wax proxy records in terms of past hydrologic change in river catchments.

Acknowledgements

BH was funded through DFG GRK 1364 and UNVEU 1966, SF through US National Science Foundation (EAR-1227192 and OCE-1401217) and the USC Women in Science and Engineering Program and DS through an Emmy-Noether grant from the German Science Foundation (DFG SA1889/1-1 and 1-2). Thanks to Manoj, Sophia Wagner and Raphael Scheffler for field assistance and Miguel Rincon, Michael Pöhle and Denise Jekel for lab assistance.

Chapter 6: Discussion & Conclusions

The primary aim of this thesis was to better understand the rates and spatial patterns of denudation in the Himalaya, and to what degree tectonic, climatic, and biotic forces drive these rates. This endeavor was undertaken at a regional scale in the central Himalayan Arun Valley of Nepal and at the scale of the entire orogen across, and along strike of the Himalaya. The topographic, lithologic, and climatic conditions of the Arun Valley make this region particularly well suited to such a study. The Arun is one of the largest trans-Himalayan rivers, carrying sediment from both the humid, densely vegetated Himalaya and from the arid southern Tibetan Plateau. This physiographic setting allows for a comparison of ^{10}Be TCN concentration and denudation rates from the border of the Tibetan Plateau and the Himalaya. This type of information had not previously been available from studies in Central Nepal, Bhutan, or the Garhwal Himalaya (*Vance et al.*, 2003; *Wobus et al.*, 2005; *Godard et al.*, 2012; *Godard et al.*, 2014; *Scherler et al.*, 2014; *Le Roux-Mallouf et al.*, 2015; *Morell et al.*, 2015; *Portenga et al.*, 2015) and thus a allows for a new look at large-scale denudation patterns in one of the most important Cenozoic mountain belts.

The Arun Valley is a deeply incised, high-relief landscape that represents a morphologically unique region, exhibiting neither the large sediment accumulation and storage observed in Central Nepal and the Kathmandu Basin to the west (e.g., *Iwata et al.*, 1982; *Yamanaka and Iwata*, 1982), nor the large regions of high-altitude, low-relief surfaces observed in Bhutan to the east (e.g., *Grujic et al.*, 2006; *Le Roux-Mallouf et al.*, 2015; *Portenga et al.*, 2015), although it possesses both aspects to a limited degree. Because of its deeply incised and high-relief morphology, the focused incision of the Arun River has been proposed to be mechanically linked with the uplift of an extensive, river-parallel anticline (*Oberlander*, 1985; *Montgomery and Stolar*, 2006). Despite these different aspects of drainage-network and landscape evolution, there is only a limited amount of data quantifying denudation rates either spatially, from Central Nepal to Bhutan, or temporally on geologic (e.g., $>10^5$ yr), centennial to millennial (10^2-10^5 yr) or decadal timescales. In light of these conditions, this thesis investigated

three principal research questions concerning denudation processes at various spatial scales in the Arun Valley and across the Himalaya.

To assess denudation rates and the processes that impact ^{10}Be TCN concentrations in an active orogen on the regional scale, I generated and analyzed new catchment-mean ^{10}Be TCN data from the Arun Valley in eastern Nepal. Due to the fact that climate, tectonics, and topography strongly co-vary across strike (from south to north), I focus along strike (from east to west) of the Himalayan arc to investigate how climatic and biotic factors influence denudation rates and topography. Lastly, the patterns of denudation rates and their relationship to regional topography I document in the previous chapters is applied to a model of terrestrial organic carbon transport to better understand the source areas of biomarker archives. Chapters 3 through 5 discuss in detail the different research questions and form the core of three separate manuscripts, respectively. Here, I will discuss the key findings of these studies in the broader context of denudation studies in active mountain belts and the implications of my study for the interpretation of past, present, and future denudation rates and surface processes in high-elevation regions.

6.1 Denudation in the Himalaya at regional and orogen scales

At the regional scale, my investigations document a five-fold, across-strike (S-N) increase of denudation rates from tributaries to the Arun River. Denudation rates increase abruptly at the transition zone between the Lesser and Higher Himalaya, from moderate denudation rates in the Lesser Himalaya (0.2 - 0.5 mm/yr) to moderately high denudation rates in the topographic transition zone (0.5 - 0.8 mm/yr), to the highest denudation rates in the Higher Himalaya (0.5 - 1.4 mm/yr). Across the Central and Western Himalaya, there is a similar increase from the Lesser to Higher Himalaya (excluding Bhutan, which demonstrates differing topographic and tectonic characteristics (e.g., *Le Roux-Mallouf et al.*, 2015)). Mean denudation rates in the Lesser Himalaya measure 0.35 ± 0.28 mm/yr (median value of 0.24 mm/yr, n = 59), and increase in the Higher Himalaya to a mean value of 0.89 ± .65 mm/yr (median value = 0.65 mm/yr, n = 34). Interestingly, denudation rates in the Arun Valley correlate well to tectonically-linked normalized channel steepness (k_{sn}), but show no strong

correlation to climatic factors, such as mean annual rainfall. The general pattern and magnitude of denudation rates in the Arun Valley are similar to those published for areas in Central Nepal (*Godard et al.*, 2014) and the Garhwal Himalaya (*Scherler et al.*, 2014; *Morell et al.*, 2015), where researchers have documented evidence for tectonic-forcing of denudation rates. The morphology of the Arun Valley, with abrupt increases of topographic steepness at the fronts of the Lesser and Higher Himalaya, the strong correlation between denudation rates and topographic steepness, and the similarity of denudation rates in the Arun Valley with those in Central Nepal and the Garhwal Himalaya are consistent with an interpretation of tectonically-forced denudation rates perpendicular to the strike of the orogen.

Along strike of the Himalaya, however, I present robust evidence that climatic and the biotic parameters modulate denudation rates. Median denudation rates remain relatively constant along a distance of ~1500 km along the Himalayan arc, varying between 0.3 - 04 mm/yr. The lowest denudation rates, e.g., 25th percentile, likewise remain fairly constant at ~0.1 mm/yr. However, despite steep hillslopes and an active tectonic regime, I observe a general decrease in the highest denudation rates from west to east; the 75th percentile of denudation rates decreases from ~2.0 mm/yr in the Sutlej Valley to 0.5 mm/yr in Bhutan. This eastward decrease in the highest denudation rates, or the range of denudation rates along strike, correlates to decreasing seasonality of vegetation cover, increasing vegetation density, and increasing rainfall along strike of the orogen. Based on these observations, I propose that a transition from a highly seasonal plant cover to increasingly stable, dense vegetation cover modulates denudation rates so that measured denudation rates are more constant and less susceptible to stochastic climate-driven processes (e.g., large storms). This notion is supported by observations on short timescales obtained by a study of suspended sediment concentration from gauging stations in the Sutlej Valley of the NW Himalaya (*Wulf et al.*, 2012), which found that in this highly seasonal, sparsely vegetated region, the highest sediment yields are generated by infrequent and large storms. I therefore suggest that vegetation plays a key to providing stability to hillslopes, inhibiting denudation, and modulating sediment availability to the fluvial system (c.f., *Collins et al.*, 2004; *Istanbulluoglu et al.*, 2004; *Istanbulluoglu and Bras*, 2005). Highly seasonal vegetation cover may also contribute to higher denudation

rates associated with glacial and snow melt (*Wulf et al.*, 2012). For example, Bookhagen and Burbank (2010) documented peak snowmelt in the western Himalaya in late spring and early summer (MJJ). In the western Himalaya, vegetation density transitions from winter to summer vegetation between the months of April to July. This may therefore result in a higher impact of snow melt on denudation rates when snowmelt is high and vegetation density is still relatively low, whereas in the eastern regions where snowmelt plays a lower role in annual river discharge and winter vegetation density is higher, denudation rates are lower and less variable.

Andermann et al. (2012) showed that denudation rates derived from suspended sediment measured over annual to decadal timescales at the outlet of major Nepali Himalayan rivers generally ranges from ~0.2 to 1.5 mm/yr, within the range of denudation rates measured by ^{10}Be TCN concentrations. An exception is the Kali Gandaki, where the suspended-sediment derived denudation rate is significantly higher (2.8 mm/yr). While denudation rates from ^{10}Be TCN in tributaries to the Kali Gandaki are lower (~0.5 mm/yr), it can be noted that these do not include measurements from the high-relief Kali Gandaki Gorge region. In contrast to rates derived from ^{10}Be TCN data, the suspended sediment records presented by Andermann et al. (2012) document low denudation rates from the Higher Himalaya, ranging from 0.1 to 0.3 mm/yr. These apparently low denudation rates, up to an order of magnitude lower than those based on ^{10}Be TCN concentrations, may result from the shorter integration time of suspended sediment (annual to decadal timescale), which likely does not represent the duration of a complete seismic cycle or integrate landsliding events in this region. Although there are no measurements of suspended sediment in tributaries to the Arun River or in its upper sectors, denudation rates obtained from the outlet of the Arun River and from the Sapt Kosi are similar to suspended sediment-derived rates estimated by Andermann et al. (2012) (0.91 ± 0.07 mm/yr from ^{10}Be TCN denudation rate, 0.9 +1.5/-0.5 mm/yr derived from suspended sediment concentration). The similarity between denudation rates derived from suspended sediment and from ^{10}Be TCN concentrations suggests that modern denudation rates from the Arun and Sapt Kosi, and across much of the Nepalese Himalaya, have not changed significantly during the last ~1 kyr.

It is notable that across the Himalaya, catchment-mean denudation rates from TCN are generally lower than exhumation and tectonic uplift rates determined either by low-temperature thermochronology (*Herman et al.*, 2010; *Thiede and Ehlers*, 2013; *Coutand et al.*, 2014) or by river incision (*Lavé and Avouac*, 2001), respectively. In chapter 4, I proposed that the discrepancy between ^{10}Be-derived denudation rates and long-term exhumation rates from thermochronology in the Lesser Himalaya may be related to the contribution of landsliding to catchment denudation. A possible explanation for the discrepancy between ^{10}Be TCN derived denudation rates (10^2-10^5 yr) and thermochronological rates (>10^5 yr) specifically in the Higher Himalaya is the role of glacial erosion. Because low-temperature thermochronology does not rely on surface exposure to calculate long-term exhumation rates, it is generally thought to be an accurate estimator of exhumation in glaciated regions (e.g., *Ehlers et al.*, 2006). The relatively lower rates of denudation from glaciated catchments recorded by ^{10}Be TCN (e.g., 1.48 ± 0.11 mm/yr in ARU-12-11) compared to thermochronology-based exhumation rates (>2 mm/yr in the Higher Himalaya) (*Godard et al.*, 2004; *Herman et al.*, 2010; *Thiede and Ehlers*, 2013) may result from an oversimplification of the ice-shielding routine. As described in chapter 3, to account for the surface shielding of catchment surfaces beneath glacial ice from cosmic rays, we assume that no ^{10}Be is produced in glaciated regions of the catchment. In many glacial settings, however, sediment is produced not only beneath the glacier, but is transported on the surface of the glacier before being delivered to proglacial streams and sedimentary deposits (e.g., *Anderson*, 2000). Such supraglacial debris will accumulate ^{10}Be as it is transported on the surface of the glacier (e.g., *Heimsath and McGlynn*, 2008; *Seong et al.*, 2009; *Ward and Anderson*, 2011). In this case, the strict principle of ice shielding will result in an underestimation of catchment-mean denudation rates. A quantitative estimate of the length of time sediment is exposed on the surface of the glacier, and the relative contribution of supra- and subglacial sediment to proglacial streams, is necessary to more accurately and realistically account for glacial shielding. Further work modeling the ^{10}Be production and contribution of sediment transported on the surface of the glacier would greatly benefit our understanding of denudation rates derived from cosmogenic nuclide concentrations in glaciated regions.

6.2 Interpretation and application of ^{10}Be TCN concentrations and denudation rates

6.2.1 Interpretation of ^{10}Be TCN concentrations

The measurement of catchment-mean denudation rates from terrestrial cosmogenic nuclides has become a widely-used tool amongst geomorphologists (e.g., *Granger et al.*, 2013). Until recently, it was generally assumed that the grain-size analyzed for ^{10}Be measurement was representative of the catchment upstream of the sampling site and of the denudation processes in the catchment, provided the catchment is large enough and the sediment well-mixed (*Niemi et al.*, 2005; *Yanites et al.*, 2009). Recent field studies have cast doubt on this assumption, however. The results of studies analyzing ^{10}Be concentrations in multiple grain sizes in Central Nepal (*Puchol et al.*, 2014) and in the Andes (*McPhillips et al.*, 2014; *Carretier et al.*, 2015) have suggested that the standard grain size used for ^{10}Be analysis may exclude denudation from mass wasting. These authors argue that landslide-related denudation rates may, instead, be preserved in larger grain sizes (e.g., >2 mm diameter) and cobbles. In my study of ^{10}Be concentrations from the Arun Valley, I suggest another means by which an analyzed sand sample may not reflect the upstream catchment.

Downstream fining of sand grains in large catchments may result in the exclusion of grains from the uppermost sectors of the catchment. Previous research suggests that in high-energy rivers, grain sizes <2 mm stay in suspension and do not fine past the sand fraction (*Sklar et al.*, 2006; *Chatanantavet et al.*, 2010). Generally, although practices vary, researchers use only the 250 - 710 µm grain size fraction to measure ^{10}Be concentration (e.g., *Granger et al.*, 1996; *Safran et al.*, 2005; *Bookhagen and Strecker*, 2012). Thus anything finer than 250 µm will be operationally excluded from the measurement, and hence not be represented in the calculated denudation rate. In this thesis, however, I provide evidence that quartz grains in the Arun River continue to fine past 250 µm diameter. The trans-Himalayan Arun catchment, which includes both the high-altitude, low-relief Tibetan Plateau with high ^{10}Be production rates and the low-altitude, high-relief Himalaya with low ^{10}Be production rates, provided the ideal setting for the detection of this effect. However, the same process may occur undetected in catchments without measurable differences in production rates

between upstream and downstream sectors, such as the Sun Kosi or Tamor Rivers and other large Himalayan rivers. It is noteworthy that the upper sectors of the Arun River in Tibet are largely composed of sedimentary and metasedimentary material in which quarts grains may be already fined and less resistant to fining than potentially larger quartz grains from younger crystalline rocks. However, because our observations are limited to this setting, we cannot conclusively determine if differences in lithology are responsible for the proposed downstream grain fining. However, in future studies it should be taken care when interpreting ^{10}Be concentrations from large watersheds, and in particular those with large upstream sedimentary lithologies, as material from the uppermost sectors may be excluded from analysis.

6.2.2 Interpretation of denudation rates and topography

The functional relationship between denudation rates and topographic steepness (e.g., hillslope gradient, local relief, or normalized channel steepness) is frequently employed by geomorphologists to interpret the dynamics of landscapes and draw conclusions about the underlying long-term tectonic activity of a region (e.g., *Ahnert*, 1970; *Wobus et al.*, 2006; *DiBiase et al.*, 2010). Although these functional relationships may be linear in slowly denuding landscapes, such as the East African Rift System (*Torres Acosta et al.*, 2015), in many highly dynamic – tectonically and/or climatically- regions the relationship observed between denudation rates and topographic steepness is rather nonlinear and subject to threshold processes (e.g., *Carson*, 1971; *M Anderson et al.*, 1980; *Montgomery*, 2001; *Binnie et al.*, 2007). In landscapes dominated by threshold processes, topography will steepen in response to increasing denudation or uplift rates up to a certain degree (e.g., ~30˚ hillslope angle for most clastic lithologies). Beyond this threshold, topography cannot continue to steepen and becomes unresponsive to changes in denudation rate (e.g., *Penck and Penck*, 1924; *Burbank et al.*, 1996). In Chapter 4, I document evidence that suggests that the degree of nonlinearity of the functional relationship between denudation rates and topographic steepness scales to rainfall and vegetation density. In humid, densely vegetated regions of the Himalaya, the relationship between denudation rates and topographic steepness is more linear (power law exponent of ~0.4 - 0.5) compared to dry,

sparsely vegetated environments, where the functional relationship is highly nonlinear (power law exponent < 0.25). The relative linearity of the relationship between denudation rates and topography scales only to climatic factors and does not significantly correlate to dominant lithology or to uplift rates inferred from low-temperature thermochronology data obtained in the Higher or Lesser Himalayan Crystalline rocks (*Thiede and Ehlers*, 2013). The results of my thesis therefore suggest that climatic factors, and in particular vegetation density and cover, have a measurable impact on the relative topographic threshold values of different compartments of the Himalayan orogen.

6.3 Conclusions

The aim of this thesis was to provide answers to several research questions concerning the forcing factors of denudation in high-elevation montantane environments, laid out in Chapter 1. First I set out ***to determine how the tectonic, climatic, and geomorphic processes of a highly active orogen impact ^{10}Be TCN concentrations and the resulting denudation rates.*** I addressed this question with a regional study of ^{10}Be TCN samples from the Arun Valley, Nepal. Second, because the steep interdependent relationships between topography, denudation, and climate make it difficult to determine the role of independent factors, I proposed ***to assess how climate and vegetation affect denudation rates and topography along strike of the Himalaya.*** Third, as terrestrial organic matter is increasingly used for paleoclimatic and paleohydrological studies, I ***applied the regional quantification of denudation rates and topographic steepness to better understand biomarker archives***. In light of these research tasks, I have reached the following conclusions:

(1) Downstream fining continues in the sand fraction in the Arun River and may occur in other large, high-energy rivers. Downstream fining of sand grains in extensive watersheds may result in a non-representative result when only standard grain size fractions are analyzed. Analyzing a wider range of grain sizes, including those <250 μm, may reduce this problem. However, it should be noted that very small grains may be lost in the leaching stage. Thus, detrital samples may not reflect the complete upstream watershed. Further work

quantifying the degree and rates of downstream fining of sand grains is therefore an important future research avenue.

(2) Local denudation rates in the Arun Valley show a five-fold gradient across strike (S-N). Denudation rates increase abruptly at the topographic transition from the Lesser to Higher Himalaya and remain high through the Higher Himalaya, particularly in glaciated catchments. Denudation rates are well predicted by normalized channel steepness (R^2 = 0.67) and exhibit a similar spatial pattern and magnitudes of similar studies from the Garhwal Himalaya and Central Nepal. I therefore conclude that across strike, measured denudation rates in the Arun Valley are consistent with the notion of dominant, tectonically-driven denudation.

(3) Along strike (E-W), however, climate and vegetation modulate the regional variability of denudation rates and the relationship between denudation rates and topography. High vegetation seasonality in the Northwest Himalaya scales with high denudation rates and high denudation rate variability, which decreases towards the east where vegetation cover is comparably stable.

(4) Vegetation density in the Himalaya modulates the power law relationship between denudation rates and topographic steepness metrics (e.g., hillslope gradient, normalized channel steepness, specific stream power), such that the relationship is more nonlinear in sparsely vegetated regions and becomes increasingly linear as vegetation density increases. Globally, other factors may impact the degree of linearity of the relationship between denudation rates and topographic steepness; however, within regions where tectonic forcing is similar (order-of-magnitude), this may be a key factor in understanding variations in this relationship.

(5) Regional patterns of denudation rates are critical to accurately reconstructing the source area of terrestrial organic matter in very dynamic orogens. Stable isotopes in plant wax *n*-alkanes from terrestrial organic matter suspended in stream water and deposited along riverbanks reliably records modern precipitation in the Arun Valley and the regional precipitation gradient. Plant wax biomarkers preserved in sedimentary archives are thus a reliable and important proxy for past climate and hydrology. Topographic metrics that are linked to denudation rates (e.g., normalized channel steepness) can be

successfully employed to reconstruct the source area of deposited terrestrial organic material.

References

Adams, B. A., K. V. Hodges, K. X. Whipple, T. A. Ehlers, M. C. van Soest, and J. Wartho (2015), Constraints on the tectonic and landscape evolution of the Bhutan Himalaya from thermochronometry, *Tectonics*, *34*(6), 1329-1347.

Adlakha, V., K. A. Lang, R. C. Patel, N. Lal, and K. W. Huntington (2013), Rapid long-term erosion in the rain shadow of the Shillong Plateau, Eastern Himalaya, *Tectonophysics*, *582*(0), 76-83.

Ahnert, F. (1970), Functional relationships between denudation, relief, and uplift in large mid-latitutde drainage basins, *American Journal of Science*, *268*, 243-263.

Anders, A. M., G. H. Roe, B. Hallet, D. R. Montgomery, N. J. Finnegan, and J. Putkonen (2006), Spatial patterns of precipitation and topography in the Himalaya, *Geological Society of America Special Papers*, *398*, 39-53.

Anderson, M., K. Richards, and P. Kneale (1980), The role of stability analysis in the interpretation of the evolution of threshold slopes, *Transactions of the Institute of British Geographers*, 100-112.

Anderson, R. S. (2000), A model of ablation-dominated medial moraines and the generation of debris-mantled glacier snouts, *Journal of Glaciology*, *46*(154), 459-469.

Avouac, J. P. (2003), Mountain building, erosion, and the seismic cycle in the Nepal Himalaya, *Advances in Geophysics*, *46*, 1-80.

Balco, G., J. O. Stone, N. A. Lifton, and T. J. Dunai (2008), A complete and easily accessible means of calculating surface exposure ages or erosion rates from 10Be and 26Al measurements, *Quaternary Geochronology*, *3*(3), 174-195.

Barros, A. P., S. Chiao, T. J. Lang, D. W. Burbank, and J. Putkonen (2006), From weather to climate--Seasonal and interannual variability of storms and implications for erosion processes in the Himalaya, *Geological Society of America Special Papers*, *398*, 17-38.

Beaumont, C., R. A. Jamieson, M. H. Nguyen, and B. Lee (2001), Himalayan tectonics explained by extrusion of a low-viscosity crustal channel coupled to focused surface denudation, *Nature*, *414*(6865), 738-742.

Berner, R.A., 1990. Atmospheric Carbon Dioxide Levels Over Phanerozoic Time. Science (80-.). 249, 1382–1386. doi:10.1126/science.249.4975.1382

Bierman, P., and E. J. Steig (1996), Estimating rates of denudation using cosmogenic isotope abundances in sediment, *Earth Surface Processes and Landforms*, *21*, 125-139.

Binnie, S. A., W. M. Phillips, M. A. Summerfield, and L. K. Fifield (2007), Tectonic uplift, threshold hillslopes, and denudation rates in a developing mountain range, *Geology*, *35*(8), 743-746.

Bissell, M. H. (1921), On the Use of the Terms ``Denudation,'' ``Erosion,'' ``Corrosion'' and ``Corrasion'', *Science*, *53*(1374), 412-414.

Blythe, A. E., D. W. Burbank, A. Carter, K. Schmidt, and J. Putkonen (2007), Plio-Quaternary exhumation history of the central Nepalese Himalaya: 1. Apatite and zircon fission track and apatite [U-Th]/He analyses, *Tectonics*, *26*(3), TC3002.

Bollinger, L., J. P. Avouac, O. Beyssac, E. J. Catlos, T. M. Harrison, M. Grove, B. Goffé, and S. Sapkota (2004), Thermal structure and exhumation history of the Lesser Himalaya in central Nepal, *Tectonics*, *23*(5), TC5015.

Bonnet, S. (2009), Shrinking and splitting of drainage basins in orogenic landscapes from the migration of the main drainage divide, *Nature Geosci*, *2*(11), 766-771.

Bookhagen, B. (2010), Appearance of extreme monsoonal rainfall events and their impact on erosion in the Himalaya, *Geomatics, Natural Hazards and Risk*, *1*(1), 37-50.

Bookhagen, B., and D. W. Burbank (2006), Topography, relief, and TRMM-derived rainfall variations along the Himalaya, *Geophysical Research Letters*, *33*(8), L08405.

Bookhagen, B., and D. W. Burbank (2010), Toward a complete Himalayan hydrological budget: Spatiotemporal distribution of snowmelt and rainfall and their impact on river discharge, *Journal of Geophysical Research: Earth Surface*, *115*(F3), F03019.

Bookhagen, B., and M. R. Strecker (2012a), Spatiotemporal trends in erosion rates across a pronounced rainfall gradient: Examples from the southern Central Andes, *Earth and Planetary Science Letters*, *327-328*(0), 97-110.

Bookhagen, B., M R Strecker (2012a), Spatiotemporal characteristics of climatic forcing of erosion - examples from the southern Central Andes and the Himalaya, Abstract GC22C-06 presented at 2012 Fall Meeting, AGU, San Francisco, Calif., 3-7 Dec.

Bookhagen, B., R. C. Thiede, and M. R. Strecker (2005a), Late Quaternary intensified monsoon phases control landscape evolution in the northwest Himalaya, *Geology*, *33*(2), 149-152.

Bookhagen, B., R. C. Thiede, and M. R. Strecker (2005b), Abnormal monsoon years and their control on erosion and sediment flux in the high, arid northwest Himalaya, *Earth and Planetary Science Letters*, *231*(1-2), 131-146.

Bookhagen, B., D. Fleitmann, K. Nishiizumi, M. R. Strecker, and R. C. Thiede (2006), Holocene monsoonal dynamics and fluvial terrace formation in the northwest Himalaya, India, *Geology*, *34*(7), 601-604.

Boos, W. R., Kuang, Z. (2010), Dominant control of the South Asian monsoon by orographic insulation versus plateau heating, *Nature*, *463*(7278), 218-222.

Bouchez, J., Galy, V., Hilton, R.G., Gaillardet, J., Moreira-Turcq, P., Pérez, M.A., France-Lanord, C., Maurice, L., 2014. Source, transport and fluxes of Amazon River particulate organic carbon: Insights from river sediment depth-profiles. Geochim. Cosmochim. Acta 133, 280–298. doi:10.1016/j.gca.2014.02.032

Bray, H. E., and S. Stokes (2004), Temporal patterns of arid-humid transitions in the south-eastern Arabian Peninsula based on optical dating, *Geomorphology*, *59*(1-4), 271-280.

Brown, E. T., R. F. Stallard, M. C. Larsen, G. M. Raisbeck, and F. Yiou (1995), Denudation rates determined from the accumulation of in situ-produced 10Be in the luquillo experimental forest, Puerto Rico, *Earth and Planetary Science Letters*, *129*(1–4), 193-202.

Brozovic, N., and D. W. Burbank (2000), Dynamic fluvial systems and gravel progradation in the Himalayan foreland, *Geological Society of America Bulletin*, *112*(3), 394-412.

Büdel, J. (1982), *Climatic Geomorphology*, 444 pp., Princeton University Press, Princeton, NJ.

Bull, W. B. (1991), Geomorphic responses to climatic change.

Burbank, D. W., R. A. Beck, and T. Mulder (1996a), The Himalayan foreland basin, *World and regional geology*, *1*(8), 149-190.

Burbank, D. W., J. Leland, E. Fielding, R. S. Anderson, N. Brozovic, M. R. Reid, and C. Duncan (1996b), Bedrock incision, rock uplift and threshold hillslopes in the northwestern Himalayas, *Nature*, *379*(8), 505-510.

Burbank, D. W., A. E. Blythe, J. Putkonen, B. Pratt-Sitaula, E. Gabet, M. Oskin, A. Barros, and T. P. Ojha (2003), Decoupling of erosion and precipitation in the Himalayas, *Nature*, *426*(6967), 652-655.

Burchfiel, B. C., C. Zhiliang, K. V. Hodges, L. Yuping, L. H. Royden, D. Changrong, and X. Jiene (1992), The South Tibetan Detachment System, Himalayan Orogen: Extension Contemporaneous With and Parallel to Shortening in a Collisional Mountain Belt, *Geological Society of America Special Papers*, *269*, 1-41.

Burdige, D.J., 2005. Burial of terrestrial organic matter in marine sediments: A re-assessment. Global Biogeochem. Cycles 19, doi:10.1029/2004GB002368

Cannon, F., L. V. Carvalho, C. Jones, and B. Bookhagen (2015), Multi-annual variations in winter westerly disturbance activity affecting the Himalaya, *Clim Dyn*, *44*(1-2), 441-455.

Carpenter, C., and R. Zomer (1996), Forest Ecology of the Makalu-Barun National Park and Conservation Area, Nepal, *Mountain Research and Development*, *16*(2), 135-148.

Carretier, S., et al. (2015), Differences in 10Be concentrations between river sand, gravel and pebbles along the western side of the central Andes, *Quaternary Geochronology*, *27*, 33-51.

Carretier, S., et al. (2013), Slope and climate variability control of erosion in the Andes of central Chile, *Geology*, *41*(2), 195-198.

Carson, M. (1971), An application of the concept of threshold slopes to the Laramie Mountains, Wyoming, *Institute of British Geographers Special Publication*, *3*, 31-47.

Cattin, R., and J. Avouac (2000), Modeling mountain building and the seismic cycle in the Himalaya of Nepal, *Journal of Geophysical Research*, *105*(B6), 13389-13407.

Charney, J. G. (1969), The intertropical convergence zone and the hadley circulation of the atmosphere, *Proc. WMO/IUCG Symp. Nu- mer. Weather Predict. Jpn. Meteorol. Agency*, *III*, 73-79.

Chatanantavet, P., E. Lajeunesse, G. Parker, L. Malverti, and P. Meunier (2010), Physically based model of downstream fining in bedrock streams with lateral input, *Water Resources Research*, *46*(2), W02518.

Chmeleff, J., F. von Blanckenburg, K. Kossert, and D. Jakob (2010), Determination of the 10Be half-life by multicollector ICP-MS and liquid scintillation counting, *Nuclear Instruments and Methods in Physics Research Section B: Beam Interactions with Materials and Atoms*, *268*(2), 192-199.

Clift, P. D., N. Shimizu, G. D. Layne, J. S. Blusztajn, C. Gaedicke, H.-U. Schlüer, M. K. Clark, and S. Amjad (2001), Development of the Indus Fan and its significance for the erosional history of the Western Himalaya and Karakoram, *Geological Society of America Bulletin*, *113*(8), 1039-1051.

Collins, D. B. G., R. L. Bras, and G. E. Tucker (2004), Modeling the effects of vegetation-erosion coupling on landscape evolution, *Journal of Geophysical Research: Earth Surface*, *109*(F3), F03004.

Copeland, P., T. M. Harrison, K. V. Hodges, P. Maruéjol, P. Le Fort, and A. Pecher (1991), An Early Pliocene thermal disturbance of the main central thrust, central Nepal: Implications for Himalayan tectonics, *Journal of Geophysical Research: Solid Earth*, *96*(B5), 8475-8500.

Coppus, R., and A. Imeson (2002), Extreme events controlling erosion and sediment transport in a semi-arid sub-Andean valley, *Earth Surface Processes and Landforms*, *27*(13), 1365-1375.

Coutand, I., D. M. Whipp, D. Grujic, M. Bernet, M. G. Fellin, B. Bookhagen, K. R. Landry, S. K. Ghalley, and C. Duncan (2014), Geometry and kinematics of the Main Himalayan Thrust and Neogene crustal exhumation in the Bhutanese Himalaya derived from inversion of multithermochronologic data, *Journal of Geophysical Research: Solid Earth*, *119*(2), 1446-1481.

Craddock, W. H., D. W. Burbank, B. Bookhagen, and E. J. Gabet (2007), Bedrock channel geometry along an orographic rainfall gradient in the upper Marsyandi River valley in central Nepal, *Journal of Geophysical Research: Earth Surface*, *112*(F3), F03007.

Curray, J. R., and D. G. Moore (1971), Growth of the Bengal Deep-Sea Fan and Denudation in the

Himalayas, *Geological Society of America Bulletin*, *82*(3), 563-572.

Curray, J. R., F. J. Emmel, and D. G. Moore (2002), The Bengal Fan: morphology, geometry, stratigraphy, history and processes, *Marine and Petroleum Geology*, *19*(10), 1191-1223.

Dahal, R. K., and S. Hasegawa (2008), Representative rainfall thresholds for landslides in the Nepal Himalaya, *Geomorphology*, *100*(3–4), 429-443.

Dahlen, F. (1990), Critical taper model of fold-and-thrust belts and accretionary wedges, *Annual Review of Earth and Planetary Sciences*, *18*, 55.

Dahlen, F., J. Suppe, and D. Davis (1984), Mechanics of fold-and-thrust belts and accretionary wedges: Cohesive Coulomb theory, *Journal of Geophysical Research: Solid Earth (1978–2012)*, *89*(B12), 10087-10101.

Dansgaard, W., 1964. Stable isotopes in precipitation. Tellus.

DeCelles, P., G. Gehrels, J. Quade, T. Ojha, P. Kapp, and B. Upreti (1998), Neogene foreland basin deposits, erosional unroofing, and the kinematic history of the Himalayan fold-thrust belt, western Nepal, *Geological Society of America Bulletin*, *110*(1), 2-21.

Desilets, D., and M. Zreda (2001), On scaling cosmogenic nuclide production rates for altitude and latitude using cosmic-ray measurements, *Earth and Planetary Science Letters*, *193*(1–2), 213-225.

Dewey, J. F., and J. M. Bird (1970), Mountain belts and the new global tectonics, *Journal of Geophysical Research*, *75*(14), 2625-2647.

DiBiase, R. A., and K. X. Whipple (2011), The influence of erosion thresholds and runoff variability on the relationships among topography, climate, and erosion rate, *Journal of Geophysical Research: Earth Surface*, *116*(F4), F04036.

DiBiase, R. A., K. X. Whipple, A. M. Heimsath, and W. B. Ouimet (2010), Landscape form and millennial erosion rates in the San Gabriel Mountains, CA, *Earth and Planetary Science Letters*, *289*(1-2), 134-144.

Dietrich, W. E., and J. T. Perron (2006), The search for a topographic signature of life, *Nature*, *439*(7075), 411-418.

DiPietro, J. A., and K. R. Pogue (2004), Tectonostratigraphic subdivisions of the Himalaya: A view from the west, *Tectonics*, *23*(5), n/a-n/a.

Dobremez, J., Shakya, P., 1975. Carte Ecologique du Népal. VI. Region Biratnagar–Kanchenjunga 1: 250, 000. Doc. Cartogr. Ecol. XVI, 33–46.

Douglas, I. (1967), Man, vegetation and the sediment yields of rivers.

Dunai, T. J. (2000), Scaling factors for production rates of in situ produced cosmogenic nuclides: a critical reevaluation, *Earth and Planetary Science Letters*, *176*(1), 157-169.

Dunai, T. J. (2001), Influence of secular variation of the geomagnetic field on production rates of in situ produced cosmogenic nuclides, *Earth and Planetary Science Letters*, *193*(1–2), 197-212.

Dunne, J., D. Elmore, and P. Muzikar (1999), Scaling factors for the rates of production of cosmogenic nuclides for geometric shielding and attenuation at depth on sloped surfaces, *Geomorphology*, *27*(1-2), 3-11.

Dunne, T., D. V. Malmon, and S. M. Mudd (2010), A rain splash transport equation assimilating field and laboratory measurements, *Journal of Geophysical Research: Earth Surface*, *115*(F1), n/a-n/a.

Egholm, D. L., S. B. Nielsen, V. K. Pedersen, and J. E. Lesemann (2009), Glacial effects limiting mountain height, *Nature*, *460*(7257), 884-887.

Ehlers, T. A. (2005), Crustal Thermal Processes and the Interpretation of Thermochronometer Data, *Reviews in Mineralogy and Geochemistry*, *58*(1), 315-350.

Ehlers, T. A., K. A. Farley, M. E. Rusmore, and G. J. Woodsworth (2006), Apatite (U-Th)/He signal of large-magnitude accelerated glacial erosion, southwest British Columbia, *Geology*, *34*(9), 765-768.

Einsele, G., L. Ratschbacher, and A. Wetzel (1996), The Himalaya-Bengal Fan Denudation-Accumulation System during the past 20 Ma, *The Journal of Geology*, *104*(2), 163-184.

Ernst, N., Peterse, F., Breitenbach, S.F.M., Syiemlieh, H.J., Eglinton, T.I., 2013. Biomarkers record environmental changes along an altitudinal transect in the wettest place on Earth. Org. Geochem. 60, 93–99.

Feakins, S.J., Sessions, A.L., 2010. Controls on the D/H ratios of plant leaf waxes in an arid ecosystem. Geochim. Cosmochim. Acta 74, 2128–2141. doi:10.1016/j.gca.2010.01.016

Ferrier, K. L., K. L. Huppert, and J. T. Perron (2013a), Climatic control of bedrock river incision, *Nature*, *496*(7444), 206-209.

Ferrier, K. L., J. T. Perron, S. Mukhopadhyay, M. Rosener, J. D. Stock, K. L. Huppert, and M. Slosberg (2013b), Covariation of climate and long-term erosion rates across a steep rainfall gradient on the Hawaiian island of Kaua'i, *Geological Society of America Bulletin*.

Finnegan, N. J., G. Roe, D. R. Montgomery, and B. Hallet (2005), Controls on the channel width of rivers: Implications for modeling fluvial incision of bedrock, *Geology*, *33*(3), 229-232.

Fisher, G. B., B. Bookhagen, and C. B. Amos (2013), Channel planform geometry and slopes from freely available high-spatial resolution imagery and DEM fusion: Implications for channel width scalings, erosion proxies, and fluvial signatures in tectonically active landscapes, *Geomorphology*, *194*(0), 46-56.

Fisher, G. B., C. B. Amos, B. Bookhagen, D. W. Burbank, and V. Godard (2012), Channel widths, landslides, faults, and beyond: The new world order of high-spatial resolution Google Earth imagery in the study of earth surface processes, *Geological Society of America Special Papers*, *492*, 1-22.

Fleitmann, D., S. J. Burns, M. Mudelsee, U. Neff, J. Kramers, A. Mangini, and A. Matter (2003), Holocene Forcing of the Indian Monsoon Recorded in a Stalagmite from Southern Oman, *Science*, *300*(5626), 1737-1739.

Flint, J. J. (1974), Stream gradient as a function of order, magnitude, and discharge, *Water Resources Research*, *10*, 969-973.

Flohn, H., M. Hantel, and E. Ruprecht (1968), Air-mass dynamics or subsidence processes in the Arabian Sea summer monsoon?, *Journal of the Atmospheric Sciences*, *25*(3), 527-529.

France-Lanord, C., L. Derry, and A. Michard (1993), Evolution of the Himalaya since Miocene time: isotopic and sedimentological evidence from the Bengal Fan, *Geological Society, London, Special Publications*, *74*(1), 603-621.

France-Lanord, C., Derry, L.A., 1997. Organic carbon burial forcing of the carbon cycle from Himalayan erosion. Nature 390, 65–67.

Freeman, K. H., and L. A. Colarusso (2001), Molecular and isotopic records of C4 grassland expansion in the late miocene, *Geochimica et Cosmochimica Acta*, *65*(9), 1439-1454.

Fuchs, G., and M. Linner (1995), Geological traverse across the western Himalaya—a contribution to the geology of eastern Ladakh, Lahul, and Chamba, *Jahrbuch der Geologischen Bundesanstalt*, *138*, 665-685.

Gabet, E. J., D. W. Burbank, J. K. Putkonen, B. A. Pratt-Sitaula, and T. Ojha (2004), Rainfall thresholds for landsliding in the Himalayas of Nepal, *Geomorphology*, *63*(3,Äì4), 131-143.

Gadgil, S. (1988), Recent advances in monsoon research with particular reference to the Indian monsoon, *Aust Meteorol Mag*, *36*, 193-204.

Gadgil, S. (2003), The Indian Monsoon and its variability, *Annual Review of Earth and Planetary Sciences*, *31*(1), 429-467.

Galy, V., Eglinton, T., 2011. Protracted storage of biospheric carbon in the Ganges–Brahmaputra basin. Nat. Geosci. 4, 843–847. doi:10.1038/ngeo1293

Galy, V., Eglinton, T., France-Lanord, C., Sylva, S., 2011. The provenance of vegetation and environmental signatures encoded in vascular plant biomarkers carried by the Ganges–Brahmaputra rivers. Earth Planet. Sci. Lett. 304, 1–12. doi:10.1016/j.epsl.2011.02.003

Galy, V., Peucker-Ehrenbrink, B., Eglinton, T., 2015. Global carbon export from the terrestrial biosphere controlled by erosion. Nature 521, 204–207. doi:10.1038/nature14400

Gansser, A. (1964), Geology of the Himalayas.

Gansser, A. (1980), The significance of the Himalayan suture zone, *Tectonophysics*, *62*(1), 37-52.

Gansser, A. (1983), Geology of the Bhutan Himalaya, 181 pp, *Denkschr. Schweiz. Naturforsch. Ges*, *96*.

Garcin, Y., Schwab, V.F., Gleixner, G., Kahmen, A., Todou, G., Séné, O., Onana, J.-M., Achoundong, G., Sachse, D., 2012. Hydrogen isotope ratios of lacustrine sedimentary n-alkanes as proxies of tropical African hydrology: insights from a calibration transect across Cameroon. Geochim. Cosmochim. Acta 79, 106–126. doi:10.1016/j.gca.2011.11.039

Garzanti, E. (1993), Sedimentary evoiution and drowning of a passive margin shelf (Giumai Gronp; Zanskar Tethys Himalaya, Endia): palaeoenvironinental changes dnring final break-np of Gondwanaiand.

Garzanti, E. (1999), Stratigraphy and sedimentary history of the Nepal Tethys Himalaya passive margin, *Journal of Asian Earth Sciences*, *17*(5–6), 805-827.

Garzione, C.N., Quade, J., DeCelles, P.G., English, N.B., 2000. Predicting paleoelevation of Tibet and the Himalaya from δ18O vs. altitude gradients in meteoric water across the Nepal Himalaya. Earth Planet. Sci. Lett. 183, 215–229. doi:10.1016/S0012-821X(00)00252-1

GLIMS, and National Snow and Ice Data Center. 2005, updated 2012. *GLIMS Glacier Database*. Boulder, Colorado USA: National Snow and Ice Data Center. http://dx.doi.org/10.7265/N5V98602.

Glotzbach, C., M. Röttjer, A. Hampel, R. Hetzel, and P. W. Kubik (2013), Quantifying the impact of former glaciation on catchment-wide denudation rates derived from cosmogenic 10Be, *Terra Nova*.

Godard, V., R. Cattin, and J. Lavé (2004), Numerical modeling of mountain building: Interplay between erosion law and crustal rheology, *Geophysical Research Letters*, *31*(23).

Godard, V., D. W. Burbank, D. L. Bourlès, B. Bookhagen, R. Braucher, and G. B. Fisher (2012), Impact of glacial erosion on 10Be concentrations in fluvial sediments of the Marsyandi catchment, central Nepal, *Journal of Geophysical Research: Earth Surface*, *117*(F3), F03013.

Godard, V., D. L. Bourlés, F. Spinabella, D. W. Burbank, B. Bookhagen, G. B. Fisher, A. Moulin, and L. Léanni (2014), Dominance of tectonics over climate in Himalayan denudation, *Geology*.

Gonfiantini, R., Roche, M.A., Olivry, J.C., Fontes, J.C., Zuppi, G.M., 2001. The altitude effect on the isotopic composition of tropical rains. Chem. Geol. 181, 147–167. doi:10.1016/S0009-2541(01)00279-0

Goñi, M., Ruttenberg, K., Eglinton, T., 1997. Sources and contribution of terrigenous organic carbon to surface sediments in the Gulf of Mexico. Nature 389, 275–278.

Goñi, M., Yunker, M., Macdonald, R., Eglinton, T., 2000. Distribution and sources of organic biomarkers in

arctic sediments from the Mackenzie River and Beaufort Shelf. Mar. Chem.

Goodbred, S. L., and S. A. Kuehl (2000), Enormous Ganges-Brahmaputra sediment discharge during strengthened early Holocene monsoon, *Geology*, *28*(12), 1083-1086.

Granger, D. E., J. W. Kirchner, and R. Finkel (1996), Spatially Averaged Long-Term Erosion Rates Measured from in Situ-Produced Cosmogenic Nuclides in Alluvial Sediment, *The Journal of Geology*, *104*(3), 249-257.

Granger, D. E., N. A. Lifton, and J. K. Willenbring (2013), A cosmic trip: 25 years of cosmogenic nuclides in geology, *Geological Society of America Bulletin*, *125*(9-10), 1379-1402.

Grujic, D., C. J. Warren, and J. L. Wooden (2011), Rapid synconvergent exhumation of Miocene-aged lower orogenic crust in the eastern Himalaya, *Lithosphere*, *3*(5), 346-366.

Gyssels, G., and J. Poesen (2003), The importance of plant root characteristics in controlling concentrated flow erosion rates, *Earth Surface Processes and Landforms*, *28*(4), 371-384.

Hales, T. C., and J. J. Roering (2005), Climate-controlled variations in scree production, Southern Alps, New Zealand, *Geology*, *33*(9), 701-704.

Hales, T. C., and J. J. Roering (2007), Climatic controls on frost cracking and implications for the evolution of bedrock landscapes, *Journal of Geophysical Research: Earth Surface*, *112*(F2), F02033.

Harvey, J. E., D. W. Burbank, and B. Bookhagen (2015), Along-strike changes in Himalayan thrust geometry: Topographic and tectonic discontinuities in western Nepal, *Lithosphere*, L444. 441.

Hedges, J., Clark, W., Quay, P., Richey, J., Devol, A., de M. Santos, U., 1986. Compositions and fluxes of particulate organic material in the Amazon River. Limnol. … 31, 717–738.

Hedges, J.I., Cowie, G., Richey, J.E., Quay, P.D., Benner, R., Strom, M., Forsberg, B.R., 1994. Origins and processing of organic matter in the Amazon River as indicated by carbohydrates and amino acids. Limnol. … 39, 743–761.

Hedges, J.I., Mayorga, E., Tsamakis, E., McClain, M.E., Aufdenkampe, A., Quay, P., Richey, J.E., Benner, R., Opsahl, S., Black, B., Pimentel, T., Quintanilla, J., Maurice, L., 2000. Organic matter in Bolivian tributaries of the Amazon River: A comparison to the lower mainstream. Limnol. Oceanogr. 45, 1449–1466. doi:10.4319/lo.2000.45.7.1449

Heim, A., and A. Gansser Central Himalaya Geological Observations of Swiss, 1939 (reprinted 1975), edited, Hindustan Publishing Corporation, Delhi.

Heimsath, A. M., and R. McGlynn (2008), Quantifying periglacial erosion in the Nepal high Himalaya, *Geomorphology*, *97*(1), 5-23.

Herman, F., D. Seward, P. G. Valla, A. Carter, B. Kohn, S. D. Willett, and T. A. Ehlers (2013), Worldwide acceleration of mountain erosion under a cooling climate, *Nature*, *504*(7480), 423-426.

Herman, F., et al. (2010), Exhumation, crustal deformation, and thermal structure of the Nepal Himalaya derived from the inversion of thermochronological and thermobarometric data and modeling of the topography, *Journal of Geophysical Research: Solid Earth*, *115*(B6), B06407.

Hirschmiller, J., D. Grujic, B. Bookhagen, I. Coutand, P. Huyghe, J.-L. Mugnier, and T. Ojha (2014), What controls the growth of the Himalayan foreland fold-and-thrust belt?, *Geology*.

Hodges, K. V. (2000), Tectonics of the Himalaya and southern Tibet from two perspectives, *Geological Society of America Bulletin*, *112*(3), 324-350.

Hodges, K. V., J. Hurtado, and K. X. Whipple (2001), Southward extrusion of Tibetan crust and its effect on Himalayan tectonics, *Tectonics*, *20*(6), 799-809.

Hodges, K. V., C. Wobus, K. Ruhl, T. Schildgen, and K. Whipple (2004), Quaternary deformation, river steepening, and heavy precipitation at the front of the Higher Himalayan ranges, *Earth and Planetary Science Letters*, *220*(3-4), 379-389.

Hoffmann, B., Kahmen, A., Cernusak, L.A., Arndt, S.K., Sachse, D., 2013. Abundance and distribution of leaf wax n-alkanes in leaves of acacia and eucalyptus trees along a strong humidity gradient in Northern Australia. Org. Geochem. 62, 62–67.

Horton, R. E. (1945), Erosional development of streams and their drainage basins; Hydrophysical approach to quantitative morphology, *Geological Society of America Bulletin*, *56*(3), 275-370.

Hou, J., Dandrea, W., Macdonald, D., Huang, Y., 2007. Hydrogen isotopic variability in leaf waxes among terrestrial and aquatic plants around Blood Pond, Massachusetts (USA). Org. Geochem. 38, 977–984. doi:10.1016/j.orggeochem.2006.12.009

Hren, M.T., Bookhagen, B., Blisniuk, P.M., Booth, A.L., Chamberlain, C.P., 2009. d18O and dD of streamwaters across the Himalaya and Tibetan Plateau: Implications for moisture sources and paleoelevation reconstructions. Earth Planet. Sci. Lett. 288, 20–32. doi:DOI: 10.1016/j.epsl.2009.08.041

Huang, Y., Shuman, B., Wang, Y., Iii, T.W., 2004. Hydrogen isotope ratios of individual lipids in lake sediments as novel tracers of climatic and environmental change : a surface sediment test 363–375.

Hubbard, M. S., and T. M. Harrison (1989), 40Ar/39Ar age constraints on deformation and metamorphism in the main central thrust zone and Tibetan slab, eastern Nepal Himalaya, *Tectonics*, *8*(4), 865-880.

Huete, A. R., C. O. Justice, and H. Liu (1994), Development of vegetation and soil indices for MODIS-EOS, *Remote Sensing of Environment*, *49*(3), 224-234.

Huete, A. R., C. O. Justice, and J. W. D. van Leeuwen (1999), MODIS Vegetation Index, Algorithm

Theoretical Basis Document, http://modarch.gsfc.nasa.gov/MODIS/ATBD/atbd_mod13.pdf.

Huffman, G.J., Bolvin, D.T., Nelkin, E.J., Wolff, D.B., Adler, R.F., Gu, G., Hong, Y., Bowman, K.P., Stocker, E.F., 2007. The TRMM Multisatellite Precipitation Analysis (TMPA): Quasi-Global, Multiyear, Combined-Sensor Precipitation Estimates at Fine Scales. J. Hydrometeorol. 8, 38–55. doi:10.1175/JHM560.1

Huntington, K. W., A. E. Blythe, and K. V. Hodges (2006), Climate change and Late Pliocene acceleration of erosion in the Himalaya, *Earth and Planetary Science Letters*, *252*(1-2), 107-118.

Istanbulluoglu, E., and R. L. Bras (2005), Vegetation-modulated landscape evolution: Effects of vegetation on landscape processes, drainage density, and topography, *Journal of Geophysical Research: Earth Surface*, *110*(F2), F02012.

Istanbulluoglu, E., D. G. Tarboton, R. T. Pack, and C. H. Luce (2004), Modeling of the interactions between forest vegetation, disturbances, and sediment yields, *Journal of Geophysical Research: Earth Surface*, *109*(F1), F01009.

Iwata, S., H. Yamanaka, and M. Yoshida (1982), Glacial landforms and river terraces in the Thakkhola region, central Nepal, *Journal of Nepal Geological Society*, *2*(Special Issue), 81-94.

Jackson, M., and R. Bilham (1994), Constraints on Himalayan deformation inferred from vertical velocity fields in Nepal and Tibet, *Journal of Geophysical Research: Solid Earth*, *99*(B7), 13897-13912.

Jarvis, A., H. I. Reuter, A. Nelson, and E. Guevara (2008), Hole-filled SRTM for the globe Version 4, available from the CGIAR-CSI SRTM 90m Database (http://srtm.csi.cgiar.org).

Jeffery, M. L., B. J. Yanites, C. J. Poulsen, and T. A. Ehlers (2014), Vegetation-precipitation controls on Central Andean topography, *Journal of Geophysical Research: Earth Surface*, 2013JF002919.

Jia, G., Wei, K., Chen, F., Peng, P., 2008. Soil n-alkane δD vs. altitude gradients along Mount Gongga, China. Geochim. Cosmochim. Acta 72, 5165–5174. doi:10.1016/j.gca.2008.08.004

Justice, C. O., E. Vermote, J. R. Townshend, R. Defries, D. P. Roy, D. K. Hall, V. V. Salomonson, J. L. Privette, G. Riggs, and A. Strahler (1998), The Moderate Resolution Imaging Spectroradiometer (MODIS): Land remote sensing for global change research, *Geoscience and Remote Sensing, IEEE Transactions on*, *36*(4), 1228-1249.

Kahmen, A., Hoffmann, B., Schefuß, E., Arndt, S.K., Cernusak, L.A., West, J.B., Sachse, D., 2013a. Leaf water deuterium enrichment shapes leaf wax n-alkane dD values of angiosperm plants II: Observational evidence and global implications. Geochim. Cosmochim. Acta 111, 50–63. doi:10.1016/j.gca.2012.09.004

Kahmen, A., Schefuß, E., Sachse, D., 2013b. Leaf water deuterium enrichment shapes leaf wax n-alkane dD values of angiosperm plants I: Experimental evidence and mechanistic insights. Geochim. Cosmochim. Acta 111, 39–49. doi:10.1016/j.gca.2012.09.003

Kim, J., Zell, C., Moreira-turcq, P., Pe, M.A.P., Mortillaro, J., Weijers, J.W.H., Meziane, T., 2012. Tracing soil organic carbon in the lower Amazon River and its tributaries using GDGT distributions and bulk organic matter properties 90, 163–180. doi:10.1016/j.gca.2012.05.014

Kirby, E., and K. Whipple (2001), Quantifying differential rock-uplift rates via stream profile analysis, *Geology*, *29*(5), 415-418.

Kirby, E., and K. X. Whipple (2012), Expression of active tectonics in erosional landscapes, *Journal of Structural Geology*, *44*(0), 54-75.

Kirchner, J. W., R. C. Finkel, C. S. Riebe, D. E. Granger, J. L. Clayton, J. G. King, and W. F. Megahan (2001), Mountain erosion over 10 yr, 10 k.y., and 10 m.y. time scales, *Geology*, *29*(7), 591-594.

Klein, J., R. Giegengack, R. Middleton, P. Sharma, J. Underwood, and R. Weeks (1986), Revealing histories of exposure using in situ produced 26Al and 10Be in Libyan desert glass, *Radiocarbon*, *28*(2A), 547-555.

Knighton, A. D. (1999), Downstream variation in stream power, *Geomorphology*, *29*(3,Äì4), 293-306.

Korschinek, G., et al. (2010), A new value for the half-life of 10Be by Heavy-Ion Elastic Recoil Detection and liquid scintillation counting, *Nuclear Instruments and Methods in Physics Research Section B: Beam Interactions with Materials and Atoms*, *268*(2), 187-191.

Krynine, P. D. (1936), Geomorphology and sedimentation in the humid tropics, *American Journal of Science*(190), 297-306.

Lague, D. (2014), The stream power river incision model: evidence, theory and beyond, *Earth Surface Processes and Landforms*, *39*(1), 38-61.

Lague, D., N. Hovius, and P. Davy (2005), Discharge, discharge variability, and the bedrock channel profile, *Journal of Geophysical Research: Earth Surface*, *110*(F4), F04006.

Lal, D. (1991), Cosmic ray labeling of erosion surfaces: in situ nuclide production rates and erosion models, *Earth and Planetary Science Letters*, *104*(2-4), 424-439.

Lal, D., and J. R. Arnold (1985), Tracing quartz through the environment, *Proc. Indian Acad. Sci. (Earth Planet Sci.)*, *94*(1), 1-5.

Lamb, M. P., M. Levina, R. A. DiBiase, and B. M. Fuller (2013), Sediment storage by vegetation in steep bedrock landscapes: Theory, experiments, and implications for postfire sediment yield, *Journal of Geophysical Research: Earth Surface*, *118*(2), 1147-1160.

Lamb, M. P., J. S. Scheingross, W. H. Amidon, E. Swanson, and A. Limaye (2011), A model for fire-

induced sediment yield by dry ravel in steep landscapes, *Journal of Geophysical Research: Earth Surface*, *116*(F3).

Lang, T.J., Barros, A.P., 2004. Winter Storms in the Central Himalayas 82, 829–844.

Langbein, W., and S. Schumm (1958), Yield of sediment in relation to mean annual precipitation, *American Geophysical Union Transactions*, *39*, 1076-1084.

Lavé, J., and J. P. Avouac (2001), Fluvial incision and tectonic uplift across the Himalayas of central Nepal, *Journal of Geophysical Research: Solid Earth*, *106*(B11), 26561-26591.

Le Fort, P. (1975), Himalayas: the collided range. Present knowledge of the continental arc, *American Journal of Science*, *275*(1), 44.

Le Roux-Mallouf, R., et al. (2015), Evidence for a wide and gently dipping Main Himalayan Thrust in western Bhutan, *Geophysical Research Letters*, *42*(9), 3257-3265.

Lilliefors, H. W. (1967), On the Kolmogorov-Smirnov test for normality with mean and variance unknown, *Journal of the American Statistical Association*, *62*, 399-402.

Lilliefors, H. W. (1969), On the Kolmogorov-Smirnov test for the exponential distribution with mean unknown, *Journal of the American Statistical Association*, *64*, 387-389.

Lupker, M., P.-H. Blard, J. Lavé, C. France-Lanord, L. Leanni, N. Puchol, J. Charreau, and D. Bourl√®s (2012), 10Be-derived Himalayan denudation rates and sediment budgets in the Ganga basin, *Earth and Planetary Science Letters*, *333*‚Äì*334*(0), 146-156.

Masarik, J., M. Frank, J. M. Schäfer, and R. Wieler (2001), Correction of in situ cosmogenic nuclide production rates for geomagnetic field intensity variations during the past 800,000 years, *Geochimica et Cosmochimica Acta*, *65*(17), 2995-3003.

McPhillips, D., P. R. Bierman, and D. H. Rood (2014), Millennial-scale record of landslides in the Andes consistent with earthquake trigger, *Nature Geosci*, *7*(12), 925-930.

McPhillips, D., P. R. Bierman, T. Crocker, and D. H. Rood (2013), Landscape response to Pleistocene-Holocene precipitation change in the Western Cordillera, Peru: 10Be concentrations in modern sediments and terrace fills, *Journal of Geophysical Research: Earth Surface*, *118*(4), 2013JF002837.

Meier, K., and E. Hiltner (1993), Deformation and metamorphism within the Main Central Thrust zone, Arun Tectonic Window, eastern Nepal, *Geological Society, London, Special Publications*, *74*(1), 511-523.

Milliman, J. D., and J. D. M. Syvitski (1992), Geomorphic/tectonic control of sediment discharge to the ocean: The importance of small mountainous rivers, *J. Geol.*, *100*, 525-544.

Milliman, J. D., G. Quraishee, and M. Beg (1984), Sediment discharge from the Indus River to the ocean: past, present and future, *Marine geology and oceanography of Arabian Sea and coastal Pakistan*, 65-70.

Molnar, P., and P. Tapponnier (1975), Cenozoic Tectonics of Asia: Effects of a Continental Collision: Features of recent continental tectonics in Asia can be interpreted as results of the India-Eurasia collision, *Science*, *189*(4201), 419-426.

Molnar, P., and P. England (1990), Late Cenozoic uplift of mountain ranges and global climate change: chicken or egg?, *Nature*, *346*(6279), 29-34.

Molnar, P., Boos, W. R., & Battisti, D. S. (2010), Orographic controls on climate and paleoclimate of Asia: thermal and mechanical roles for the Tibetan Plateau, *Annual Review of Earth and Planetary Sciences*, *38*(1), 77.

Monteith, J. (1965), Evaporation and environment, paper presented at Symp. Soc. Exp. Biol.

Montgomery, D. R. (2001), Slope Distributions, Threshold Hillslopes, and Steady-state Topography, *American Journal of Science*, *301*(4-5), 432-454.

Montgomery, D. R., and D. B. Stolar (2006), Reconsidering Himalayan river anticlines, *Geomorphology*, *82*(1-2), 4-15.

Montgomery, D. R., and D. B. Stolar (2006), Reconsidering Himalayan river anticlines, *Geomorphology*, *82*(1-2), 4-15.

Moody, J. A., R. A. Shakesby, P. R. Robichaud, S. H. Cannon, and D. A. Martin (2013), Current research issues related to post-wildfire runoff and erosion processes, *Earth-Science Reviews*, *122*, 10-37.

Moon, S., C. Page Chamberlain, K. Blisniuk, N. Levine, D. H. Rood, and G. E. Hilley (2011), Climatic control of denudation in the deglaciated landscape of the Washington Cascades, *Nature Geosci*, *4*(7), 469-473.

Moore, G. F., J. R. Curray, and F. J. Emmel (1982), Sedimentation in the Sunda Trench and forearc region, *Geological Society, London, Special Publications*, *10*(1), 245-258.

Morell, K. D., M. Sandiford, C. Rajendran, K. Rajendran, A. Alimanovic, D. Fink, and J. Sanwal (2015), Geomorphology reveals active décollement geometry in the central Himalayan seismic gap, *Lithosphere*, *7*(3), 247-256.

Morgan, R. P. C. (1978), Field studies of rainsplash erosion, *Earth Surface Processes*, *3*(3), 295-299.

Mu, Q., M. Zhao, and S. W. Running (2011), Improvements to a MODIS global terrestrial evapotranspiration algorithm, *Remote Sensing of Environment*, *115*(8), 1781-1800.

Mu, Q., F. A. Heinsch, M. Zhao, and S. W. Running (2007), Development of a global evapotranspiration

algorithm based on MODIS and global meteorology data, *Remote Sensing of Environment*, *111*(4), 519-536.

Niemi, N. A., M. Oskin, D. W. Burbank, A. M. Heimsath, and E. J. Gabet (2005), Effects of bedrock landslides on cosmogenically determined erosion rates, *Earth and Planetary Science Letters*, *237*(3-4), 480-498.

Nishiizumi, K., D. Elmore, X. Z. Ma, and J. R. Arnold (1984), 10Be and36Cl depth profiles in an Apollo 15 drill core, *Earth and Planetary Science Letters*, *70*(2), 157-163.

Nishiizumi, K., M. Imamura, M. W. Caffee, J. R. Southon, R. C. Finkel, and J. McAninch (2007), Absolute calibration of 10Be AMS standards, *Nuclear Instruments and Methods in Physics Research Section B: Beam Interactions with Materials and Atoms*, *258*(2), 403-413.

Noble, C. A., and R. P. C. Morgan (1983), Rainfall interception and splash detachment with a Brussels sprouts plant: A laboratory simulation, *Earth Surface Processes and Landforms*, *8*(6), 569-577.

Oberlander, T. (1985), Origin of drainage transverse to structures in orogens.

Olen, S. M., B. Bookhagen, B. Hoffmann, D. Sachse, D. P. Adhikari, and M. R. Strecker (2015), Understanding erosion rates in the Himalayan orogen: A case study from the Arun Valley, *Journal of Geophysical Research: Earth Surface*, n/a-n/a.

Osterkamp, W. R., C. R. Hupp, and M. Stoffel (2012), The interactions between vegetation and erosion: new directions for research at the interface of ecology and geomorphology, *Earth Surface Processes and Landforms*, *37*(1), 23-36.

Ouimet, W. B., K. X. Whipple, and D. E. Granger (2009), Beyond threshold hillslopes: Channel adjustment to base-level fall in tectonically active mountain ranges, *Geology*, *37*(7), 579-582.

Parker, R. N., A. L. Densmore, N. J. Rosser, M. de Michele, Y. Li, R. Huang, S. Whadcoat, and D. N. Petley (2011), Mass wasting triggered by the 2008 Wenchuan earthquake is greater than orogenic growth, *Nature Geosci*, *4*(7), 449-452.

Perron, J. T., Royden, L. (2013), An integral approach to bedrock river profile analysis, *Earth Surface Processes and Landforms*, *38*(6), 570-576.

Peterse, F., Meer, M.T.J. Van Der, Schouten, S., Jia, G., Ossebaar, J., Blokker, J., Damst, J.S.S., 2009. Assessment of soil n-alkane δD and branched tetraether membrane lipid distributions as tools for paleoelevation reconstruction 2799–2807.

Polissar, P.J., Freeman, K.H., 2010. Effects of aridity and vegetation on plant-wax d D in modern lake sediments. Geochim. Cosmochim. Acta 74, 5785–5797. doi:10.1016/j.gca.2010.06.018

Ponton, C., West, a. J., Feakins, S.J., Galy, V., 2014. Leaf wax biomarkers in transit record river catchment composition. Geophys. Res. Lett. 41, 6420–6427. doi:10.1002/2014GL061328

Portenga, E. W., P. R. Bierman, C. Duncan, L. B. Corbett, N. M. Kehrwald, and D. H. Rood (2015), Erosion rates of the Bhutanese Himalaya determined using in situ-produced 10Be, *Geomorphology*, *233*, 112-126.

Prins, M. A., and G. Postma (2000), Effects of climate, sea level, and tectonics unraveled for last deglaciation turbidite records of the Arabian Sea, *Geology*, *28*(4), 375-378.

Prosser, I. P., and W. E. Dietrich (1995), Field Experiments on Erosion by Overland Flow and Their Implication for a Digital Terrain Model of Channel Initiation, *Water Resources Research*, *31*(11), 2867-2876.

Prosser, I. P., and M. Soufi (1998), Controls on gully formation following forest clearing in a humid temperate environment, *Water Resources Research*, *34*(12), 3661-3671.

Puchol, N., J. Lavé, M. Lupker, P.-H. Blard, F. Gallo, and C. France-Lanord (2014), Grain-size dependent concentration of cosmogenic 10Be and erosion dynamics in a landslide-dominated Himalayan watershed, *Geomorphology*, *224*(0), 55-68.

Raymo, M. E., and W. F. Ruddiman (1992), Tectonic forcing of late Cenozoic climate, *Nature*, *359*(6391), 117-122.

Raymo, M. E., W. F. Ruddiman, and P. N. Froelich (1988), Influence of late Cenozoic mountain building on ocean geochemical cycles, *Geology*, *16*(7), 649-653.

Reiners, P. W., T. A. Ehlers, S. G. Mitchell, and D. R. Montgomery (2003), Coupled spatial variations in precipitation and long-term erosion rates across the Washington Cascades, *Nature*, *426*(6967), 645-647.

Riebe, C. S., J. W. Kirchner, and R. C. Finkel (2004), Erosional and climatic effects on long-term chemical weathering rates in granitic landscapes spanning diverse climate regimes, *Earth and Planetary Science Letters*, *224*(3-4), 547-562.

Riebe, C. S., J. W. Kirchner, D. E. Granger, and R. C. Finkel (2001), Strong tectonic and weak climatic control of long-term chemical weathering rates, *Geology*, *29*(6), 511-514.

Robert, X., P. van der Beek, J. Braun, C. Perry, M. Dubille, and J.-L. Mugnier (2009), Assessing Quaternary reactivation of the Main Central thrust zone (central Nepal Himalaya): New thermochronologic data and numerical modeling, *Geology*, *37*(8), 731-734.

Roe, G. H., D. R. Montgomery, and B. Hallet (2002), Effects of orographic precipitation variations on the concavity of steady-state river profiles, *Geology*, *30*(2), 143-146.

Roe, G. H., K. X. Whipple, and J. K. Fletcher (2008), Feedbacks among climate, erosion, and tectonics in a critical wedge orogen, *American Journal of Science*, *308*(7), 815-842.

Rogers, R., and S. Schumm (1991), The effect of sparse vegetative cover on erosion and sediment yield, *Journal of Hydrology*, *123*(1), 19-24.

Rowley, D.B., Pierrehumbert, R.T., Currie, B.S., 2001. A new approach to stable isotope-based paleoaltimetry: Implications for paleoaltimetry and paleohypsometry of the High Himalaya since the late Miocene. Earth Planet. Sci. Lett. 188, 253–268. doi:10.1016/S0012-821X(01)00324-7

Royden, L., and J. T. Perron (2013), Solutions of the stream power equation and application to the evolution of river longitudinal profiles, *Journal of Geophysical Research: Earth Surface*, *118*(2), 497-518.

Sachse, D., Radke, J., Gleixner, G., 2004. Hydrogen isotope ratios of recent lacustrine sedimentary n-alkanes record modern climate variability. Geochim. Cosmochim. Acta 68, 4877–4889. doi:10.1016/j.gca.2004.06.004

Sachse, D., Radke, J., Gleixner, G., 2006. δD values of individual n-alkanes from terrestrial plants along a climatic gradient – Implications for the sedimentary biomarker record. Org. Geochem. 37, 469–483. doi:10.1016/j.orggeochem.2005.12.003

Sachse, D., I. Billault, G. J. Bowen, Y. Chikaraishi, T. E. Dawson, S. J. Feakins, K. H. Freeman, C. R. Magill, F. A. McInerney, and M. T. Van der Meer (2012), Molecular paleohydrology: interpreting the hydrogen-isotopic composition of lipid biomarkers from photosynthesizing organisms.

Safran, E. B., P. R. Bierman, R. Aalto, T. Dunne, K. X. Whipple, and M. Caffee (2005), Erosion rates driven by channel network incision in the Bolivian Andes, *Earth Surface Processes and Landforms*, *30*(8), 1007-1024.

Schäfer, J., Blanc, G., Lapaquellerie, Y., Maillet, N., Maneux, E., Etcheber, H., 2002. Ten-year observation of the Gironde tributary fluvial system: Fluxes of suspended matter, particulate organic carbon and cadmium. Mar. Chem. 79, 229–242.

Schefuß, E., 2003. Carbon isotope analyses of n-alkanes in dust from the lower atmosphere over the central eastern Atlantic. Geochim. Cosmochim. Acta 67, 1757–1767. doi:10.1016/S0016-7037(02)01414-X

Schelling, D. (1992), The tectonostratigraphy and structure of the eastern Nepal Himalaya, *Tectonics*, *11*(5), 925-943.

Schelling, D., and K. Arita (1991), Thrust tectonics, crustal shortening, and the structure of the far-eastern Nepal Himalaya, *Tectonics*, *10*(5), 851-862.

Scherler, D., B. Bookhagen, and M. R. Strecker (2014), Tectonic control on 10Be-derived erosion rates in the Garhwal Himalaya, India, *Journal of Geophysical Research: Earth Surface*, 2013JF002955.

Scherler, D., B. Bookhagen, H. Wulf, F. Preusser, and M. R. Strecker (2015), Increased late Pleistocene erosion rates during fluvial aggradation in the Garhwal Himalaya, northern India, *Earth and Planetary Science Letters*, *428*, 255-266.

Schulte-Pelkum, V., G. Monsalve, A. Sheehan, M. R. Pandey, S. Sapkota, R. Bilham, and F. Wu (2005), Imaging the Indian subcontinent beneath the Himalaya, *Nature*, *435*(7046), 1222-1225.

Schwanghart, W., Kuhn, N.J., 2010. TopoToolbox: A set of Matlab functions for topographic analysis. Environ. Model. Softw. 25, 770–781. doi:10.1016/j.envsoft.2009.12.002

Schwanghart, W., and D. Scherler (2013), Short Communication: TopoToolbox 2: an efficient and user-friendly tool for Earth surface sciences, *Earth Surf. Dynam. Discuss.*, *1*(1), 261-275.

Schwanghart, W., G. Groom, N. J. Kuhn, and G. Heckrath (2013), Flow network derivation from a high resolution DEM in a low relief, agrarian landscape, *Earth Surface Processes and Landforms*, *38*(13), 1576-1586.

Searle, M. P., R. L. Simspon, R. D. Law, R. R. Parrish, and D. J. Waters (2003), The structural geometry, metamorphic and magmatic evolution of the Everest massif, High Himalaya of Nepal–South Tibet, *Journal of the Geological Society*, *160*(3), 345-366.

Seeber, L., and V. Gornitz (1983), River profiles along the Himalayan arc as indicators of active Tectonics, *Tectonophysics*, *92*(355-467).

Seong, Y. B., L. A. Owen, M. W. Caffee, U. Kamp, M. P. Bishop, A. Bush, L. Copland, and J. F. Shroder (2009), Rates of basin-wide rockwall retreat in the K2 region of the Central Karakoram defined by terrestrial cosmogenic nuclide 10 Be, *Geomorphology*, *107*(3), 254-262.

Singh, P., K. Ramasatri, N. Kumar, and N. Bhatnagar (2003), Suspended sediment transport from the Dokriani Glacier in the Garhwal Himalayas, *Nordic hydrology*, *34*(3), 221-244.

Sklar, L. S., and W. E. Dietrich (2004), A mechanistic model for river incision into bedrock by saltating bed load, *Water Resources Research*, *40*(6), W06301.

Sklar, L. S., W. E. Dietrich, E. Foufoula-Georgiou, B. Lashermes, and D. Bellugi (2006), Do gravel bed river size distributions record channel network structure?, *Water Resources Research*, *42*(6), W06D18.

Snyder, N. P., K. X. Whipple, G. E. Tucker, and D. J. Merritts (2000), Landscape response to tectonic forcing: Digital elevation model analysis of stream profiles in the Mendocino triple junction region, northern California, *Geological Society of America Bulletin*, *112*(8), 1250-1263.

Snyder, N. P., K. X. Whipple, G. E. Tucker, and D. J. Merritts (2003a), Channel response to tectonic forcing: field analysis of stream morphology and hydrology in the Mendocino triple junction region, northern California, *Geomorphology*, *53*(1–2), 97-127.

Snyder, N. P., K. X. Whipple, G. E. Tucker, and D. J. Merritts (2003b), Importance of a stochastic distribution of floods and erosion thresholds in the bedrock river incision problem, *Journal of Geophysical Research: Solid Earth (1978–2012)*, *108*(B2).

Stöcklin, J. (1980), Geology of Nepal and its regional frame: Thirty-third William Smith Lecture, *Journal of the Geological Society*, *137*(1), 1-34.

Stone, J. O. (2000), Air pressure and cosmogenic isotope production, *Journal of Geophysical Research*, *105*(B10), 23,753-723,759.

Tao, S., Eglinton, T.I., Montluçon, D.B., McIntyre, C., Zhao, M., 2015. Pre-aged soil organic carbon as a major component of the Yellow River suspended load: Regional significance and global relevance. Earth Planet. Sci. Lett. 414, 77–86. doi:10.1016/j.epsl.2015.01.004

Tierney, J.E., Russell, J.M., Huang, Y., Damsté, J.S.S., Hopmans, E.C., Cohen, A.S., 2008. Northern hemisphere controls on tropical southeast African climate during the past 60,000 years. Science 322, 252–255.

Tipple, B.J., Pagani, M., 2012. Environmental control on eastern broadleaf forest species' leaf wax distributions and D/H ratios. Geochim. Cosmochim. Acta 111, 64–77. doi:10.1016/j.gca.2012.10.042

Thamban, M., V. Purnachandra Rao, and R. R. Schneider (2002), Reconstruction of late Quaternary monsoon oscillations based on clay mineral proxies using sediment cores from the western margin of India, *Marine Geology*, *186*(3-4), 527-539.

Thiede, R. C., and T. A. Ehlers (2013), Large spatial and temporal variations in Himalayan denudation, *Earth and Planetary Science Letters*, *371*,Äì*372*(0), 278-293.

Thiede, R. C., B. Bookhagen, J. R. Arrowsmith, E. R. Sobel, and M. R. Strecker (2004), Climatic control on rapid exhumation along the Southern Himalayan Front, *Earth and Planetary Science Letters*, *222*(3-4), 791-806.

Thiede, R. C., J. R. Arrowsmith, B. Bookhagen, M. O. McWilliams, E. R. Sobel, and M. R. Strecker (2005), From tectonically to erosionally controlled development of the Himalayan orogen, *Geology*, *33*(8), 689-692.

Torres Acosta, V., T. F. Schildgen, B. A. Clarke, D. Scherler, B. Bookhagen, H. Wittmann, F. von Blanckenburg, and M. R. Strecker (2015), Effect of vegetation cover on millennial-scale landscape denudation rates in East Africa, *Lithosphere*.

Tucker, G. E., and R. Slingerland (1997), Drainage basin responses to climate change, *Water Resources Research*, *33*(8), 2031-2047.

USGS, 2006. Shuttle Radar Topography Mission, 3 Arc Second scene. Global Land Cover Facility, University of Maryland, College Park, Maryland.

Valdiya, K. S. (1980), *Geology of kumaun lesser himalaya*, Wadia Institute of Himalayan Geology.

van der Beek, P., X. Robert, J.-L. Mugnier, M. Bernet, P. Huyghe, and E. Labrin (2006), Late Miocene – Recent exhumation of the central Himalaya and recycling in the foreland basin assessed by apatite fission-track thermochronology of Siwalik sediments, Nepal, *Basin Research*, *18*(4), 413-434.

Vance, D., M. Bickle, S. Ivy-Ochs, and P. W. Kubik (2003), Erosion and exhumation in the Himalaya from cosmogenic isotope inventories of river sediments, *Earth and Planetary Science Letters*, *206*(3-4), 273-288.

von Blanckenburg, F. (2005), The control mechanisms of erosion and weathering at basin scale from cosmogenic nuclides in river sediment, *Earth and Planetary Science Letters*, *237*(3-4), 462-479.

von Blanckenburg, F., T. Hewawasam, and P. W. Kubik (2004), Cosmogenic nuclide evidence for low weathering and denudation in the wet, tropical highlands of Sri Lanka, *Journal of Geophysical Research: Earth Surface*, *109*(F3), F03008.

Wager, L. R. (1937), The Arun River Drainage Pattern and the Rise of the Himalaya, *The Geographical Journal*, *89*(3), 239-250.

Wainwright, J., A. J. Parsons, and A. D. Abrahams (2000), Plot-scale studies of vegetation, overland flow and erosion interactions: case studies from Arizona and New Mexico, *Hydrological Processes*, *14*(16-17), 2921-2943.

Waldron, L. J. (1977), The Shear Resistance of Root-Permeated Homogeneous and Stratified Soil, *Soil Science Society of America Journal*, *41*(5), 843-849.

Wang, B. (2006), *The Asian Monsoon*, 787 pp., Springer, Berlin.

Ward, D. J., and R. S. Anderson (2011), The use of ablation-dominated medial moraines as samplers for 10Be-derived erosion rates of glacier valley walls, Kichatna Mountains, AK, *Earth Surface Processes and Landforms*, *36*(4), 495-512.

Webster, P. J. (1987), The elementary monsoon, edited, Monsoons.

Weijers, J.W.H., Schouten, S., Schefuß, E., Schneider, R.R., Sinninghe Damsté, J.S., 2009. Disentangling marine, soil and plant organic carbon contributions to continental margin sediments: A multi-proxy approach in a 20,000 year sediment record from the Congo deep-sea fan. Geochim. Cosmochim. Acta 73, 119–132.

West, A., M. Arnold, G. Aumaître, D. Bourlès, K. Keddadouche, M. Bickle, and T. Ojha (2015), High natural erosion rates are the backdrop for present-day soil erosion in the agricultural Middle Hills of Nepal.

Whipple, K. X. (2004), Bedrock Rivers and the Geomorphology of Active Orogens, *Ann. Rev. Earth Planet Sci. , 32*, 151-185.

Whipple, K. X., and G. E. Tucker (1999), Dynamics of the stream-power river incision model: Implications for height limits of mountain ranges, landscape response timescales, and research needs, *Journal of Geophysical Research*, *104*(B8), 17661-17674.

Willenbring, J. K., and F. von Blanckenburg (2010), Long-term stability of global erosion rates and weathering during late-Cenozoic cooling, *Nature*, *465*(7295), 211-214.

Willett, S. D. (1999), Orogeny and orography: The effects of erosion on the structure of mountain belts, *Journal of Geophysical Research: Solid Earth*, *104*(B12), 28957-28981.

Willett, S. D., and M. T. Brandon (2002), On steady states in mountain belts, *Geology*, *30*(2), 175-178.

Wilson, L. (1973), Variations in mean annual sediment yield as a function of mean annual precipitation, *American Journal of Science*, *273*(4), 335-349.

Wobus, C., A. Heimsath, K. X. Whipple, and K. V. Hodges (2005), Active out-of-sequence thrust faulting in the central Nepalese Himalaya, *Nature*, *434*(7036), 1008-1011.

Wobus, C., K. X. Whipple, E. Kirby, N. P. Snyder, J. Johnson, K. Spyropolou, B. Crosby, and D. Sheehan (2006), Tectonics from topography: Procedure, promise, and pitfalls, *Geological Society of America Special Papers*, *398*, 55-74.

Wolman, M. G., and J. P. Miller (1960), Magnitude and frequency of forces in geomorphic processes, *The Journal of Geology*, 54-74.

Wolman, M. G., and R. Gerson (1978), Relative scales of time and effectiveness of climate in watershed geomorphology, *Earth surface processes*, *3*(2), 189-208.

Wulf, H., B. Bookhagen, and D. Scherler (2010), Seasonal precipitation gradients and their impact on fluvial sediment flux in the Northwest Himalaya, *Geomorphology*, *118*(1-2), 13-21.

Wulf, H., B. Bookhagen, and D. Scherler (2012), Climatic and geologic controls on suspended sediment flux in the Sutlej River Valley, western Himalaya, *Hydrol. Earth Syst. Sci.*, *16*(7), 2193-2217.

Yamanaka, H., and S. Iwata (1982), River terraces along the middle Kali Gandaki and Marsyandi Khola, central Nepal, *Journal of Nepal Geological Society*, *2*(1), 95.

Yanites, B. J., and G. E. Tucker (2010), Controls and limits on bedrock channel geometry, *Journal of Geophysical Research: Earth Surface*, *115*(F4), n/a-n/a.

Yanites, B. J., G. E. Tucker, and R. S. Anderson (2009), Numerical and analytical models of cosmogenic radionuclide dynamics in landslide-dominated drainage basins, *Journal of Geophysical Research: Earth Surface*, *114*(F1), F01007.

Yanites, B. J., G. E. Tucker, K. J. Mueller, and Y.-G. Chen (2010a), How rivers react to large earthquakes: Evidence from central Taiwan, *Geology*, *38*(7), 639-642.

Yanites, B. J., G. E. Tucker, K. J. Mueller, Y.-G. Chen, T. Wilcox, S.-Y. Huang, and K.-W. Shi (2010b), Incision and channel morphology across active structures along the Peikang River, central Taiwan: Implications for the importance of channel width, *Geological Society of America Bulletin*, *122*(7-8), 1192-1208.

Yin, A. (2006), Cenozoic tectonic evolution of the Himalayan orogen as constrained by along-strike variation of structural geometry, exhumation history, and foreland sedimentation, *Earth-Science Reviews*, *76*(1,Äì2), 1-131.

Zhao, W., K. D. Nelson, J. Che, J. Quo, D. Lu, C. Wu, and X. Liu (1993), Deep seismic reflection evidence for continental underthrusting beneath southern Tibet, *Nature*, *366*(6455), 557-559.

Zhisheng, A., et al. (2011), Glacial-Interglacial Indian Summer Monsoon Dynamics, *Science*, *333*(6043), 719-723.